

AD-A059 562

WASHINGTON STATE UNIV PULLMAN DEPT OF PHYSICS
CHARACTERISTIC EXOEMISSION FROM OXIDE COVERED ALUMINUM ALLOYS.(U)

F/G 11/6

JUL 78 P BRAUNLICH, J T DICKINSON

F49620-77-C-0042

UNCLASSIFIED

AFOSR-TR-78-1354

NL

1 of 2

AD
A059562

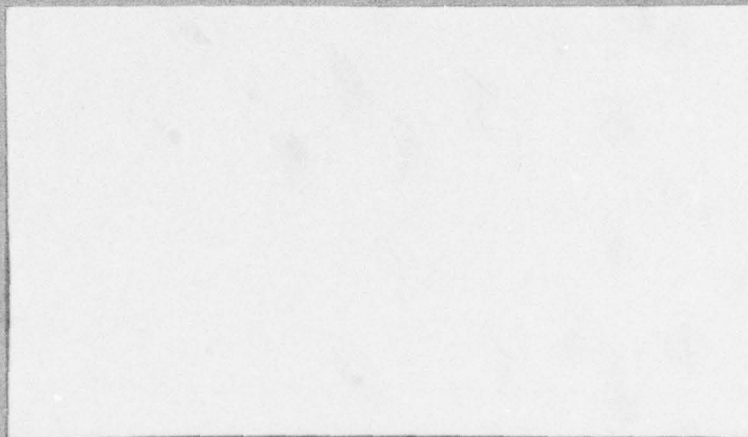


FOSR-TR- 78-1354

~~SECRET~~ (1) LEVEL II

AD A059562

DDC FILE COPY



DDC
RECEIVED
OCT 6 1978
B

Approved for public release;
distribution unlimited.

78 09 13 113

UNCLASSIFIED

SECURITY CLASSIFICATION OF THIS PAGE (When Data Entered)

REPORT DOCUMENTATION PAGE		READ INSTRUCTIONS BEFORE COMPLETING FORM	
1. REPORT NUMBER AFOSR-TR-78-1354	2. GOVT ACCESSION NO.	3. RECIPIENT'S CATALOG NUMBER	
4. TITLE (and Subtitle) Characteristic EXOEMISSION FROM OXIDE COVERED ALUMINUM ALLOYS.		5. TYPE OF REPORT & PERIOD COVERED ⑨ FINAL Repts	
7. AUTHOR(s) ⑩ P. Braunlich and J. T. Dickinson		8. CONTRACT OR GRANT NUMBER(s) ⑮ F49620-77-C-0042	
9. PERFORMING ORGANIZATION NAME AND ADDRESS Department of Physics Washington State University Pullman, Washington 99164		10. PROGRAM ELEMENT, PROJECT, TASK AREA & WORK UNIT NUMBERS ⑮ 61102F ⑮ 2306/A2 ⑮ A2	
11. CONTROLLING OFFICE NAME AND ADDRESS AFOSR/NE Bldg 410 Bolling AFB DC 20332		12. REPORT DATE ⑪ July 1978	
14. MONITORING AGENCY NAME & ADDRESS (if different from Controlling Office)		13. NUMBER OF PAGES 104	
		15. SECURITY CLASS. (of this report) UNCLASSIFIED	
		15a. DECLASSIFICATION/DOWNGRADING SCHEDULE	
16. DISTRIBUTION STATEMENT (of this Report) ⑫ 128 p. Approved for public release; Distribution unlimited			
17. DISTRIBUTION STATEMENT (of the abstract entered in Block 20, if different from Report)			
18. SUPPLEMENTARY NOTES			
19. KEY WORDS (Continue on reverse side if necessary and identify by block number)			
20. ABSTRACT (Continue on reverse side if necessary and identify by block number) Electrons, positive and negative ions as well as photons are known to be emitted from oxides of a number of metals during tensile deformation. It has been shown that the propagation of cracks in the oxide is uniquely associated with this so-called tribo-stimulated exoemission phenomenon. In this report we describe experiments concerning the tribo-stimulated emission of negatively charged particles from oxidized bare and aluminum clad Al 2024 and Al 7075. The investigated samples were anodically oxidized under various conditions to produce oxide layers of different thickness, as well as chemical and mechanical properties. Our			

401 959


UNCLASSIFIED

SECURITY CLASSIFICATION OF THIS PAGE(When Data Entered)

working hypothesis is that exoemission during tensile elongation is determined by the physical and chemical properties of the oxide layer. Evidence in support of this hypothesis is presented for the bare and clad alloys studied to date. The features of the exoemission curves (emission rate vs. strain of the substrate) that appear to be most sensitive to changes in the oxide layer presented and discussed.



UNCLASSIFIED

SECURITY CLASSIFICATION OF THIS PAGE(When Data Entered)



Abstract

Electrons, positive and negative ions as well as photons are known to be emitted from oxides of a number of metals during tensile deformation. It has been shown that the propagation of cracks in the oxide is uniquely associated with this so-called tribo-stimulated exoemission phenomenon. In this report we describe experiments concerning the tribo-stimulated emission of negatively charged particles from oxidized bare and aluminum clad Al 2024 and Al 7075. The investigated samples were anodically oxidized under various conditions to produce oxide layers of different thickness, as well as chemical and mechanical properties. Our working hypothesis is that exoemission during tensile elongation is determined by the physical and chemical properties of the oxide layer. Evidence in support of this hypothesis is presented for the bare and clad alloys studied to date. The features of the exoemission curves (emission rate vs. strain of the substrate) that appear to be most sensitive to changes in the oxide layer presented and discussed.



~~SECRET~~ (1) **LEVEL III**

Department of Physics
Washington State University
Pullman, WA 99164

Final Report
July 1978

CHARACTERISTIC EXOEMISSION FROM OXIDE
COVERED ALUMINUM ALLOYS

By

P. Braunlich and J. T. Dickinson

Prepared for AFOSR
Under Contract #F49620-77-C-0042

Major W. C. Simmons
Contract Monitor

DISTRIBUTION STATEMENT A
Approved for public release;
Distribution Unlimited

DDC
RECEIVED
OCT 6 1978
B

AD A059562

DDC FILE COPY

78 09 13 113

Characteristic Exoemission from Oxide Covered
Aluminum Alloys

Table of Contents

	<u>Page</u>
ABSTRACT	1
FOREWORD	1
 <u>PART A</u>	
I. INTRODUCTION	2
II. TEST FACILITY	4
III. SAMPLES AND SAMPLE PREPARATION	5
IV. EXPERIMENTAL PROCEDURE	7
V. RELEVANT PARAMETERS	8
VI. ADDITIONAL INFORMATION	10
VII. RESULTS	11
1. Aluminum-Clad Samples	11
1.1 Ammonium Tartrate Anodization	11
1.2 Phosphoric Acid Anodization	13
2. Bare Samples	15
2.1 Bare Aluminum 2024	15
2.2 Bare Aluminum 7075	15
3. Comparison of Characteristic Exoemission from Al 2024 and Al 7075	16
4. Boeing Porous Oxide Samples	19
4.1 Boeing Porous Oxides on Clad Al 2024	19
4.2 Boeing Porous Oxides on Bare Al 2024	22
 <u>PART B RECENT WORK</u>	
I. Introduction	27
II.1. Auger Electron Spectroscopy and Ion Sputtering Capabilities . . .	28
II.2. Effects of Oxide Aging on Exoemission	29
II.3. Different Rinsing Solvents	30

	<u>Page</u>
II.4. Deviations from the Baseline Oxide	31
II.5. Neutral Emission	32
SUMMARY	35
REFERENCES	36
FIGURE CAPTIONS	37
LIST OF PUBLICATIONS	40
LIST OF PERSONNEL	41
COUPLING ACTIVITIES	43

ACCESSION for		
NTIS	White Section	<input checked="" type="checkbox"/>
DDC	Buff Section	<input type="checkbox"/>
UNANNOUNCED		<input type="checkbox"/>
JUSTIFICATION		
BY		
DISTRIBUTION/AVAILABILITY CODES		
Dist.	AVAIL. and/or	SPECIAL
A		

Forword

The work reported in Part A of this report was conducted in the first nine months of the present contract period (January 1, 1977 - September 30, 1977) and that in Part B in the subsequent period from October 1, 1977 to February 28, 1978. The primary objective of this research was to experimentally verify the following conjecture: does a characteristic tribo-stimulated exoemission curve exist for a given metal oxide-metal alloy system which permits an inexpensive and quick test of the quality of the particular oxide coating? The economic implications of such a quality control test are obvious in light of the importance of oxide layers as protective coatings or their role in adhesive bonding of metal alloys in the manufacturing of airplane frames and the like.

In this report we will first introduce the phenomenon of tribo-stimulated exoemission, describe the facility assembled at WSU to conduct the reported research and present recent results obtained under Air Force sponsorship (Contract #F49620-77-C-0042). These results strongly suggest the existence of characteristic exoemission curves (CEC) for all samples investigated up to this time: bare and aluminum-clad Al 2024 and Al 7075, coated with oxide layers of different thickness and chemical and physical properties. We discuss the features of these exoemission curves which appear to be most sensitive to variations in the substrate-oxide system. Finally, neutral particle emission during tensile deformation of oxide coated aluminum alloys was clearly observed for the first time and analyzed with a mass spectrometer. Distinct differences between the characteristic exoemission curve of negative particles and the neutral emission curve are described.

I. INTRODUCTION

Tribo-stimulated exoemission of charged particles is a transient phenomenon that is observed from a variety of oxide-covered metals during mechanical deformation or abrasion.⁽¹⁻⁵⁾ It has to be distinguished from a number of other so-called exoemission processes that occur when dielectric or semiconducting materials are subjected to external stimulation in the form of photons (photo-stimulated exoemission)^(6,7) or temperature increase (thermally stimulated exoemission).⁽⁸⁾ Freshly prepared metal surfaces may give rise to chemi-stimulated exoemission when they are allowed to react with certain chemically active gases.⁽⁹⁾

In order to study one of these emission processes, the experiments must be designed such that all other sources of stimulation are eliminated. Tribo-stimulated exoemission from oxide-covered metals must therefore be investigated under conditions which preclude the occurrence of chemical, thermal, as well as photo-stimulation. This can be done in high vacuum, in total darkness, and at a fixed temperature, e.g., room temperature.

In the past 10 years, a number of experiments on tribo-stimulated emission from oxide-covered metals have been carried out under fairly well controlled environmental conditions. Basically two modes of surface deformation were employed: (a) scratching the specimen with a scribe or abrading it with a steel brush and (b) tensile deformation. The emission from oxide-covered aluminum,⁽¹⁻⁶⁾ magnesium,⁽³⁾ nickel,^(1,2) and titanium^(1,2) was studied at various oxide thicknesses and strain rates. During tensile deformation, the emission was found to occur in bursts after initiation at a very low strain ($\approx 0.2\%$). Its intensity depends on oxide thickness and on the rate at which the sample strain increases with time. Emission is observed only

during ongoing deformation or abrasion and usually ceases abruptly when these forms of mechanical stimulation are interrupted. In some cases ($\leq 1000 \text{ \AA}$ thick oxide layers on aluminum-clad Al 2024), a distinct and characteristic emission after rupture of the sample is observed for several minutes; an effect that has yet to be explained (see Section VII).

The mechanism responsible for tribo-stimulated exoemission is not known in detail. Clearly, emission occurs only during the propagation of cracks or during the disruption of the continuity of the oxide film during abrasion. Gieroszynski et al.^(5,6,10) have suggested the so-called electrified fissure mechanism, according to which the walls of propagating cracks are assumed to be oppositely charged and the resulting intense electric fields are sufficient to cause field emission of electrons. On the other hand, Arnott and Ramsey⁽³⁾ proposed that the strain energy released at the tip of the propagating crack may lead in some unspecified way to the emission of electrons. All previous authors observed only negatively charged particles and assumed these to be electrons. In our previous studies we have discovered that negative and positive ions as well as photons are emitted as well and, as a consequence, the most likely mechanism is field-assisted thermionic emission of these particles from the tip of the propagating cracks^(1,2) (Attachment B). The emission of photons is of particular interest for the anticipated practical applications of tribo-stimulated emission. Single-photon counters can be used that do not require the sample to be in high vacuum during the test, thus opening possibilities to observe exoemission in ambient air and to study the effects of reactive gases which are expected to enhance the emission or permit the detection of propagating surface cracks even in an unoxidized alloy.

As stated in the Foreword, the present investigations were carried out with the goal to establish the existence of a characteristic exoemission

curve for a given metal alloy coated with a specific oxide. A large variety of bare and aluminum-clad Al 2024 and Al 7075 samples were tested. The oxidation processes used (see Section III) were selected because the chemical and physical properties of their oxide layers are well known,⁽¹¹⁻¹⁵⁾ and they are of manufacturing interest for finding surfaces which facilitate adhesive bonding. This goal has been achieved (see Section VII), and we have established that for these samples the exoemission curve is indeed a "fingerprint" of the particular metal oxide-metal alloy system as obtained via our test procedure (Section IV).

II. TEST FACILITY

One system assembled for these studies consisted of an ultrahigh vacuum system which incorporated a fully instrumented tensile straining device, a Varian Auger-electron spectrometer (presently being tested), a residual gas analyzer, and a special high sensitivity-low resolution electron energy analyzer. Single event channeltron electron multipliers (CEM) are available for the detection of charged particles as well as a single photon counter with S-20 photocathode (Bendix BX754) for the measurement of photons in the visible region of the electromagnetic spectrum. This system is described in detail elsewhere⁽¹⁾ (Attachment A). A second vacuum system, equipped with a duplicate of the tensile straining device, a low noise channeltron and a single photon counter was built during the nine-month contract period. The use of high vacuum (1×10^{-6} Torr) instead of UHV did not measurably affect the characteristic exoemission curve. This apparatus allows us to test in a comparable time many more samples as compared to the UHV system which is now used exclusively for experiments that require UHV (such as surface-analytical studies using Auger spectroscopy, mass spectrometry and the like). A high resolution scanning electron microscope and an optical

microscope together with oxidation facilities are also available to us for our exoemission studies.

A schematic of the tensile straining device and of the detection arrangement of the particle detector used in both vacuum facilities is shown in Fig. 1 of Attachment A.

III. SAMPLES AND SAMPLE PREPARATION

All samples were machined by a slow milling process (to avoid unnecessary stresses and temperature increase) to the dimensions indicated in Fig. 1. The 20 mil thick material was provided from production stock by the Boeing Commercial Airplane Company, Seattle, Washington. Electrolytic anodization for the production of oxide layers on these samples was performed in the following three different laboratories using either an ammonium tartrate electrolyte to form dense (barrier type) oxides or a phosphoric acid electrolyte which results in porous (duplex type) oxides:

- a) Washington State University: samples produced to test the facility only; no results of these tests are included in Section VII.
- b) AFML, WPAFB, Dayton, Ohio (laboratory Dr. W. Baun).
- c) Boeing Commercial Airplane Company, Seattle, Washington.

The samples prepared at AFML were coated with oxides of nominal thicknesses ranging from 500 Å to 4500 Å in a standard (0.05 M) ammonium tartrate electrolyte to produce dense barrier type oxides, or in a 1 M phosphoric acid electrolyte which yields a porous duplex oxide layer. Different oxide thicknesses are achieved by varying the electric potential on the electrodes in the case of the ammonium tartrate (dense) oxides, and by varying the time (duration) of oxidation in the case of the H_3PO_4 (porous) oxides. Spot checks of the actual thickness of a number of samples using SEM techniques

generally revealed good agreement of the so-called nominal thickness with the measured thickness in all aluminum-clad samples (an exception is described in Section VII.1.2). This was not so for all bare alloys investigated. The nominal thickness in these cases appears to be considerably less than the actual thickness. Since these deviations are characteristic for each type of sample, we have not corrected the oxide thicknesses at that point in time and we have plotted the exoemission vs. the nominal thickness only. In this way trends with thickness are recognizable without having to carry out time-consuming SEM thickness measurement of all individual samples.

The samples oxidized at Boeing used a procedure similar to those employed for production of oxides suitable for epoxy bonding. (These samples are subsequently called Boeing Baseline Samples.)

1. (Baseline) Details of Phosphoric Acid Anodizing Process:

- 1) Solvent wipe w/MEK (methyl Ethyl Ketone).
- 2) Alkaline clean 10 minutes (immersion in Kelite 25E @ 140°F).
- 3) Hot water rinse 3-5 minutes (spray or running water @ 110°F minimum).
- 4) Etch 10 minutes (immersion in Amchem #6 @ room temperature).
- 5) Cold water rinse 3-5 minutes (spray or running water @ 90°F minimum).
- 6) Anodize in 10 (wt)% orthophosphoric acid (~85%) @ 74°F
20 minutes and 10 volts potential.
- 7) Cold water rinse 3-5 minutes with a 15 second delay between
the termination of anodizing and the start of rinsing.
- 8) Dry at room temperature.

This process produces a rather thin ($<2000 \text{ \AA}$) porous oxide on bare Al 2024 and a several thousand \AA thick porous oxide ($<5000 \text{ \AA}$) on aluminum-clad Al 2024.

Variation of this process, investigated by us, included

2. (20V): Use 20V and 8 (wt)% H_3PO_4 in step 6 and reduce temperature to 66°F
3. (4V): Use 40V and 8 (wt)% H_4PO_4 in step 6 and reduce temperature to 64°F

to produce thicker (2) and thinner (3) porous oxide layers as compared to the Boeing Baseline sample, and

4. ("Without Etch"): Omit etch process (step 4).

These variations produce characteristic exoemission curves that are different from the curve obtained from Boeing Baseline samples. The change in temperature is expected to result in a different surface texture. At the same time, process 4 (omission of the etch treatment) may produce an oxide that can be undesirable for bonding since gross contamination e.g., due to outdoor storage) is not removed in the manufacturing process. Our samples, being stored under selectively clean conditions after rolling the metal, are not expected to be affected greatly by omission of step 4.

IV. EXPERIMENTAL DATA

IV.1. Measurement Procedure

After receipt the samples were placed into a desiccator. Just prior to installation in the test chamber, the sample was rinsed in reagent grade acetone and, as soon as the vacuum had reached about 1 to 3×10^{-6} Torr, pulled until rupture with a constant strain rate of $\epsilon = 0.014\% \text{ sec}^{-1}$. The stress-strain curve was recorded during pulling and, simultaneously, the exoemission count rate was measured.

Optical microscopy was used to survey the cracking pattern and scanning electron microscopy for the investigation of the crack walls and other characteristic features of the oxide.

IV.2. Display of Data

During the straining of the sample, a stress-strain curve was generated on an x-y recorder with time-markers being produced every 15 seconds to insure that the strain rate was indeed linear. Simultaneously, the pulses from the CEM are amplified and handled with the system shown in Fig. 2. The pulses are stored and displayed in 3 ways: (1) Simply counted with a scaler, providing total accumulated counts. (2) Stored in a multichannel scaler where typically each channel accumulates counts for 0.8 seconds then advances to the next channel and accumulates counts for the same time interval. (3) A count rate meter integrates the pulses and displays on a chart recorder the count rate vs. time. The use of the count rate meter and the multichannel scaler allows for considerably more flexibility and detail in handling the data.

Figure 3 shows a typical stress-strain curve for an clad Al 2024 sample elongated under vacuum in our system. Figures 4a and 4b show the multichannel analyzer output and rate meter output. The exoemission data for a 3000 Å dense oxide layer on clad Al 2024 anodized in the ammonium tartrate solution, which is a good emitter. Figure 5a and 5b show similar results for a much weaker emitter, a thin porous oxide on bare Al 2024 anodized in phosphoric acid (Boeing Baseline Bare Al 2024). Figure 5c shows the digital data smoothed by an averaging technique discussed in Sec. VII.2. We note here that even though the emission is weak, the reproducibility of the characteristic exoemission obtained from nominally identical samples is remarkable.

V. WHAT ARE THE RELEVANT PARAMETERS?

In these experiments we are interested in detecting properties of the exoemission curves which change as one changes the type of oxide layer (e.g., dense vs. porous), the substrate (e.g., pure Al, various alloys, clad alloys)

oxide thickness, possibly even chemical composition (e.g., impurities, degree of hydration, etc.). We have successfully varied a few of the initial parameters of the substrate-oxide layer system and examined the data for details which indicate differences in the exoemission curves. To date we find the following set of characteristics the most obvious "fingerprints" for a given substrate oxide layer system:

1. Total Counts. This parameter indicates the overall strength of exoemission from the time strain begins until rupture.
2. Initial onset of emission. As the substrate undergoes strain, exoemission is initially negligible until some particular minimum strain and is reported in percent strain. The onset's position relative to the onset of plastic deformation is also frequently discussed.
3. Number of peaks. Some types of samples emit one peak, others yield multiple peaks, e.g., one major peak and several smaller peaks.
4. Peak positions and widths at half-maximum (particularly the major peak) usually measured in percent strain.
5. Occurrence of a "precursor" peak prior to rupture. Several types of samples show increased emission several seconds before rupture. When this peak is present, its height, position, and shape are considered potentially relevant.
6. Occurrence of a spike at rupture. Some samples yield a very narrow but easily detected flurry of pulses immediately following rupture (the duration of this spike is 1 second or less). When this spike is present, the number of counts in the spike is considered potentially relevant.

7. Occurrence of after-emission following rupture. Some samples emit negative particles even after rupture. Generally this after-emission slowly decays with a duration as long as 3-4 minutes. When after-emission is present, the magnitude and duration are considered most important.

VI. OTHER INFORMATION BEING ACCUMULATED

In addition to exoemission curves, we are also examining a number of the samples with the optical microscope and scanning electron microscope (SEM) both before and after deformation. The type of information we obtain with these methods include:

1. Density and size of pits in the oxide layer. This is likely to be unimportant in explaining exoemission but may be very significant in the role of the oxide layer in adhesive bonding.⁽¹⁶⁾
2. Overall surface roughening of the oxide layer due to deformation.
3. Overall distribution of cracks along the length of the deformed samples, including density.
4. Morphology of the cracks in the oxide layer as a function of position; e.g., shape, length, width, etc. Particular differences have been observed between cracks near the rupture and away from the rupture.
5. Side-on-view of the oxide layer with the SEM yields information about the structure of the original oxide layer (e.g., dense vs. porous, pore size, and density) as well as a measure of the oxide thickness.

Auger electron spectroscopy (AES) is soon to be available for examining the make-up of the oxide-layer surface, including a sputtering profile through

the oxide layer. We are most interested in determining the role of impurities and exoemission and whether or not the chemical nature of the oxide layer changes during elongation.

A quadrupole mass spectrometer is also available. One important use of this instrument is to determine the identity of ions which are emitted during elongation. In addition, we hope to look for neutral particles during the pulling of the sample. Potential species include chemisorbed gases such as H_2 , O_2 , and H_2O .

The remaining sections of this report will include first a brief description of the data for a number of substrate oxide layer systems, followed by a discussion of differences and similarities found between them, and finally a brief discussion of possible explanations for some of the effects we observed.

VII. RESULTS

VII.1. Aluminum-Clad Al 2024 Samples

VII.1.1. Ammonium Tartrate Anodization--Wright Patterson. These samples were studied with oxide layers ranging from 500 Å to 4000 Å in thickness. The oxide layer can be characterized as a "dense," "barrier-type," or "non-porous" oxide. There is little solvent action during its formation. SEM photos of the unstrained surface of this oxide shows the absence of pits. Higher magnification of samples bent into a right angle to expose the oxide layer for viewing shows no evidence of pores. It appears to have a two-layered structure seen as a very thin dark layer at the substrate-oxide interface.

For oxides thicker than 1500 Å, the cracks are very straight and uniformly spread, approximately 10μ apart at the rupture strain. For these

thicker oxides, the cracks often extend a millimeter or more. Thinner oxides did not exhibit the long straight cracks; on the contrary, they seem to be in sets of parallel, short cracks and are closely packed. We believe this to be due to the fact that the thinner oxides are breaking up along the slip steps on the substrate surface. The thinner oxides are obviously more strongly influenced by the substrate than the thicker oxides. (2,3)

The density and appearance of the cracks on the ammonium-tartrate samples are quite uniform along the part of the sample which has undergone uniform elongation. In the region of the rupture, the cracks appear to be wider and perhaps deeper.

The total emission of negative particles from the ammonium-tartrate samples is strongly dependent on thickness of the oxide layer (see, e.g., Fig. 10). A typical emission curve obtained from a thick oxide (4000 \AA) is shown in Fig. 6. Superimposed on the curve is the stress-strain curve which was recorded during the elongation. The curve shows two peaks: the major peak soon after the sample entered plastic deformation, and a smaller peak just before rupture, a so-called "precursor peak." No after-emission was observed. The onset of emission is seen to begin after a short delay following the transition from elastic to plastic deformation. The onset of emission comes at about 4% elongation for the 4000 \AA samples and shifts to about 6% elongation for the thin oxides. The major peak occurs at around 5% elongation for the 4000 \AA samples and shifts to about 8% for thin oxides. The full width at half maximum of the thicker oxide peaks were around 1.8% elongation, whereas the widths of the thinner oxide peaks were closer to 3.0%. (These results are shown in Figs. 11 and 12 together with similar measurements made on clad Al 2024 covered with porous oxide.)

A 4000 \AA ammonium tartrate sample was pulled in air and micrographs of the surface were made at 100x. At elongations in the elastic range no

cracks in the oxide were visible. After the sample went into the plastic region, fine cracks less than 0.5 mm in length were observed, corresponding to the rise of emission. As the sample was further extended these cracks grew in length and additional cracks appeared, presumably corresponding to further emission. Finally for further elongation, additional cracks were not seen to appear and the cracks simply grew wider. The small decreasing level of emission in this region is presumably due to a very small number of cracks being created and/or increasing in length. As the sample approaches rupture, it necks down in a region within ~0.2 mm of the future break. This necking-down is accompanied by the production of a large number of cracks in the substrate in this region. It is during this time that the precursor peak is occurring. Since the precursor only occurs on certain types of substrate-oxide systems, we suggest it is due to further break-up of the oxide layer in the vicinity of the rupture and only certain oxides are so disrupted by the necking-down. If the oxide is flexible enough, it is not cracked further during these last few seconds of the pull.

VII.1.2. Phosphoric Acid Anodization--Wright Patterson. Samples of this type were investigated with oxide layers between 500 Å and 4500 Å thickness. The oxide appears to be the "classic" porous, duplex layer expected to be formed by acidic anodization. SEM photos of the unstrained surface reveal the presence of characteristic larger pits and small pores of the kind apparently needed for adhesive bonding.⁽¹⁶⁾ High magnification SEM pictures taken of sharply bent samples (to expose the walls of the cracks in the oxide) show clear evidence of open pores on top of a rather thin dense layer adjacent to the substrate. An interesting fact was revealed by these pictures. The thickness of the oxide nominally expected to be 3500 Å was about 4000 Å and

that of the nominally 4000 Å thick samples (all prepared in one batch) was about 3500 Å (Fig. 7). Erroneous sample designation may be the cause for this mix-up. We have plotted the curves using the nominal thickness as a case in point to show that the exoemission technique readily detects such errors (see Fig. 9).

The rupture behavior of the porous oxides is in several respects different from that of the dense oxides (Section VII.1.1). Again, the oxides (up to 1000 Å) crack along slip lines and cracks in the grains. However, the average crack density appears to be higher at the rupture strain. The onset of cracking in thick (4000 Å) porous oxides occurs later (at about 5% strain) as compared to dense oxides. The cracks are short and never develop into the type (traversing the gauge completely) observed in dense oxide. With increasing strain they grow in density but do not appear to increase in width. These differences should be kept in mind when the exoemission curves of these samples are compared with those obtained from the same substrate covered with dense oxide.

The exoemission curve of these samples is characterized by a dominant main peak occurring at a strain that is about 3% higher than the onset of plastic deformation with no apparent dependence on oxide thickness. A precursor peak is again observed in samples covered with less than 1000 Å thick oxide. It appears between 25% and 28.7% strain.

Typical raw exoemission data for these samples are shown in Fig. 8. The dependence of the total number of emitted particles is presented in Fig. 9 and again in Fig. 10 where, for comparison, the results obtained on clad Al 2024 covered with a dense oxide are shown as well. The peak locations on the strain axis and the full widths at half maximum of the main peak of the two different materials (clad Al 2024, dense and porous oxide) are compared in Figs. 11 and 12. These results are summarized in Table I.

VII.2. Bare Samples

VII.2.1. Aluminum 2024 Bare

Up to this point in time our investigations have included only bare Al 2024 samples covered with dense oxide (see Section III). Only exoemission data and no optical micrographs are available to date and SEM studies were only undertaken for spot checks of the actual oxide thickness.

The exoemission curves exhibit one maximum above oxide thicknesses of 2000 Å and a number of smaller peaks below 2000 Å (see Fig. 13). The total emission is rather high for the thicker oxides and decreases rapidly with decreasing oxide thickness (Fig. 14). The location of the main peak on the strain axis and its full width at half maximum are shown in Figs. 15 and 16. The exoemission data obtained from these samples are summarized in Table I, and compared with data measured on other Al 2024 samples. A more detailed discussion of these preliminary results is presented in Section VII.3.

VII.2.2. Aluminum 7075 Bare

The investigation of this material is still incomplete. No optical or SEM micrographs have been obtained so far to study cracking patterns and the appearance of the oxide layer or the crack wall under high magnification. A series of samples covered with porous oxide and dense oxide, produced at Wright Patterson (see Section III), was pulled and the characteristic exoemission curves were measured in the high vacuum facility.

Both porous and dense oxides on bare Al 7075 feature a pronounced main peak at thicknesses >2000 Å which broadens and becomes less distinguished in the thinner oxides. Dense oxides on this material produce a characteristic splitting of this main exoemission peak above 2000 Å oxide thickness (Fig. 17). Again, the dense oxides emit considerably more negative particles as compared to porous oxides of comparable thickness, and the total number of emitted particles increases monotonically with oxide thickness (Fig. 18). The

position of this peak shifts to lower strains with increasing oxide thickness in dense oxides and remains relatively fixed in porous oxides (Fig. 19). The full width at half maximum decreases in both oxides with decreasing thickness (Fig. 20). Other characteristic features (after-emission below 1000 Å, occurrence of a precursor peak prior to rupture of the sample) are summarized in Table I in comparison with data obtained from Al 2024 alloys.

VII.3. Comparison of Characteristic Exoemission from Al 2024 and Al 7075

In this section we will attempt to compare the exoemission features measured in Al 2024, both bare and clad with aluminum, and in bare Al 7075 covered with dense or porous oxides. Information on clad Al 7075 covered with either oxide and from bare Al 2024 covered with porous oxide will soon be available.

The oxidation of all samples was carried out at the Materials Laboratory of WPAFB under controlled laboratory conditions, e.g., there was no intentional variation in the concentrations of the electrolyte used or the temperature of anodization. Consequently, for a given batch of samples covered with a selected oxide, only the thickness was varied via either the length of time of anodization (to produce porous oxide in phosphoric acid) or the applied potential (to produce dense oxide in ammonium tartrate). Thus we expect no variation of the essential chemical and physical properties in a given batch aside from those varying with oxide thickness. The characteristic features of the exoemission curves obtained from a given batch should reflect only the variations in the properties of the oxide described with the thickness variation.

As pointed out before, SEM spot checks have revealed a consistent deviation of the actual oxide thickness from the nominal one (as stated by the ML at WPAFB, based on well known anodization procedures) in all cases where the bare (unclad) alloy was oxidized. Nevertheless, we have plotted all results

as a function of the nominal thickness because this will indicate trends with thickness as well.

The total number of emitted negative particles as well as its peak height decreased with oxide thickness in all cases. The main peak was a commonly observed feature of all tested samples and only below 1000 Å to 2000 Å thickness (depending on the substrate-oxide system) did it become less distinct among several smaller peaks. We intend to analyze in more detail (e.g., using curve-smoothing of the digital data) the lower emission curves for the Air Force thin oxides, particularly since we have seen reproducible and characteristic structure in these curves for a particular oxide. For the Boeing samples (Section VII.4), the sometimes rather subtle variations in the anodization process produced quite recognizable and reproducible changes in the exoemission curve. These observations lead us to believe that, indeed, even when the exoemission intensity is quite low a characteristic exoemission curve exists for a given oxide substrate system. On first sight, the "Air Force" samples exhibit features that appear common to all samples covered with thick oxide. However, careful comparison of the peak position, the total number of negative particles emitted, etc. reveal several differences that permit one to distinguish between samples with exoemission data alone (see Table I). For a given nominal thickness, dense oxides on clad Al 2024 emit the most particles, followed by porous oxides on the same material, dense oxide on bare Al 7075, dense oxide on bare Al 2024 and, finally, porous oxide on bare Al 7075. The variations in the measured peak position and the full width at half maximum of the main peak are displayed in Figs. 11, 12, 15, and 16. A quite distinct feature of the porous oxides on all investigated materials and of dense oxide on clad Al 2024 is the occurrence of a precursor peak prior to rupture of the sample. (See also Section VII.4). In addition, thin porous oxides on clad Al 2024 and thick

Table I

Mat.	Oxide	Thickness	Counts	Number* of Peaks	Position of Major Peak After Plastic	Major Peak Height	fwhm	Precursor Peak Height	After Emission Duration (Min.)	Counts
2024	Porous (H ₃ PO ₄)	4000 Å	31,000	2	3.3%	~450	2.77%	9		
		1000 Å	~300	2	2.6%	6	3.6%	2	2	300
	Dense (Amm. Tar)	4000 Å	60,000	2	1.5%		1.76%	20		
		1000 Å	10,000	2	2.5%	100	~8%	10		
Bare 2024	Dense (Amm. Tar)	4000 Å	9,000	1	~1.6%	130	2.4%	---		
		1000 Å	85	1-2	~2.3%	2	4%	---		
Bare 7075	Porous (H ₃ PO ₄)	4000 Å	750	2	3.1%	13	4.1%	10		
		1000 Å	300	?	2.8%	5	~8%	4		
	Dense (Amm. Tar)	4000 Å	~15,000	1	1.4%	440	2.8%	---	5	70
		1000 Å	400	1	2.9%	9	4.2%	---		

*Including Precursors

dense oxides on bare Al 7075 exhibit reproducible emission after rupture of the sample. The origin of both effects is not well understood (see Section VII.4). To summarize, the features of the investigated exoemission characteristics of the various "Air Force samples" are such that a clear distinction appears possible between samples based solely on the exoemission curve.

VII.4. Boeing Porous Oxide Samples

As further evidence of the sensitivity of exoemission to changes in the oxide, we now discuss samples prepared for us by the Boeing Commercial Airplane Company with procedures used for producing oxides of technological importance. The substrates studied so far have been clad and bare Al 2024. Combinations of parameters in the pretreatment or anodization processes were varied slightly to produce changes in the oxide characteristics. Such variables as oxidation temperature, electrolyte concentration, anodization voltage, and a pre-etch treatment were altered (see Section III). Such changes could potentially occur in manufacturing procedures and could make the difference between an acceptable or unacceptable oxide layer.

In the following two sections we discuss the results obtained so far on the Boeing samples.

VII.4.1. Boeing Porous Oxides on Clad 2024 Aluminum

An examination of the Boeing clad Al 2024 samples show the oxide to be porous; Figure 21 shows a SEM photograph of an edge of the Baseline oxide. On the original photograph one can readily see the pore structure. On similar SEM pictures we have determined approximate thicknesses of the oxides (see Table II).

Of the four types of Boeing clad Al 2024 samples investigated so far, the Baseline samples have the most open structure at the surface. This is due to the fact that they were anodized at a higher temperature (74°F) which

leads to a stronger corrosive action by the H_3PO_4 solution on the tops of the pore structure. Under the SEM, this shows up as a very highly textured surface. The "Without Etch" and 20V samples are of intermediate roughness and the 4V samples relatively smooth, presumably because the pores of the 4V samples are very fine or closed at the surface.

Photomicrographs of the extended samples show the cracks formed on each of the four types of surfaces (Fig. 22). The distinctive features are the density, length, and width of the cracks. In our hierarchy of thickness, the thin 4V oxide has a higher density of cracks, but they are fine, short, and appear to be following the grains of the substrate. The thicker 20V oxide shows nearly parallel cracks perpendicular to the direction of strains and are fewer in number while longer and wider. The Baseline and "Without Etch" oxides are seen to be nearly the same, intermediate to the 20V and 4V samples.

Typical exoemission data for these samples are shown in Figs. 23 and 24. (We have not as yet obtained such data on the "Without Etch" clad samples.) The curves shown are original data from the count-rate meter. We have found that in the case of low count rates, the rather noisy emission curve can be smoothed using averaging techniques on the digitized data from the multichannel analyzer. A number of features repeatedly occur when the same type of oxide is examined. Figure 25a and 25b show examples of such curves formed by averaging every five channels near the beginning and end points. In the middle region of the curve, a curve smoothing technique of adding five channels to the previous average and dropping five channels is used. This leads to the formation of smooth peaks with structure very similar to the count rate data (Figs. 23a and b). A comparison of a number of such

curves for identically treated samples indicates that the majority of the peaks so formed are very reproducible (e.g., see two such curves for Al 2024 bare samples) even though the peak heights are only one or two counts per second in height. This allows us to rely on considerably detailed structure in the exoemission curves for characterizing the oxide layers, even for weak emitters.

Table II summarizes the key features of the exoemission data from the Boeing 2024 Clad samples. The interesting differences are:

1. Total counts and peak heights. Significant differences in emission intensity occur between the different oxides. Currently, the baseline samples are the weakest emitters, contrary to what we expect on the basis of oxide thickness. This indicates the strong dependence the exoemission process has on subtle differences in the physical and chemical makeup of the oxide layer. The relatively thin 4V samples, on the other hand, are quite good emitters.
2. Number of peaks and peak shapes. The 20V samples showed the one pronounced peak, occasionally accompanied by a smaller precursor. The Baseline sample shows 2-3 peaks--the first major peak which corresponds to the peak position of the thicker 20V sample; a precursor right before the break which is increasing as the sample ruptures and then ceases emitting immediately; finally a region between these two distinct peaks which occasionally takes on the shape of one or two peaks. The 4V sample shows a much broader peak occurring at greater elongations accompanied by additional peaks on the shoulder and a larger precursor peak that is completely gone at rupture. On the basis of peak positions and shape alone these curves are distinguishable. Again, we find this is due to the differences in the physical and chemical make-up of these oxides which in turn determine the way the oxide breaks up under strain and leads to characteristic exoemission.

3. Onset of emission. The percent elongation where the onset of exoemission begins will also depend on the nature of the oxide. An interesting trend we observe here is the thinner 4V oxide breaks up sooner than the thicker Baseline and 20V samples. (Compare with AF porous oxides.)

4. Presence of precursor. All these samples showed a precursor peak. Relative to the largest peak, the 4V sample showed by far the largest precursor. The cause of this effect is believed to be related to the sample necking down, as discussed previously.

5. After-emission. Only the 4V sample yielded emission of negative particles after rupture. The duration of the emission averaged 3 minutes and totaled on the average 300 counts. The thin Air Force porous oxides on Al 2024 clad also exhibited this after-emission effect. Since the 4V samples were also thin oxides, it indicates the thickness is critical for its presence. After-emission is very difficult to explain. One hypothesis for the cause of after-emission is the possibility of chemical reactions occurring on the freshly exposed substrate metal yielding chemi-emission. The oxide would potentially contain active impurities. As these become unavailable either due to lack of mobility or depletion or as the fresh metal becomes contaminated, the emission would fall off. To explain the thickness dependence, it is further hypothesized that the mechanisms (e.g., surface and/or bulk diffusion) are prohibited by a thicker oxide. Another possible mechanism might involve some relaxation of the substrate-oxide system following rupture.

VII.4.2. Boeing Porous Oxides on Bare 2024 Aluminum

To date we have investigated two types of oxides on bare 2024 aluminum, both provided by Boeing: those produced by the Baseline treatment and the same treatment omitting the acid etching step ("Without Etch"). The purpose

Table II

Boeing Sample 2024 Clad	Oxide Thickness λ	Total Counts	No. of Peaks (Excluding Precursor)	Onset of Emission % Strain from Plastic Onset	Major Peak Height $\frac{\text{Counts}}{\text{sec}}$	Precursor Peak Height $\frac{\text{Counts}}{\text{sec}}$	Duration (min)	After Emission Counts
Baseline (5 samples)	~3500	260	2-3	0.5%	4	2	none	0
Without Etch	~3500	*	*	*	*	*	*	*
⁴ V (6 samples)	<1000	2600	3-4	0.3%	11	5	2-4	300 ave.
²⁰ V (5 samples)	4000-5000	3400	1-2	1%	40	2 (occurs roughly 50% of the time)	none	0

*Data not yet taken.

of the etch is to provide a uniform starting point of a clean, thin oxide layer on the aluminum surface before anodization. The effect of skipping this step will thus depend strongly on the history of the metal prior to treating. The history and condition of the original aluminum sheets used in this study are unknown.

Studies of the anodized characteristic surfaces are still incomplete. However, SEM pictures show both of these oxide layers to be quite thin, well under 1000 Å, and the "Without Etch" is slightly thicker than Baseline.

Figure 26 shows typical count rate vs. percent strain curves for the Baseline and "Without Etch" oxides on Al 2024. One immediately sees that both curves start out with weak emission and then grow into a series of jagged peaks, culminating in the largest peak which is very similar in position to the precursor peak on the clad samples. Note that in both cases this final peak has essentially died away when the sample ruptures. Figures 27a and b are the smoothed digital data for two Baseline Bare samples, showing the reproducibility of the peak structure between samples with identical treatment. (Figure 27a corresponds to the data shown in Fig. 26a.) It should be noted that the Baseline Bare Al 2024 samples are the weakest emitters. Figure 27c is the smoothed digital data for the bare "Without Etch" sample shown in Fig. 26b, again showing very similar peak structures.

Table III summarizes the exoemission data obtained on these two Boeing oxide layers. The major differences in the features examined are:

1. Total counts. The thinner Baseline oxide shows weaker emission than the "Without Etch."
2. The number of peaks, peak positions, and peak shapes are very much the same.
3. The onset of emission is detectably earlier for the Baseline sample.

Table III

Boeing Sample 2024 Bare	Oxide Thickness Å	Total Counts	No. of Peaks	Onset of Emission % Strain from Plastic	Major Peak Height Counts/Sec (Final Peak)	After Emission
Baseline (5 samples)	Thin. <1000 Å	300 ave.	5	1.25%	4.5	none
Without Etch (5 samples)	Thin. <1000 Å	410 ave.	5	2.08%	5.6	none

4. The after-emission is completely absent. This is in spite of the fact that both of these are thin oxides. This is in agreement with observations made on the Air Force thin H_3PO_4 porous oxides on base Al 2024, where after-emission was also missing.

It should be noted again that the particular differences in these oxide layers other than thickness, are not really known. The effects of omitting the etching step would be even more drastic, depending on the history of the material (e.g., sun and weather vs. sitting in a clean vacuum). Extremes in this history, which lead to substantial changes in the properties of the oxide layer would in our case lead to substantial differences in the exoemission from such samples.

PART B

RECENT WORK

I. INTRODUCTION

Part A of this Final Scientific Report (Contract #F49260-77-C-0042) describes experiments which provided strong evidence for the existence of a characteristic exoemission curve for a given aluminum oxide on aluminum alloys. In Part B we report preliminary results of investigations carried out in the contract period October 1, 1977 through February 28, 1978. We report here (a) the testing of our Auger Electron Spectrometer, (b) exoemission experiments on a number of treated oxide films, and (c) the initial results for neutral particle emission which we have discovered accompanies charged particle emission. Under (b) we examine a number of extremely interesting effects due to aging of the oxide, using organic rinsing agents, and varying electrolyte concentration, applied potential, and temperature during anodization of commercial-like oxide layers.

ATTACHMENTS

Three papers are included in this report as Attachments. Two (Attachments A and B) contain published material that was obtained in prior contract periods. Attachment C was prepared for publication in Applied Surface Science and constitutes a report on work performed in the period March 1, 1978 through May 31, 1978.

II.1. Auger Electron Spectroscopy and Ion Sputtering Capabilities

We now have functioning in the UHV system a Varian Auger Electron Spectrometer for analyzing the oxide layers before and after elongation. We also have installed an Ar ion sputtering facility for depth profiling. To position the sample relative to the Cylindrical Mirror Analyzer (CMA), a mechanical pusher was devised to adjust the distance between the sample and CMA entrance. The Ar ion gun and external electron gun are aligned to allow Auger analysis to be performed on the region being sputtered. The spectra shown in Figure 28 were taken in a background pressure of 10^{-9} during a test run on a naturally oxidized Al 2024 unclad sample. Before sputtering, the only visible Auger lines correspond to C, O, and N (not shown). An initial Ar sputtering at 300 eV yielded an Auger spectrum shown on the bottom. The elements present are Al, Cl, C, N, and O. The other spectra were measured after 240 minutes and 390 minutes sputtering. The peak to peak amplitudes of the major elements present are shown as a function of sputtering time in Figure 29. One sees that Cl and C are quickly depleted indicating they were surface contaminants. At around 120 minutes the O and Al amplitudes have grown and leveled off indicating the sampling of the oxide itself. Finally, an indication of Al signal growing and O decreasing, suggesting that a clean Al surface was being approached, but not reached. The source of the Cl was not determined. The C was most likely from hydrocarbons and CO picked up in the air and during pump down.

During this test run, Cu and Mg lines were not carefully measured even though weak signals were observed. More careful scanning will be carried out to characterize these elements. Also, our sputtering rate is rather low and we have plans to increase the ion current by a factor of 2 in the near future.

II.2. Effects of Oxide Aging on Exoemission

It is known that freshly formed anodic oxide coatings on aluminum as well as aluminum alloys change their mechanical properties during a time lasting up to several days. It is thought to change from a relatively soft to a stabilized brittle coating. Since the formation of cracks and, in particular, the initial fracture strain (monitored, e.g. via the onset of exoemission) depend on the mechanical properties, we expected to observe changes in the characteristic exoemission curve as a function of time elapsed after anodization. To test this, we selected aluminum-clad Al 2024 samples, coated with 2000 Å thick dense oxide, produced in an aqueous solution of 0.05 M ammonium tartrate. The dependence of the total emission on the oxide thickness was investigated earlier (compare Fig. 10, Part A; all these samples were measured after stabilization of the oxide). Figure 30 displays the total number of negative particles counted per sample as a function of time after completion of the anodization process. The total number of counts levels off after approximately 120 hours at a value of about 20×10^3 (in agreement with our previous work on aged samples; see Fig. 10). At the same time, the onset of oxide cracking shifts toward smaller strain values as the oxide stabilizes with age. This is in agreement with the expected decrease in the critical fracture strain as the oxide becomes more brittle with age. We also observe that the density of cracks formed in the oxide at the failure strain of the substrate does not increase nearly as much with aging time as does the total exoemission count rate. Thus, the stronger emission from stabilized coatings cannot be accounted for by entirely the formation of more cracks, but could be attributed to an increase in energy released at a propagating crack tip. These studies are in a preliminary stage only. However, they provide yet another example for the sensitivity of the characteristic exoemission curve to change in the physical (mechanical) properties of the oxide coating.

II.3. Different Rinsing Solvents

In this section we report some preliminary findings on the effect of altering the solvents used in rinsing the oxide coating after anodization. Initially we simply asked if such a change would produce a noticeable change in the characteristic exoemission curve. The rinsing procedure is known to influence the adhesion properties of porous oxides.

The procedure used to effect the outermost surface was simply to omit rinsing the sample in distilled water to dissolve and remove the residues from the electrolyte.

Also W. Baun, AFML, in a private communication indicated that rinsing anodized aluminum samples in organic solvents significantly altered the SIMS signals as compared with samples rinsed in distilled water. (This latter result is not well understood at this point.)

Consequently, we produced identical anodized samples, both dense (ammonium tartrate) and porous (H_3PO_4), treating them immediately after anodization in (a) distilled water, (b) benzene, and (c) toluene.

The effect of these solvents on exoemission was significant; compared to the water rinsed samples, the total number of emitted particles decreased drastically (Table IV).

Table IV

Rinse	Dense	Porous
Water	20751	4349
Toluene	7145	123
Benzene	6005	245

Table IV. Total exoemission counts obtained from 2000 Å thick dense and 3000 Å thick porous oxide on aluminum-clad Al 2024 after various rinse procedures.

SEM photographs of the surfaces reveal a marked change in the appearance of upper 20-30% of the oxide layer after rinsing in benzene or toluene. E.g., a very smooth over-layer, roughly 1000 Å thick was found on 3000 Å thick porous oxides. We intend to analyze the make-up of this overlayer with AES. At this point it is too early to comment further on these very interesting findings.

II.4. Deviations from the Baseline Oxide

During actual production of oxide coatings on aluminum alloys such as Al 2024 or Al 7075, the applied potential, the concentration of the phosphoric acid electrolyte as well as its temperature may change. These deviations from the specifications of the anodization process will result in oxides of different thickness, pore structure, and surface texture, and thus, may reduce the quality of the produced coating with respect to its adhesive bonding properties to a primer. If the characteristic exoemission curve is to provide a quality control test for deviations from the production specs, changes in concentration and temperature of the electrolyte must reveal themselves as measurable deviations from the exoemission curve of the Boeing Baseline samples. To test the effect of these changes on the exoemission curve, we have selected aluminum-clad Al 2024 and performed three sets of tests:

1. Only the electrolyte concentration was varied from the 10% baseline concentration. The temperature remained at 74°F and the potential at 10V. The characteristic exoemission obtained with 12% and 8% H_2PO_4 electrolytes curves are shown in Fig. 31 as compared to the usual CEC of the baseline sample.
2. The applied potential was varied and all other anodization parameters remained fixed. The oxide thickness increased considerably at 20V and decreased at 4V anodization potential (Fig. 32 a+b). Corresponding CEC's are shown in Fig. 33. The total exoemission increases considerably with increasing potential.

3. The temperature of the electrolyte was varied and all other anodization parameters remained constant. The texture of the oxide surface tends to get less rough with decreasing temperature and the total exoemission decreases sharply (Fig. 32c, d, and 34).

These results are summarized in Fig. 35. It is obvious the investigated deviations from the desired anodization procedure (baseline procedure) change the properties of the produced coating and that these changes are steadily revealed as deviations in the respective characteristic exoemission curves from that of the baseline curve. These examples support our previous findings (Part A) and are a further indication that the CEC holds promise to be developed into a sensitive quality control test for oxide coatings on aluminum alloys.

II.5. Neutral Emission

As previously discussed, the emission of electrons during elongation was also accompanied by ion and photon emission on pure Al substrates.^(1,2) It occurred to us that the emission of neutral particles might also be observable during the stretching of the sample. Our first experiment was to simply monitor total pressure in the UHV vacuum system (background was $\sim 10^{-9}$ Torr) with a Bayart-Alpert pressure gauge during the elongation of a thick, dense oxide on clad Al 2024. Considerable signal was observed that correlated roughly with the exoelectron emission curve.

We have since repeated the neutral particle emission on a few samples of porous oxide (H_3PO_4), 3500 Å thick, on clad Al 2024. While monitoring total pressure we also take a number of scans on the quadrupole mass spectrometer during the straining of the sample. The ionizer of the mass spectrometer is in direct sight of one side of the sample so that reactive and condensible species would still be detected. The major species observed are O_2 (mass 32) and H_2O

(mass 18). Also observed are CO_2 (mass 44) and possibly mass 28 (N_2 or CO), and mass 40 (Ar). Figure 36 shows the emission curves for H_2O and O_2 as well as the total pressure rise. These major components, when added together fit the total pressure curve quite well. Note that the total pressure does not come down to near its original value until after the rupture of the sample. Also there is a large burst of gas at the rupture indicating considerable gas release from the sample.

A comparison of the neutral emission and electron emission for similar samples is shown in Figure 37 and 38. The main peaks of the curves agree closely but the neutral emission starts almost immediately with elongation and falls much slower, indicating emission even after cracks stop propagating.

Although the number of samples investigated is limited, we can say that so far, neutral emission has been detected on all samples that are exoelectron emitters. Also the shape relates to the exoelectron curve as shown in Fig. 35.

The distinct differences between the neutral and electron emission suggests that the mechanism for neutral emission is somewhat different. Clearly, the requirement for emission of the neutral particles involves (a) exposure of bound molecules to the solid-vacuum interface, and (b) desorption--either stimulated or thermal. The propagation of cracks in the oxide could certainly expose gas molecules occluded into the oxide layer during anodization. The crack tip is a localized hot spot which could provide sufficient thermal energy for desorption or possibly stimulation into an excited anti-bonding state (similar to electron-stimulated desorption).

The substantial emission which occurs after the electron emission has fallen could be due to bonds being broken between the oxide and aluminum substrate due to the continued plastic deformation of the substrate. The location

of these bonds would allow neutral emission but drastically limit charged particle emission. Also the energy available by this mechanism is far less than the cracking of the oxide, which again favors neutral emission over charged particle emission.

The burst of neutrals at the rupture of the sample could be due to acoustic emission of adsorbed gases or possibly a relaxation effect.

The explanations presented here are only tentative. It should be clear, however, that neutral emission could provide another characteristic curve which in many ways compliments the charged particle emission and merits further investigation.

VIII. SUMMARY

A Variety of characteristic exoemission curves (rate of charged particle emission vs. strain during tensile deformation) have been measured for a number of different oxide covered aluminum alloy samples. We have shown that samples treated in the same fashion yield very reproducible exoemission curves. For a few cases we have qualitatively compared the crack distributions on the elongated samples and the basic features of the exoemission. Our results to date support our working hypothesis that a particular substrate-oxide layer system will yield a unique characteristic exoemission curve. In the case of samples oxidized at the Boeing Commercial Airplane Company, only slightly different conditions (e.g., changes in the acid concentration or a change in the anodizing temperature) produced readily detectable changes in the exoemission. We thus conclude that this unique type of emission may well serve as a quick and inexpensive test of the quality of an oxide layer.

References

1. B. Z. Rosenblum, J. P. Carrico, P. Braunlich, and L. Himmel, J. Phys. E., Scientific Instruments 10 (1977), in print (see Attachment A).
2. B. Z. Rosenblum, P. Braunlich, and L. Himmel, J. Appl. Phys (Nov. 77), in print (see Attachment B).
3. D. R. Arnott and J. A. Ramsey, Surf. Sci. 28, 1 (1971).
4. E. Linke, Z. Angew Physik 29, 241 (1970).
5. B. Sujak and A. Gieroszynski, Acta Phys. Pol. 28, 311 (1965).
6. B. Sujak, A. Gieroszynski, and E. Pega, Acta Phys. Pol. 28, 61 (1965).
7. W. J. Baxter, Vacuum 22, 571 (1972).
8. K. Becker, "Critical Review in Solid State Sciences," 3, 39 (1972).
9. T. F. Gesell, E. F. Arakawa, and T. A. Callcott, Surf. Sci. 20, 174 (1970).
10. B. Sujak and A. Gieroszynski, Acta. Phys Pol. A37, 733 (1970).
11. N. T. McDevitt, W. C. Baun, and J. S. Solomon, Technical Report, AFML-TR-15-122.
12. W. L. Baun, Technical Report, AFML-TR-76-30 (1976).
13. W. L. Baun, T. J. Wild, and J. S. Solomon, Technical Report, AFML-TR-76-70.
14. J. A. Marceau and J. C. McMillan, Technical Report AFML-TR-76-173.
15. N. T. McDevitt, W. L. Baun, G. Fugate, and J. S. Solomon, Technical Report, AFML-77-55.
16. G. A. Alers, P. L. Flynn, and M. J. Buckely, Materials Evaluation 35, 73 (1977).

Acknowledgment:

The authors gratefully acknowledge support of this work by the Bendix Corporation through donation of equipment.

Figure Captions

1. Shape of the 0.051 cm thick test samples.
2. Schematic of pulse handling system.
3. Typical stress-strain curve obtained by increasing the strain with time at a constant rate.
4. Raw data obtained from a strong exoemitter (Al 2024 clad, covered with 3000 Å thick dense oxide). The upper curve represents the recorded display of the multichannel analyzer, the lower one is a strip chart recording of the rate-meter output obtained with a 5 sec response time.
5. Data obtained from a weak exoemitter (Al 2024 clad, porous oxide, Boeing Baseline--see Section III). Display of
 - a) multichannel analyzer
 - b) strip chart recording of rate meter
 - c) characteristic exoemission curve obtained with the curve smoothing technique described in Section VII.4.
6. Emission of negative particles from aluminum-clad Al 2024 covered with 4000 Å thick dense oxide as a function of strain. The dependence of the stress on the pulling time is shown for comparison.
7. SEM photographs of cracks in porous oxides on clad Al 2024. The nominal thickness of the oxides is a) 3500 Å and b) 4000 Å. However, these photographs indicate that the thickness must be reversed. We first discovered this interchange as an apparent anomaly in the exoemission curves.
8. Exoemission curves obtained from aluminum-clad Al 2024 covered with porous oxide (upper figure) and the associated stress-strain curves (lower figure).
9. Dependence of the total exoemission obtained from aluminum-clad Al 2024 covered with porous oxide. The arrows indicate corrections made after measuring the correct thickness of the samples with the aid of SEM techniques (Fig. 7) (See Section VII.1.2). The encircled points represent data which do not reproduce similar measurements made on nominally identical samples.
10. Dependence of the total emission of negative particles on oxide thickness emitted from aluminum clad Al 2024 covered with porous or dense oxides.
11. Position (increase of strain after onset of plastic deformation) of the main exoemission peak as a function of oxide thickness. These results were obtained from aluminum-clad Al 2024 covered with dense or porous oxides.

12. The full width at half maximum of the main exoemission peak as a function of oxide thickness measured on aluminum-clad Al 2024 covered with dense or porous oxide.
13. Exoemission curves and stress-strain curves measured on bare Al 2024 samples.
14. Total exoemission and peak height of the main peak as a function of thickness of dense oxide on bare Al 2024.
15. Position (increase of strain after onset of plastic deformation) of the main exoemission peak as a function of the thickness of dense oxide on bare Al 2024.
16. The full width at half maximum of the main exoemission peak as a function of the thickness of dense oxide on bare Al 2024.
17. Exoemission curve and stress-strain curve obtained from bare Al 7025 covered with 4000 Å thick dense and porous oxides.
18. Total exoemission as a function of oxide thickness obtained from bare Al 7025 covered with dense and porous oxides.
19. Position of the main exoemission peak as a function of oxide thickness on bare Al 7025 covered with dense and porous oxides.
20. Full width of half maximum of the main exoemission peak as a function of oxide thickness measured on bare Al 7025 covered with dense and porous oxides.
21. SEM photograph of an edge of a Boeing Baseline oxide layer on clad Al 2024. From the photograph, the oxide thickness is seen to be approximately 3500 Å.
22. Photomicrographs of the four Boeing oxides on clad Al 2024 after being strained to the rupture point. The magnification of each photograph is 200X.
23. Exoemission curves obtained from a Boeing Baseline sample and a 4 V sample (aluminum-clad Al 2024, porous oxide).
24. Exoemission curve measured on a Boeing 20 V sample (aluminum-clad Al 2024, porous oxide).
25. Exoemission curves smoothed by the averaging techniques described in Section VII.4. obtained from the Boeing Baseline sample B-2C-7 and the Boeing Baseline 4V-8-65-C-2. Both aluminum-clad Al 2024 substrates were covered with porous oxide of different thickness.
26. Exoemission curves from a Boeing Baseline sample (a) and a Boeing "without etch" sample (b) (aluminum-clad Al 2024, porous oxides).

27. "Smoothed" exoemission curves, obtained from two nominally identical Boeing Baseline samples, shown to demonstrate the reproducibility of the data that was achieved even for weak exoemitters. Curve (c) is the smoothed version of rate meter data shown in Fig. 26 (b).
28. Auger spectra of bare Al 2024 for various sputtering times: (a) no sputtering, (b) 240 minutes sputtering, (c) 390 minutes sputtering.
29. Peak heights of prominent Auger lines obtained from bare Al 2024 as a function of ion sputtering time.
30. Total number of negatively charged particles emitted from clad Al 2024 samples covered with 2000 Å thick dense oxide as compared to the crack density and the onset of emission (initial fracture strain) for samples of different age after anodization.
31. CEC's obtained from porous oxide coatings by changing only the electrolyte concentration from the Boeing baseline procedure. The wt percentages used are indicated on the curves.
32. SEM photographs of cracked oxides obtained from the Boeing baseline sample (center) and from samples obtained by changing the anodizing potential to 20V (a) and 4V (b) and by changing the temperature of the electrolyte to 85° F (c) and 65° F (d).
33. CEC's obtained from porous oxides by changing the anodizing potential to 20V and 4V as compared to the 10V used in the Boeing baseline procedure.
34. CEC's obtained from porous oxides by changing the electrolyte temperature to 85° F and 65° F as compared to the 74° F used in the Boeing baseline procedure.
35. Total number of counted negative particles obtained from oxides that were produced by varying anodization parameters of the Boeing baseline procedure. The data are averages obtained from 3 to 6 samples each.
36. Emission of neutral particles (O_2 and H_2O) from clad Al 2024 covered with 3500 Å thick porous oxide. The upper two graphs display the intensity of H_2O and O_2 emission and the lower graph the total emission of neutral particles as compared to the sum of the emission intensities of O_2 and H_2O .
37. Total rate of neutral emission as compared to the emission rate of the negative particles obtained from 3500 Å thick porous oxide on clad Al 2024.
38. Total rate of neutral emission as compared to the emission rate of negative particles obtained from 3000 Å thick dense oxide on bare Al 2024.

List of Publications

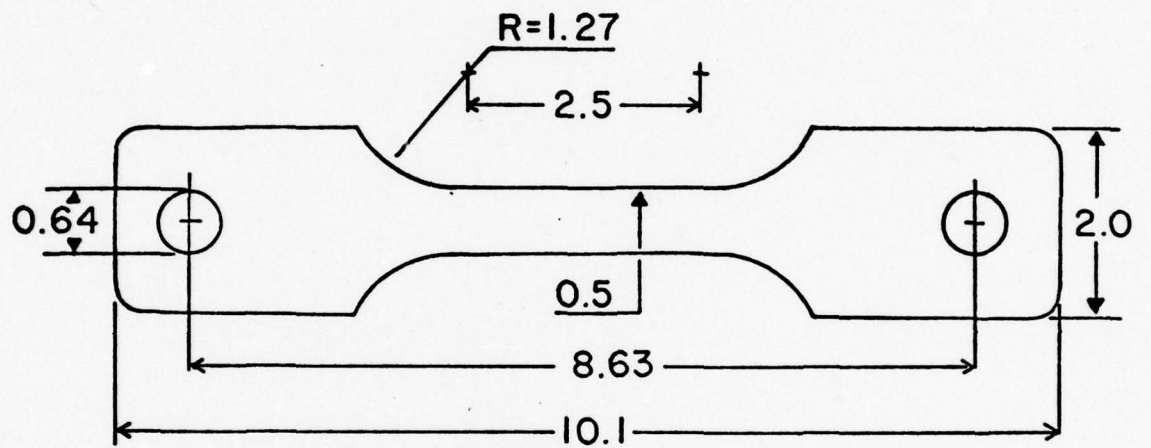
1. B. Rosenblum, P. Bräunlich, and L. Himmel; J. Appl. Phys. 48, 5262 (1977).
2. B. Rosenblum, J. P. Carrico, P. Bräunlich, and L. Himmel; J. Phys. E: Scient. Instr. 10, 1056 (1977).
3. J. T. Dickinson, P. F. Bräunlich, L. Larson, and A. Marceau; paper presented at the AMS-AIME--Chicago Meeting, Oct. 24, 1977.
4. J. T. Dickinson, P. F. Bräunlich, L. Larson, and A. Marceau; "Characteristic Emission of Negatively Charged Particles During Tensile Deformation of Oxide-Covered Aluminum Alloys"; accepted for publication in Appl. Surf. Sc.
5. D. L. Doering, T. Oda, J. T. Dickinson, and P. Bräunlich; "Characterization of Anodic Oxide Coatings on Aluminum by Tribo-stimulated Exoemission"; to be submitted to Appl. Surf. Sc.
6. L. Larson, J. T. Dickinson, P. F. Bräunlich, and D. B. Snyder; ABSTRACT: "The Emission of Particles from Anodized Aluminum Surfaces During Tensile Deformation." To be submitted to 25th National Vacuum Symposium, American Vacuum Society.
7. T. Oda, J. T. Dickinson, and P. F. Bräunlich; ABSTRACT: "Thermally Stimulated Particle Emission from NaCl after Electron Sputtering." To be submitted to 25th National Vacuum Symposium, American Vacuum Society.

List of Personnel

- | | |
|---------------------|--|
| 1. P. Braunlich: | Assoc. Prof. of Physics, Principal Investigator |
| 2. J. T. Dickinson: | Assoc. Prof. of Physics, Co-Principal Investigator |
| 3. Larry Larson: | Graduate Student (Ph.D. Candidate) |
| 4. Toshiyuki Oda: | Assistant Professor of Physics (Visiting Scientist
from Oita University, Japan) |
| 5. Ansgar Schmid: | Research Associate (temporary help) |

Coupling Activities

We have established a cooperation with the Boeing Commercial Airplane Company in Seattle. Specifically, we work together with Dr. Art Marceau on possible applications of the exoemission method to quality control of oxide coatings on alloys which are produced to facilitate adhesive bonding. In addition, we have tested samples from Grumman Aerospace Division, Bethpage, New York. Dr. Gary Geschwind, from Grumman, is interested in using exoemission phenomena to detect fatigue crack initiation on the surface of various alloys. We plan to investigate whether chemi-emission or the newly discovered emission of neutral particles can be utilized for this purpose. If these initial tests prove to be successful, we plan to use them as a basis for a joint proposal to the Navy or Air Force at a later date.



ALL DIMENSIONS IN CENTIMETERS

Fig. 1

PULSE HANDLING SYSTEM

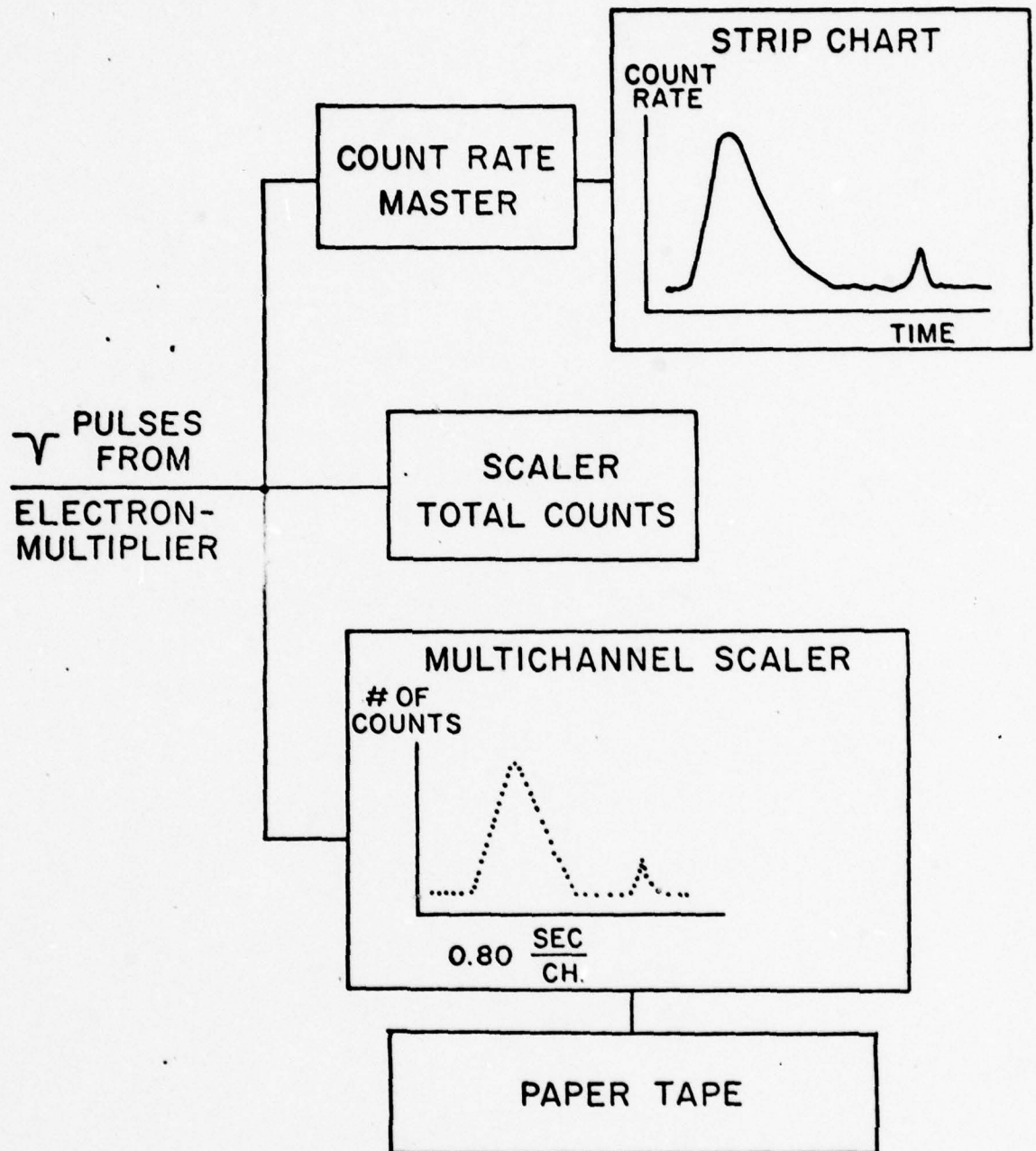


Fig. 2

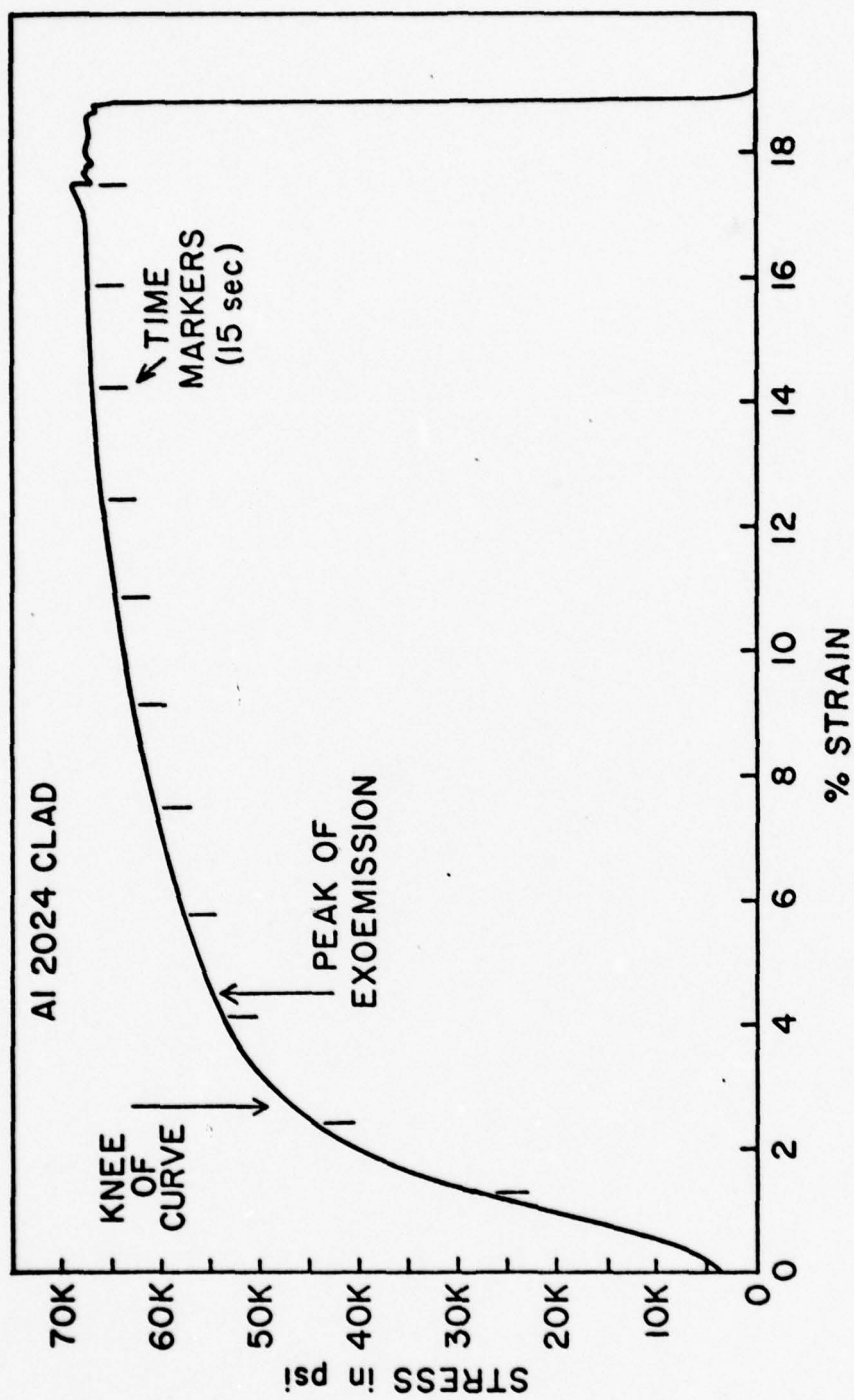


Fig. 3

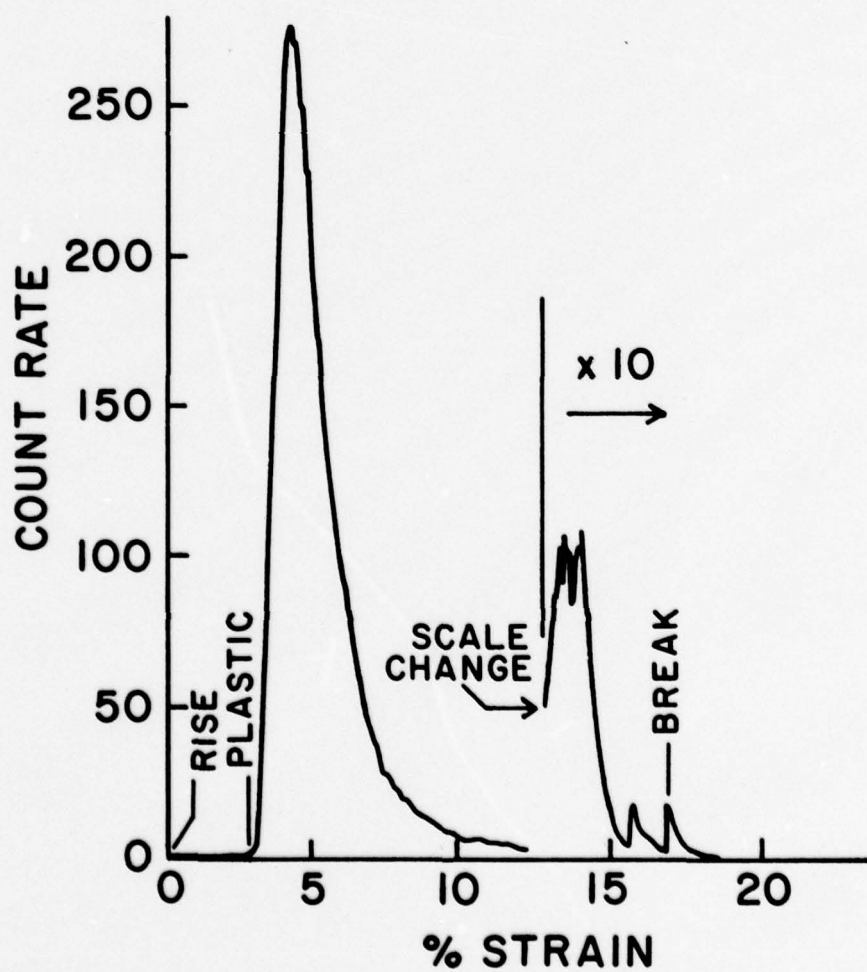
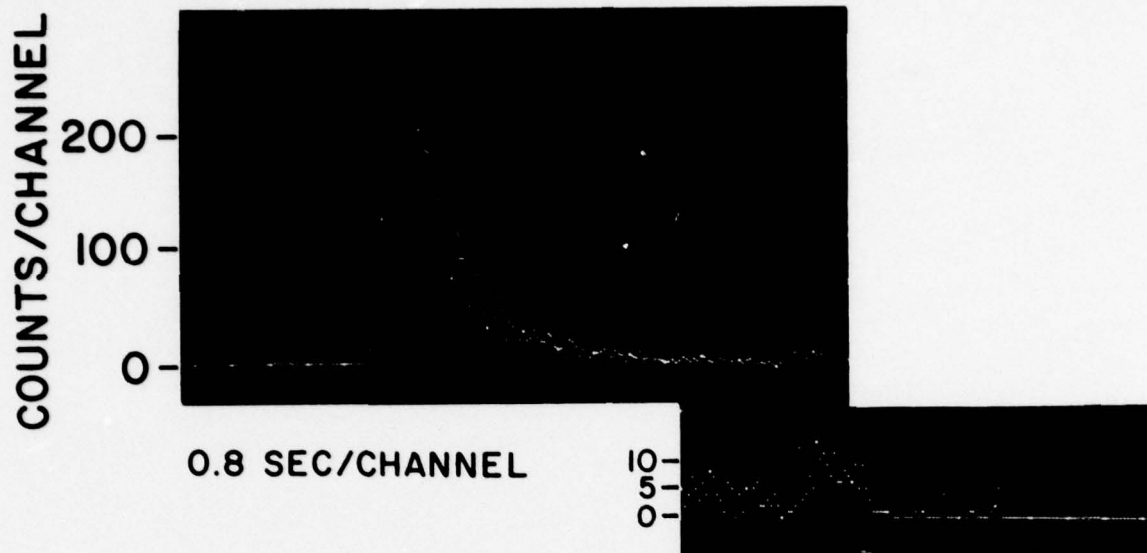
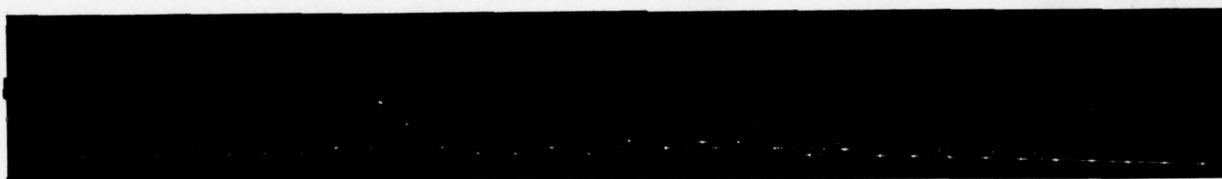


Fig. 4

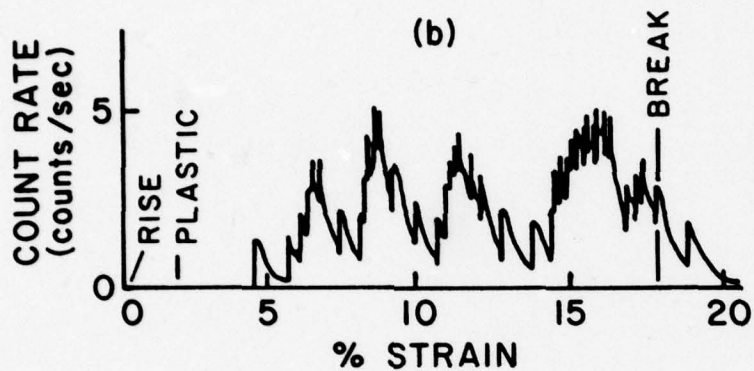
(a)

COUNTS/
CHANNEL



0.8 SEC/CHANNEL

(b)



(c)

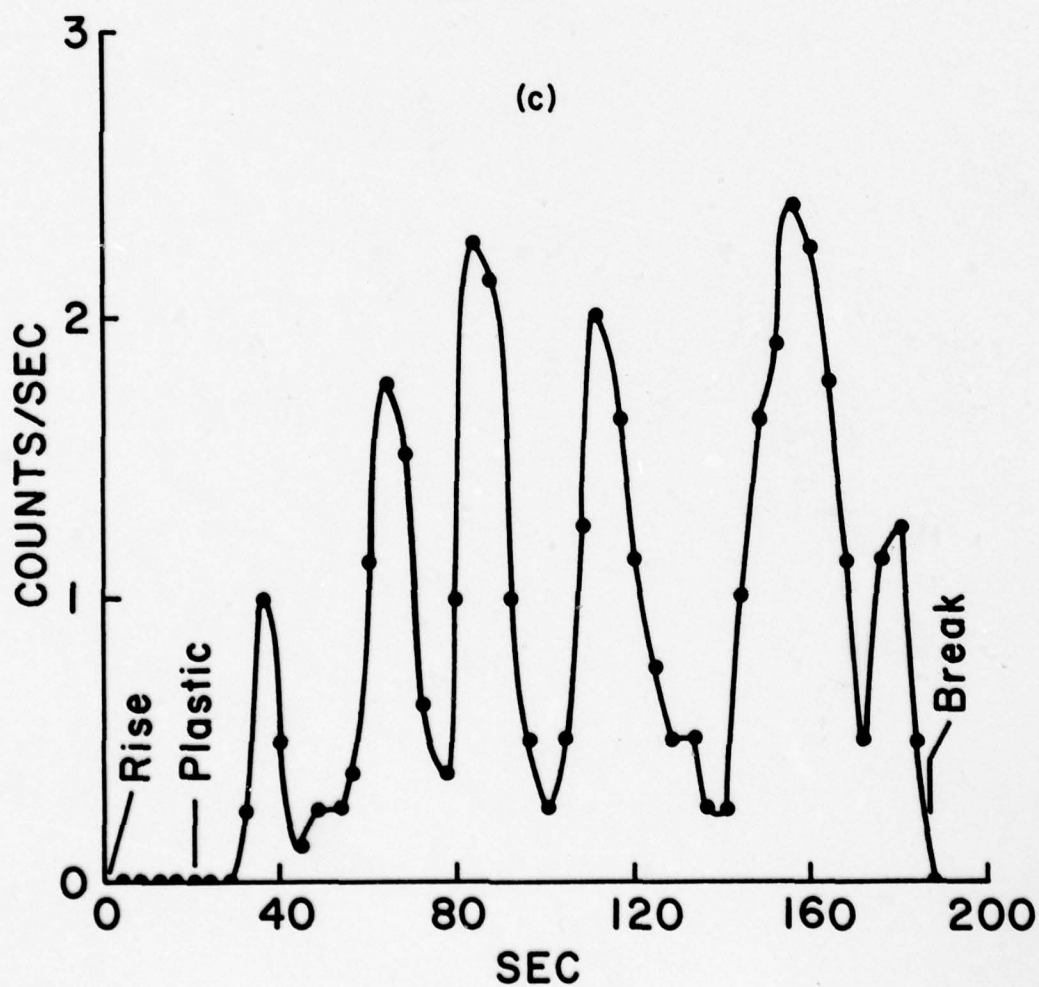


Fig. 5

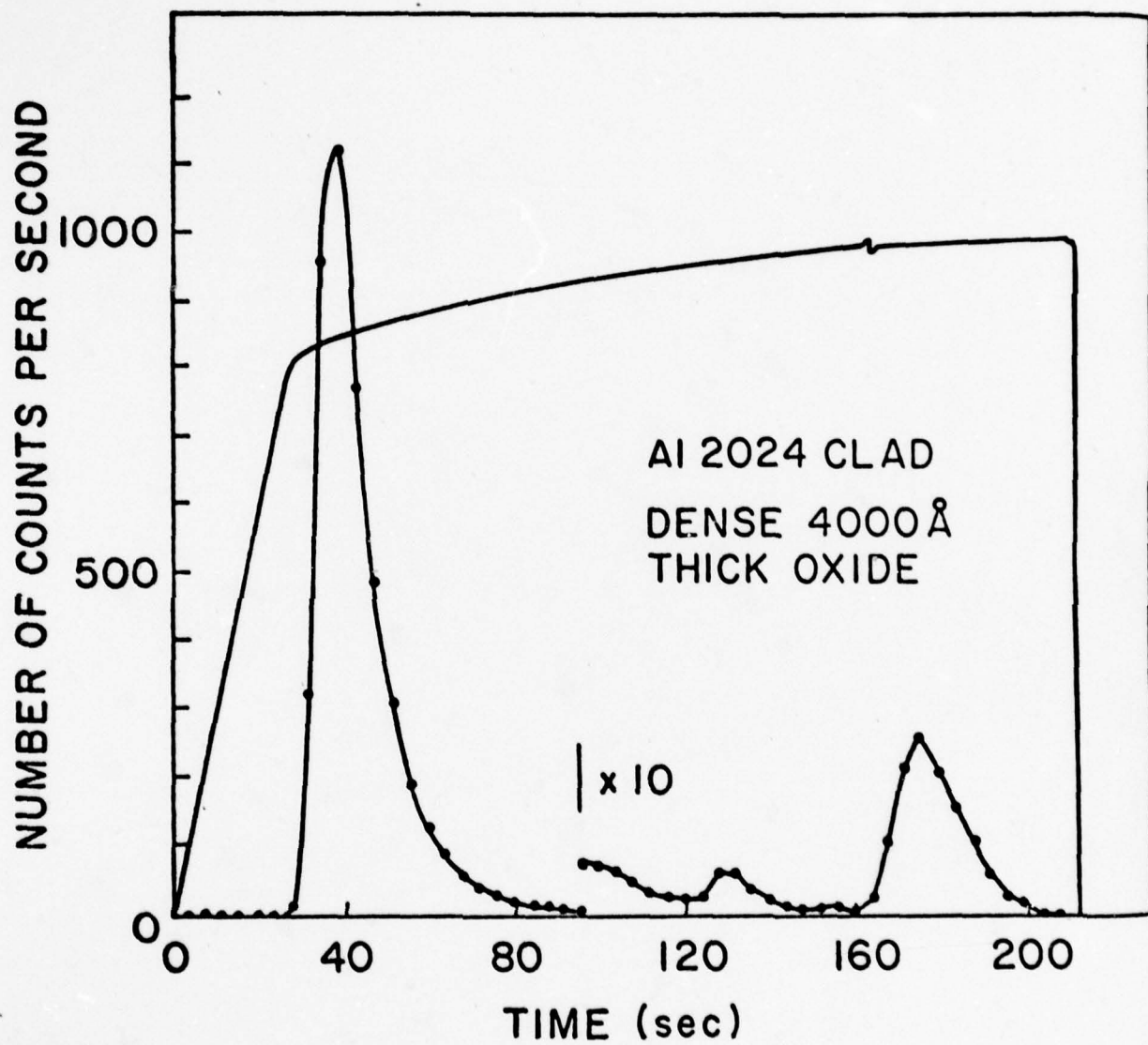


Fig. 6

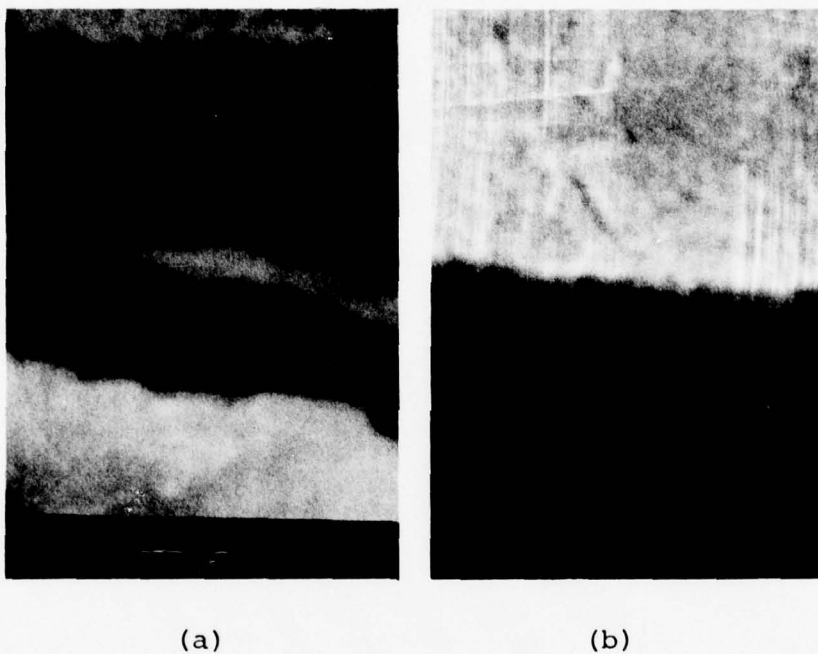


Figure 7 . SEM photographs of cracks in porous oxides on 2024 clad Al. The nominal thickness of the oxides is a) 3500 Å and b) 4000 Å. However, these photographs indicate that the thickness must be reversed. We first discovered this interchange in an apparent anomaly in the exoemission curves.

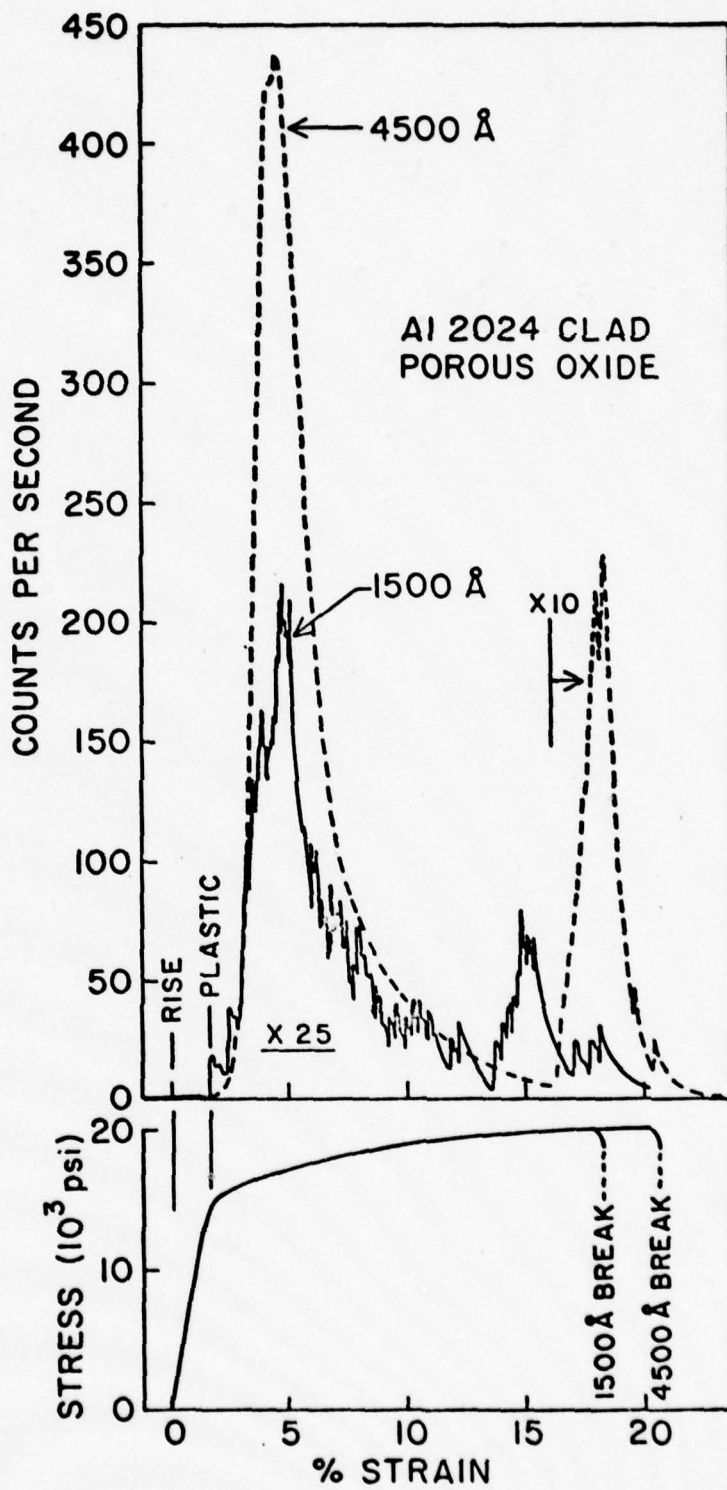


Fig. 8

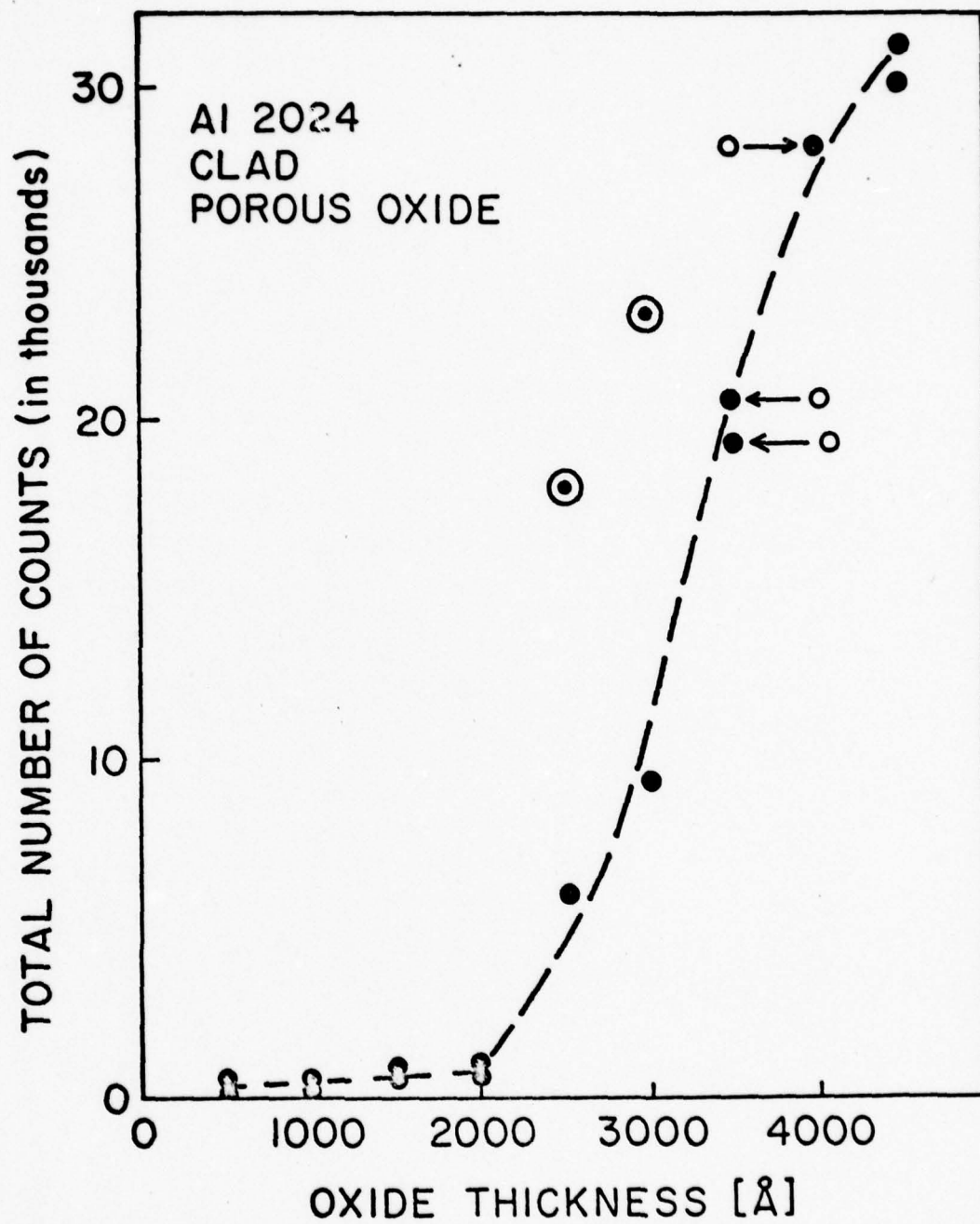


Fig. 9

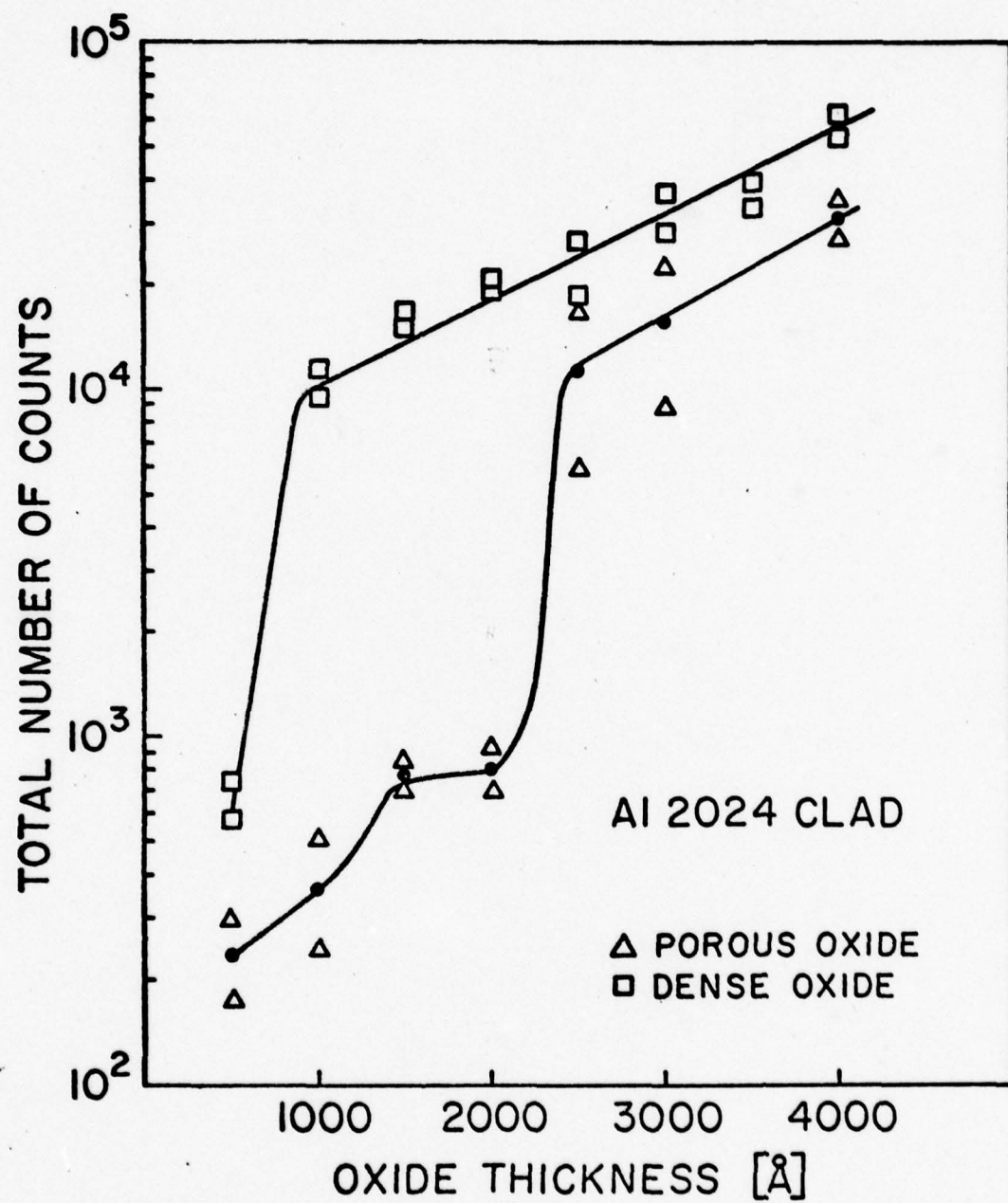


Fig. 10

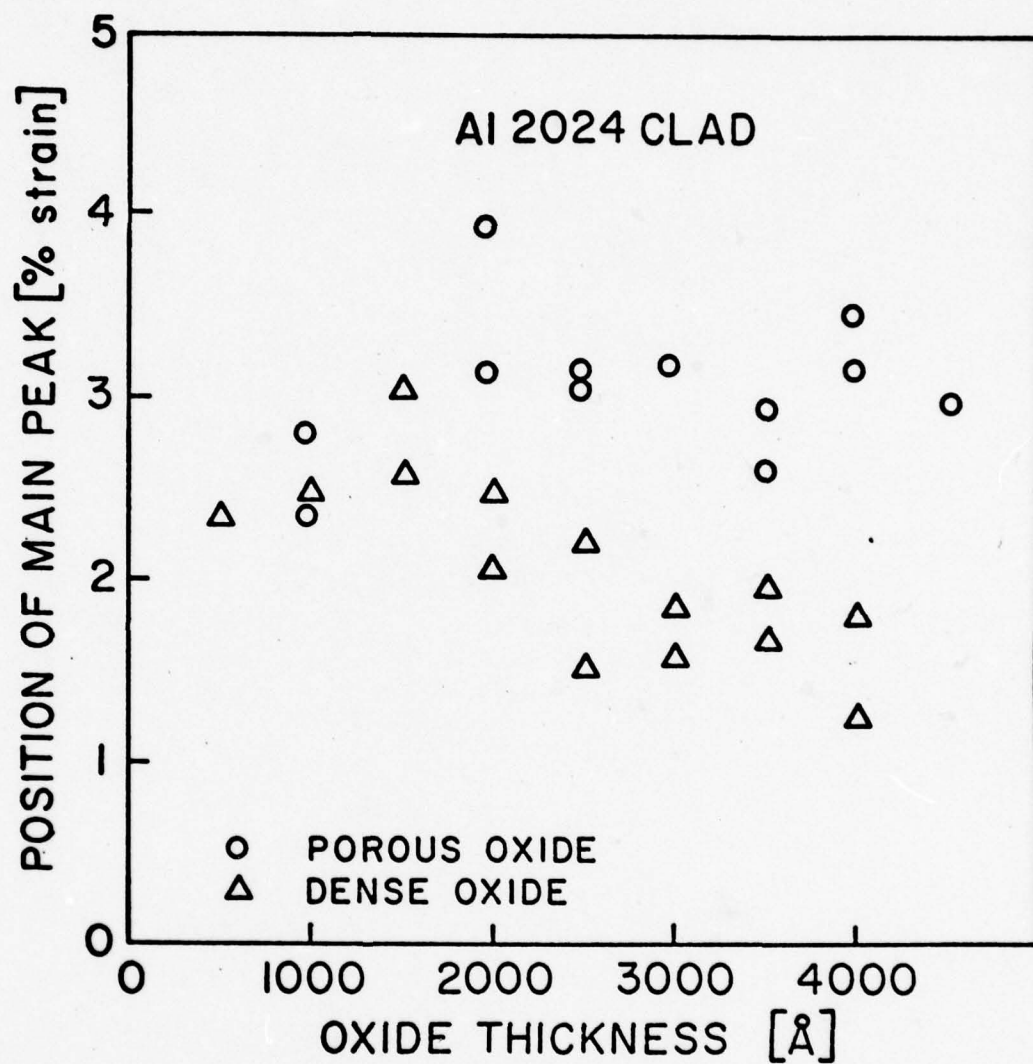


Fig. 11

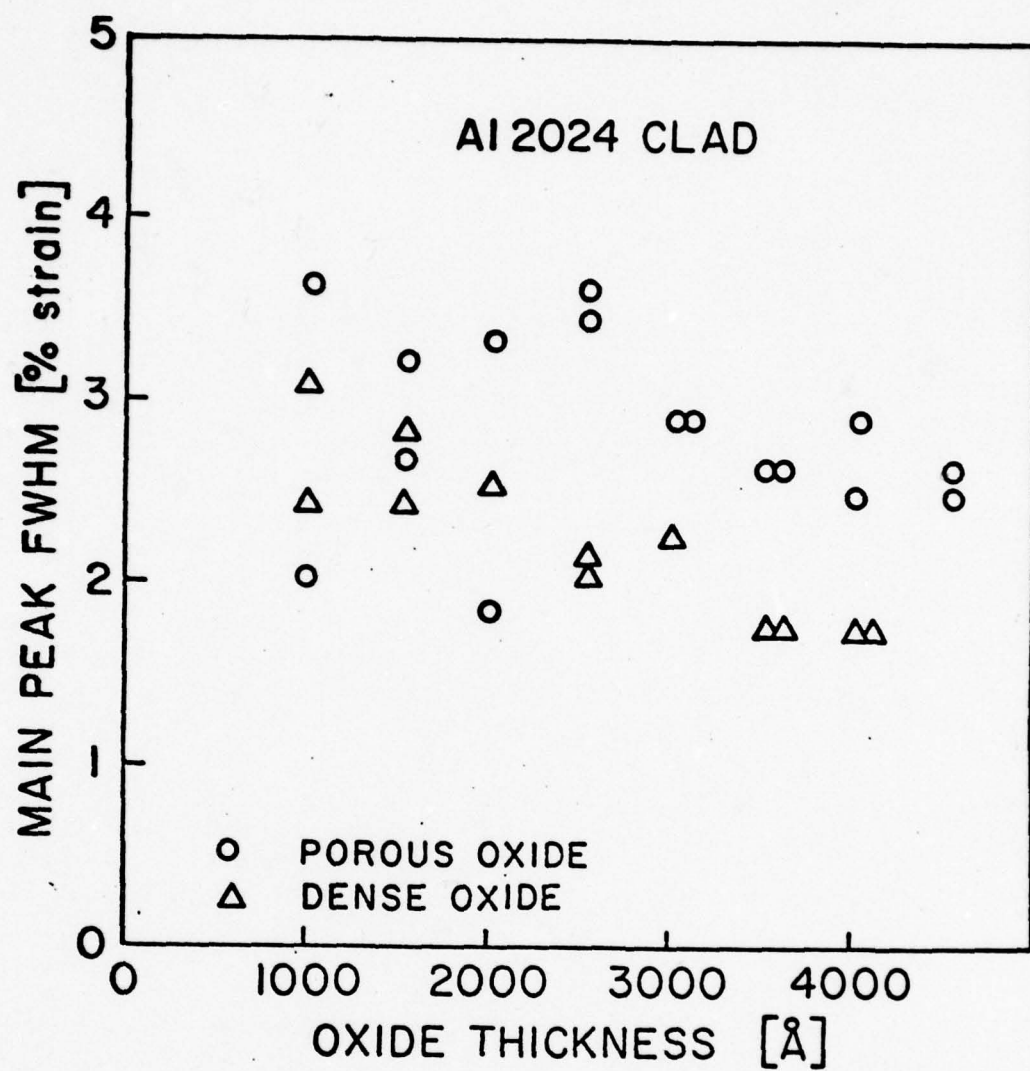


Fig. 12

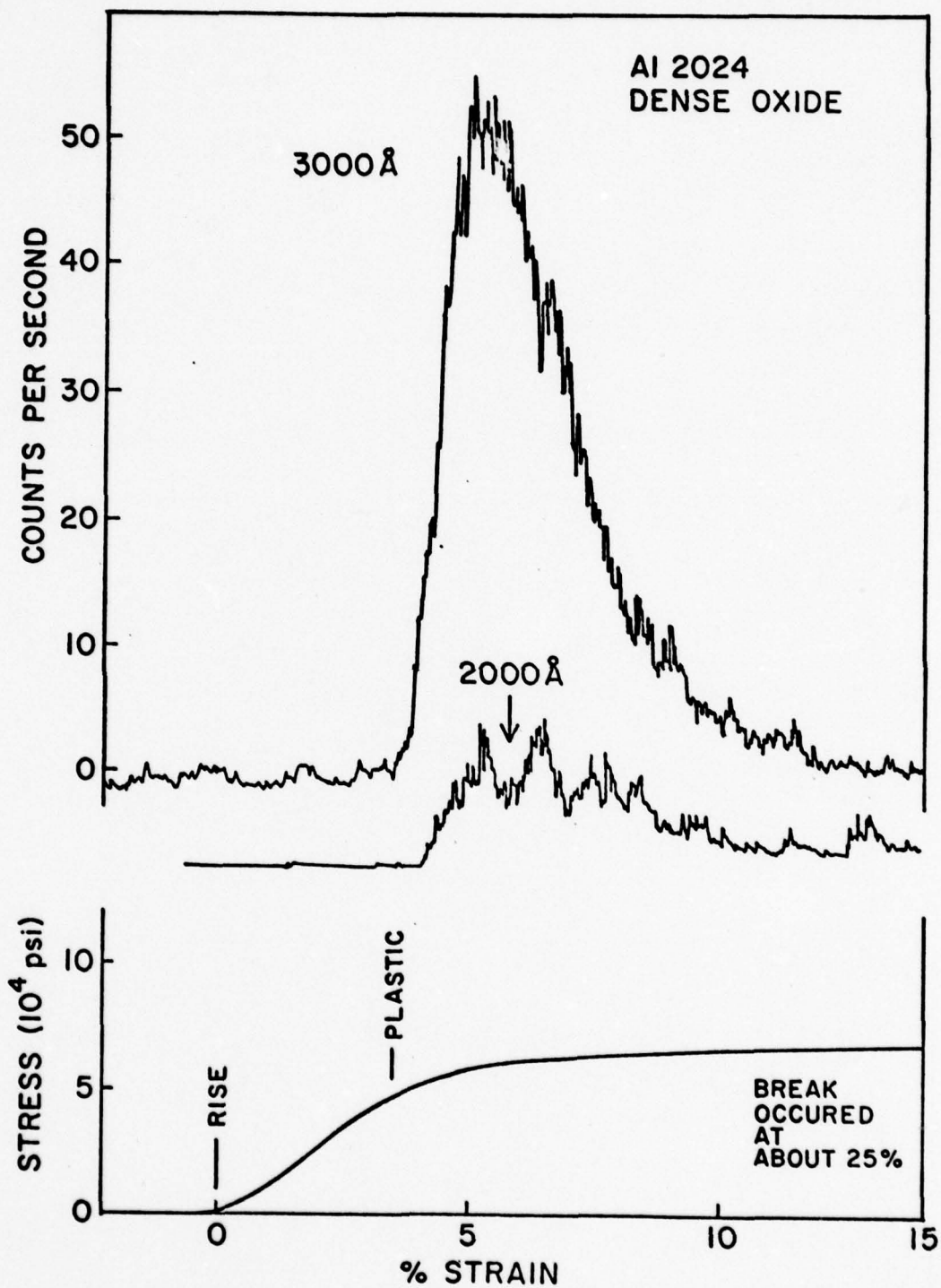


Fig. 13

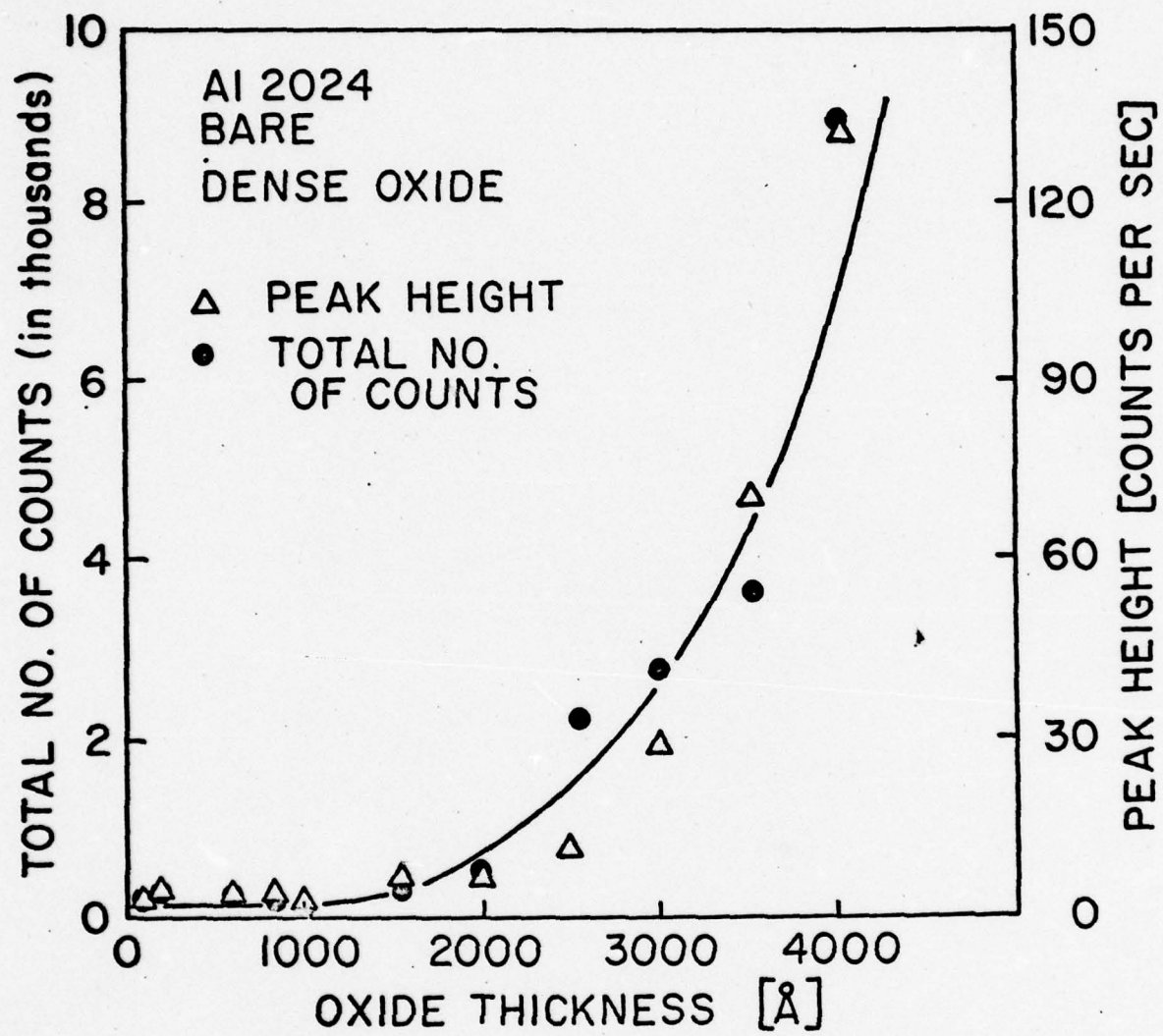


Fig. 14

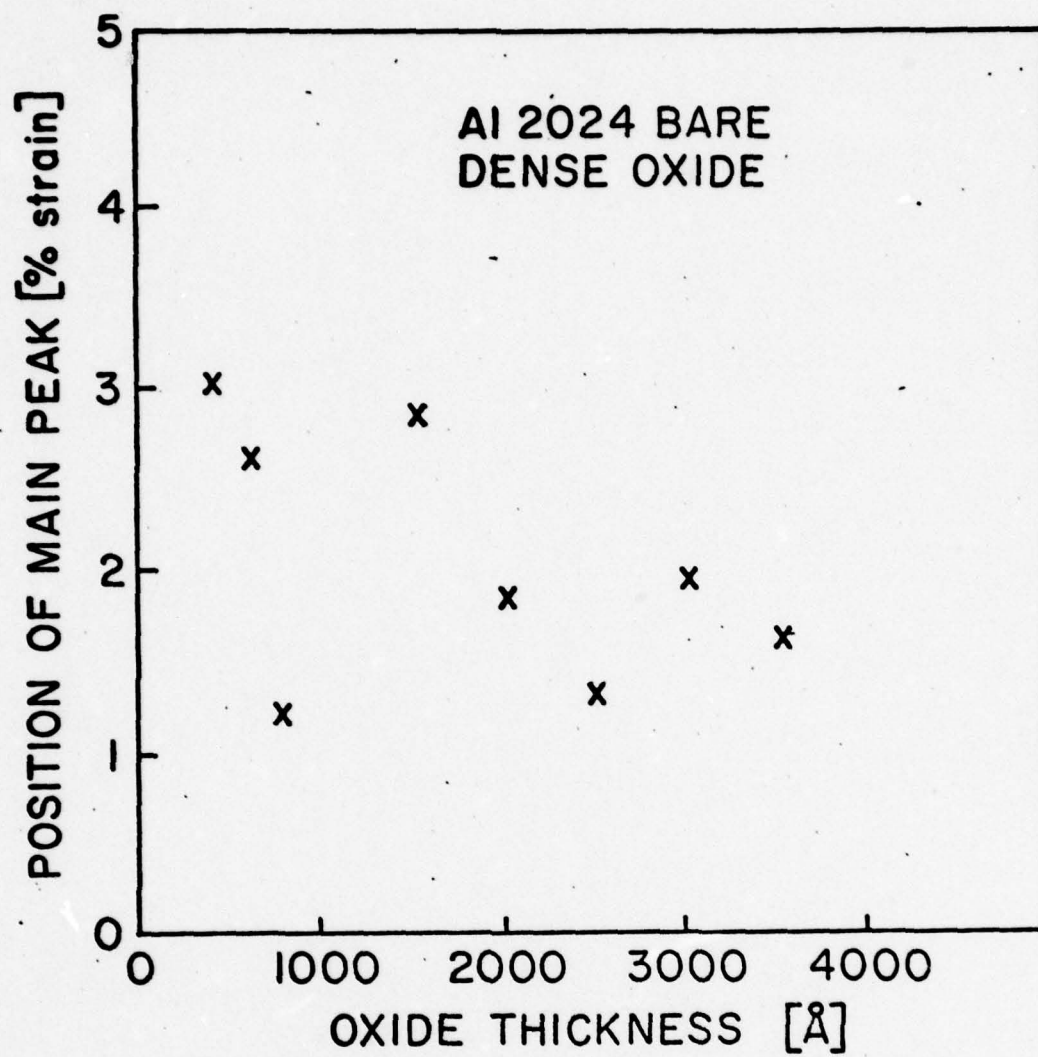


Fig. 15

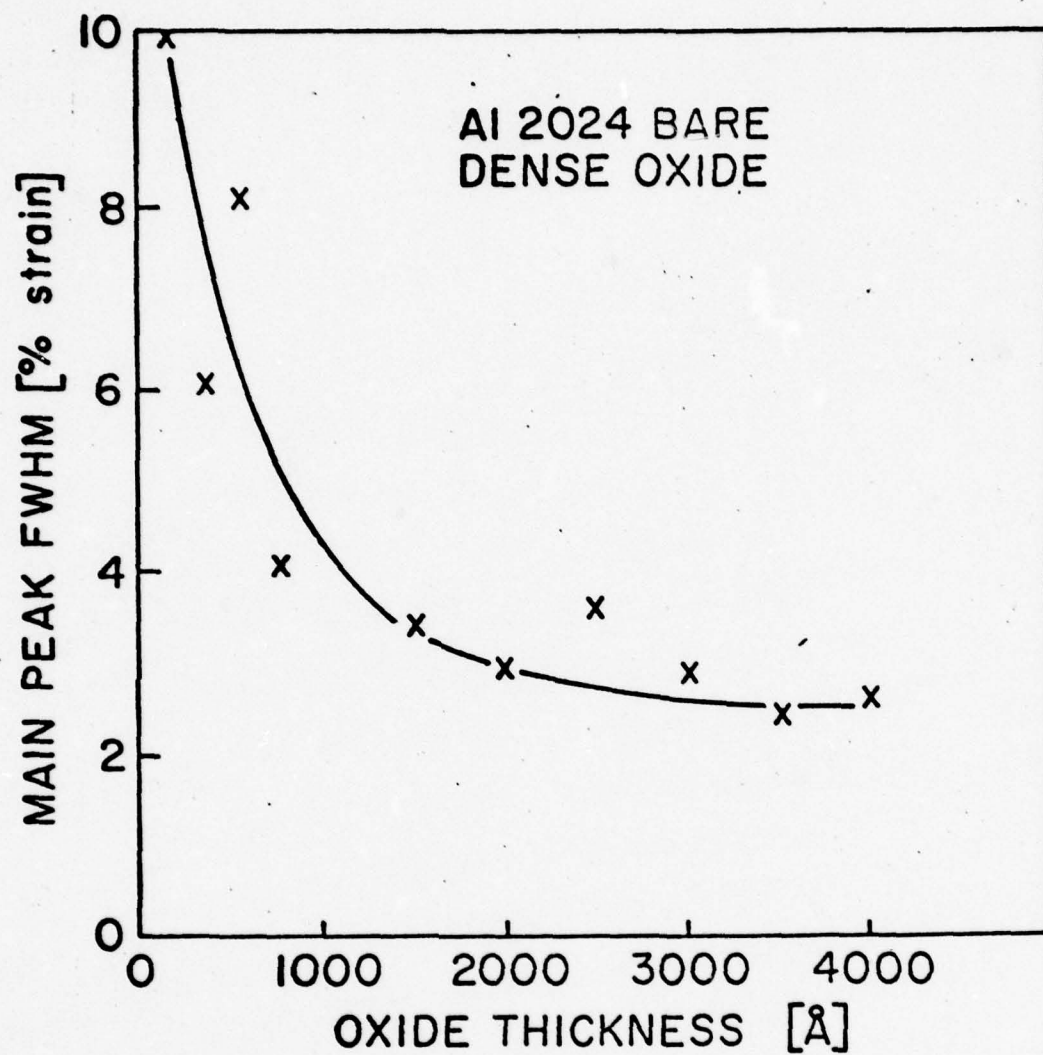


Fig. 16

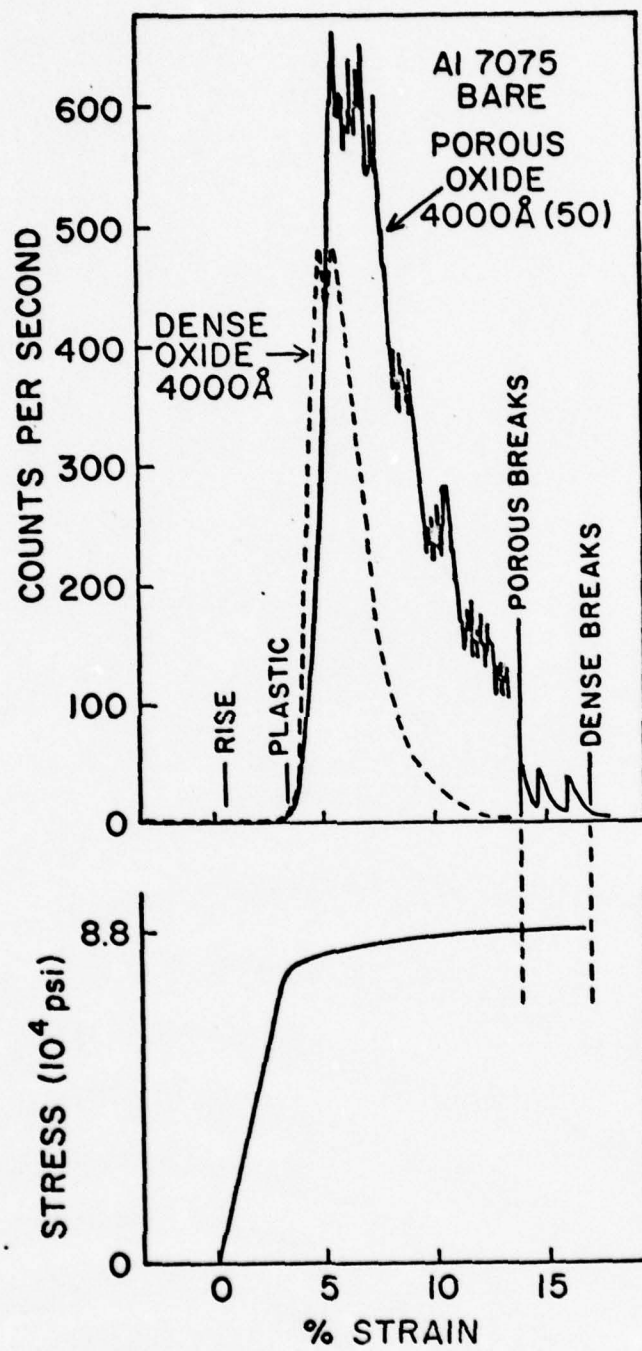


Fig. 17

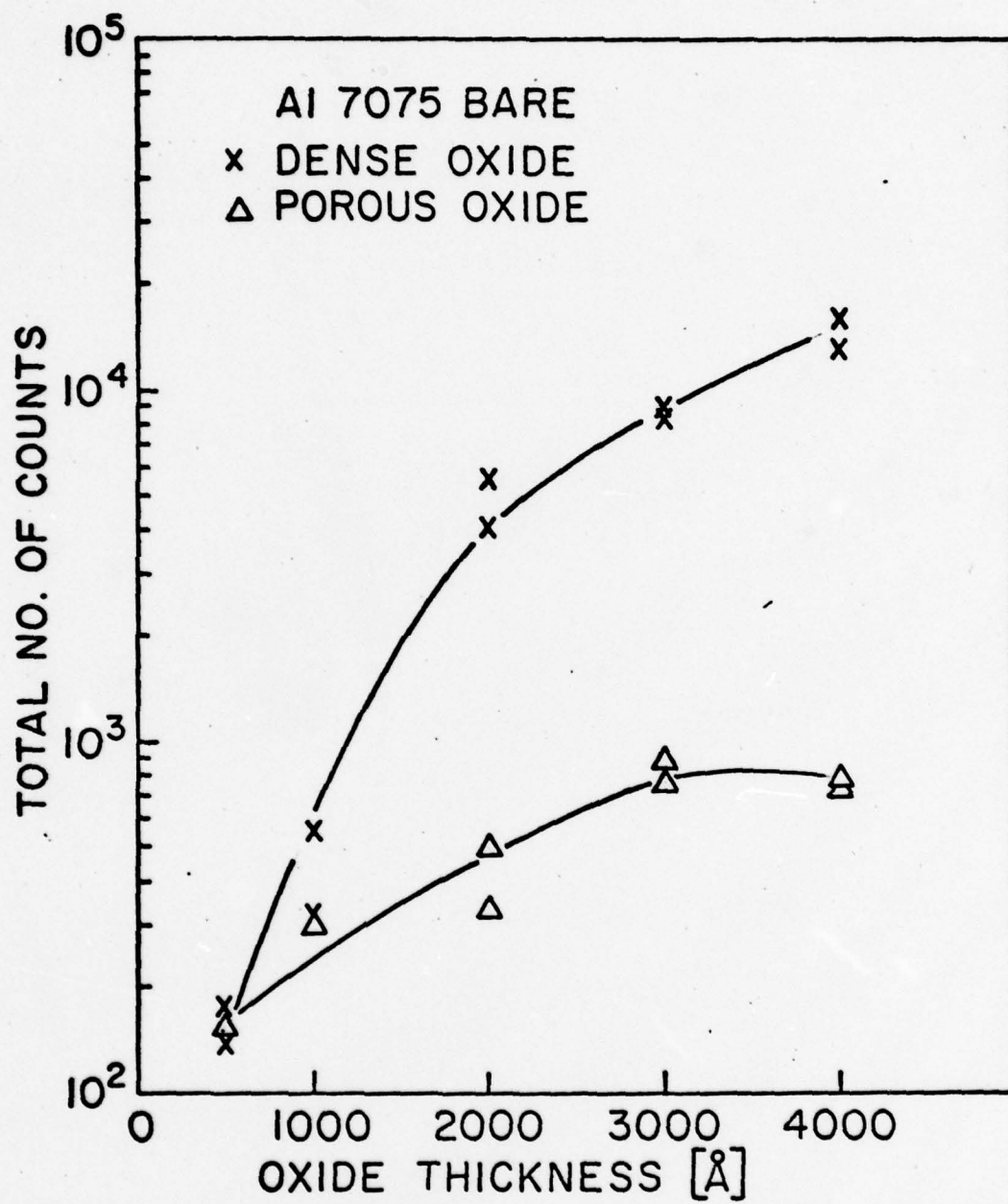


Fig. 18

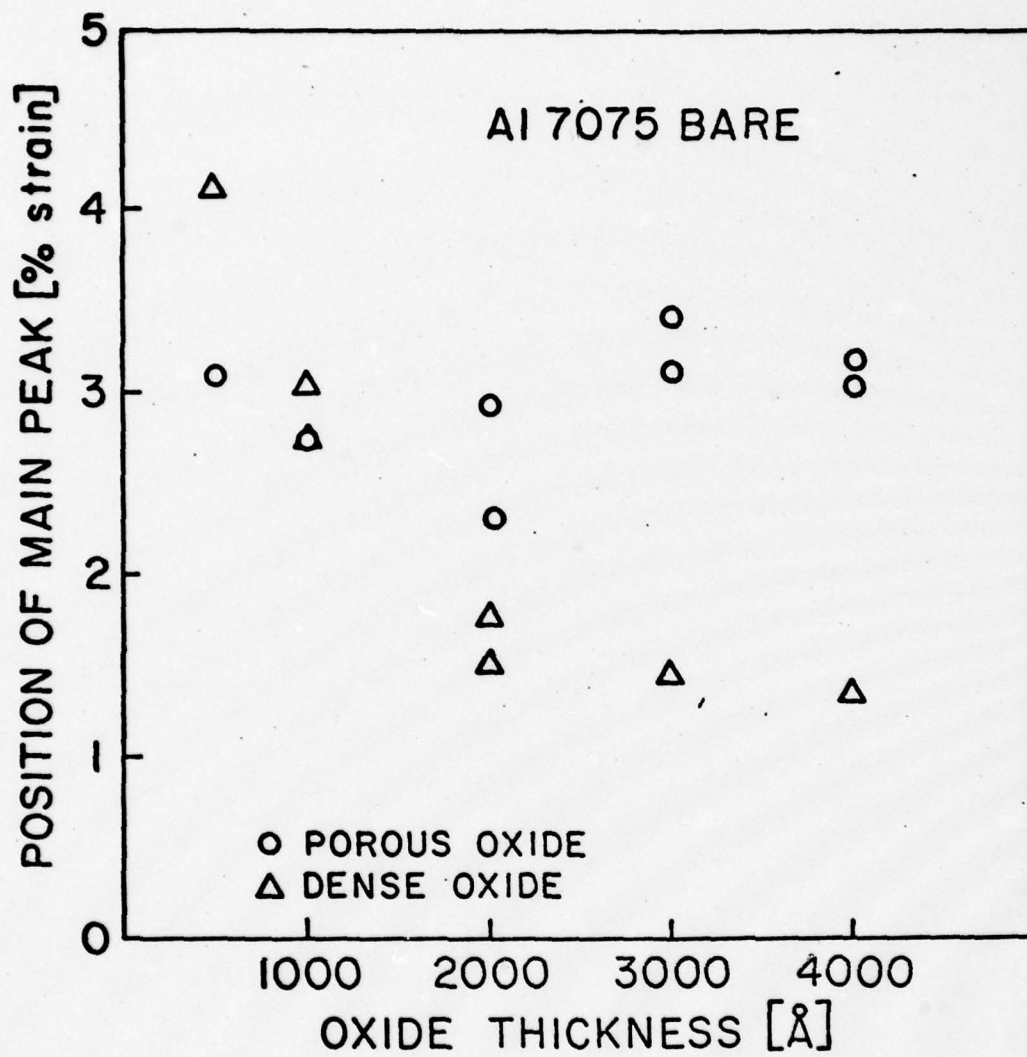


Fig. 19

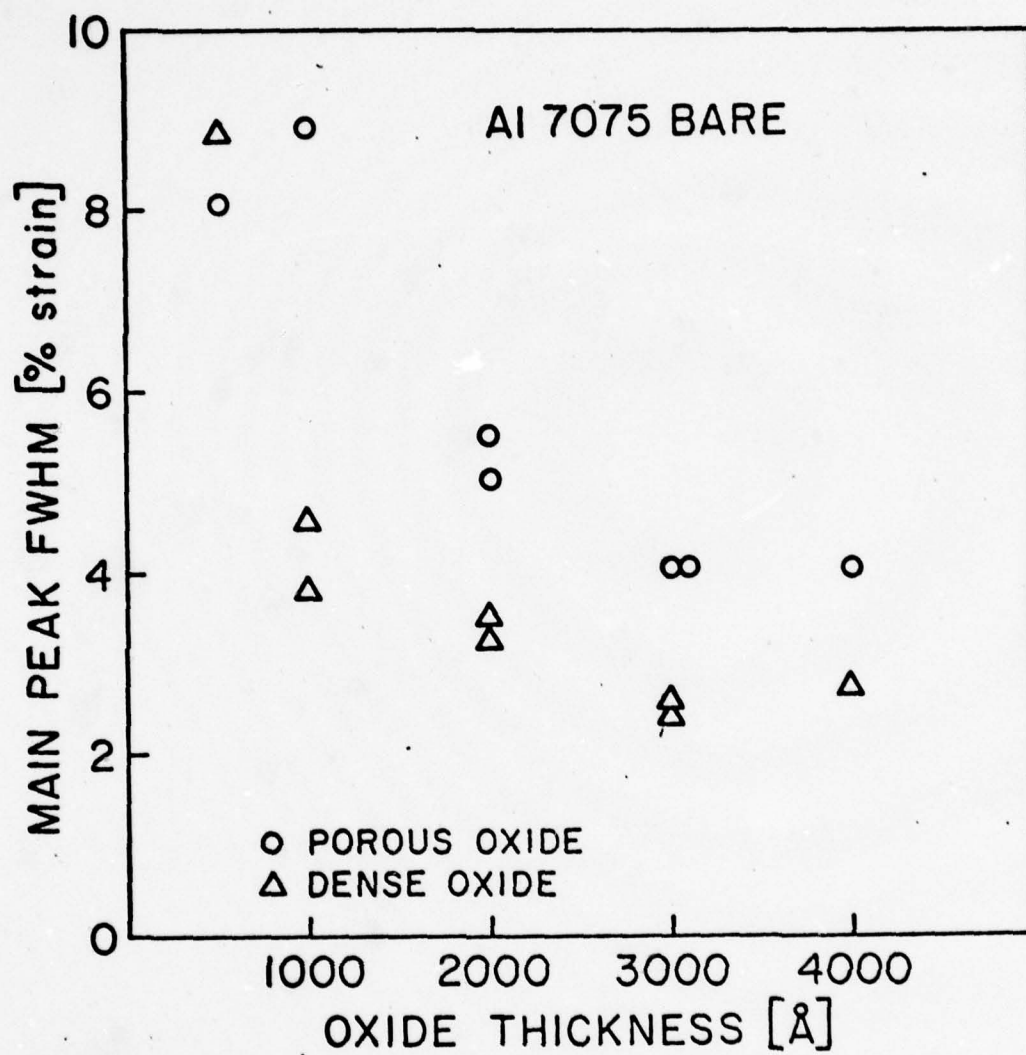
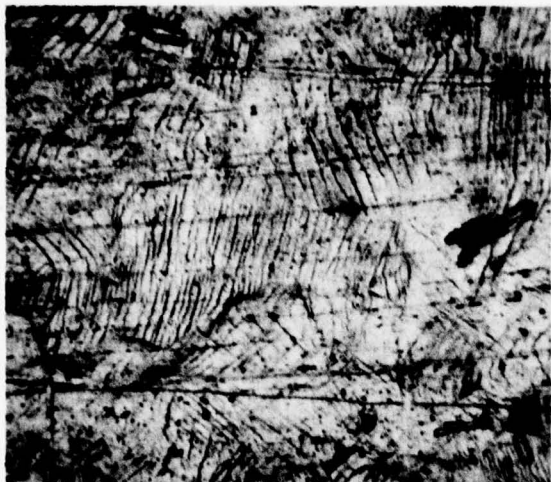


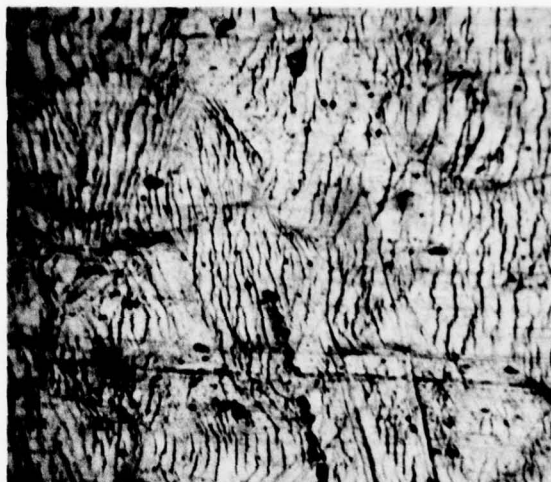
Fig. 20



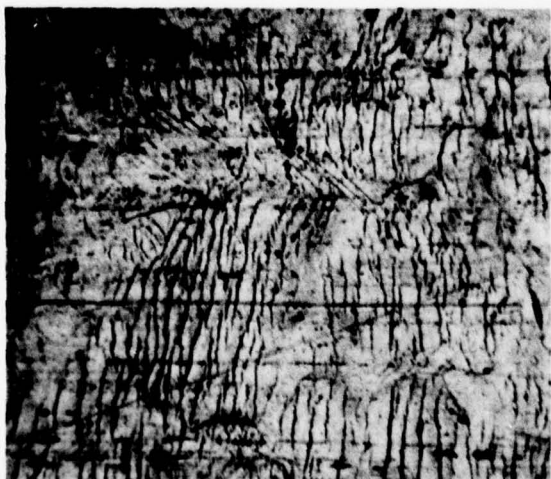
Figure 21. SEM photograph of an edge of a Boeing Baseline oxide layer on 2024 clad Al. From the photograph, the oxide thickness is seen to be 3500 Å.



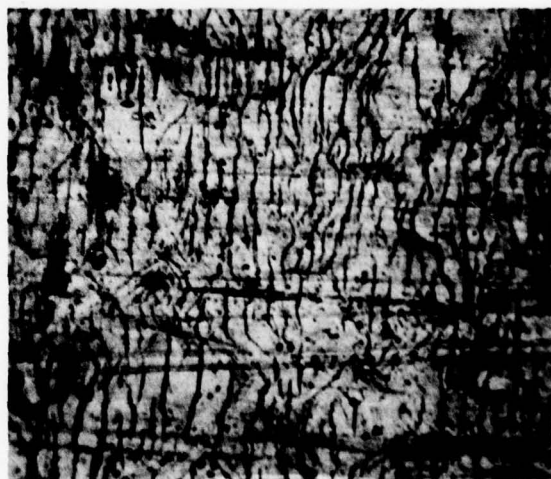
(a) 4V



(b) BASELINE

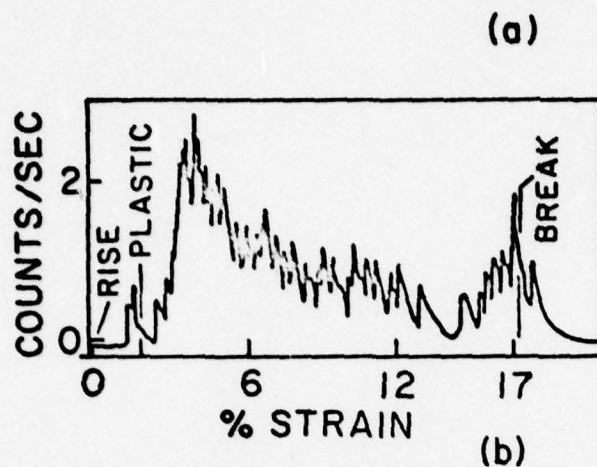


(c) "WITHOUT ETCH"



(d) 20 V

Figure 22 . Photomicrographs of the four Boeing oxides on 2024 clad Al after being strained to the rupture point. Each photograph is 200X.



BOEING
BASELINE H_3PO_4
ON 2024 Al CLAD
TOTAL NUMBER
OF COUNTS 236

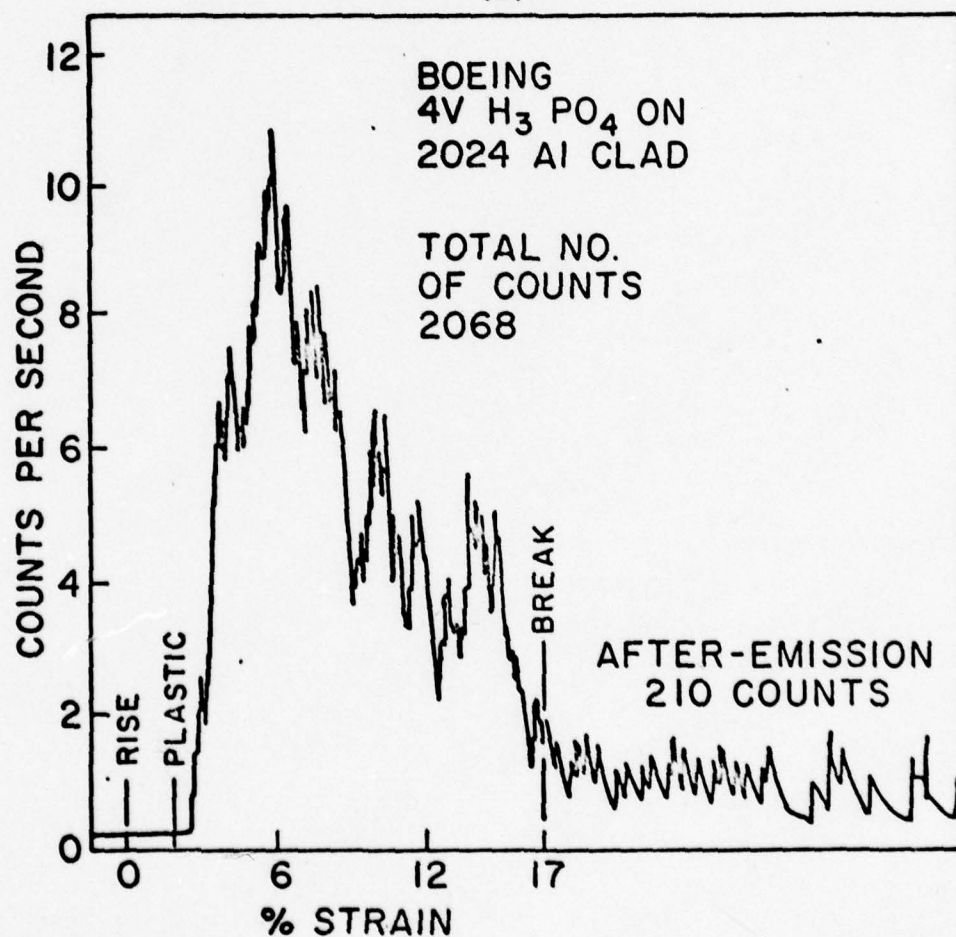


Fig. 23

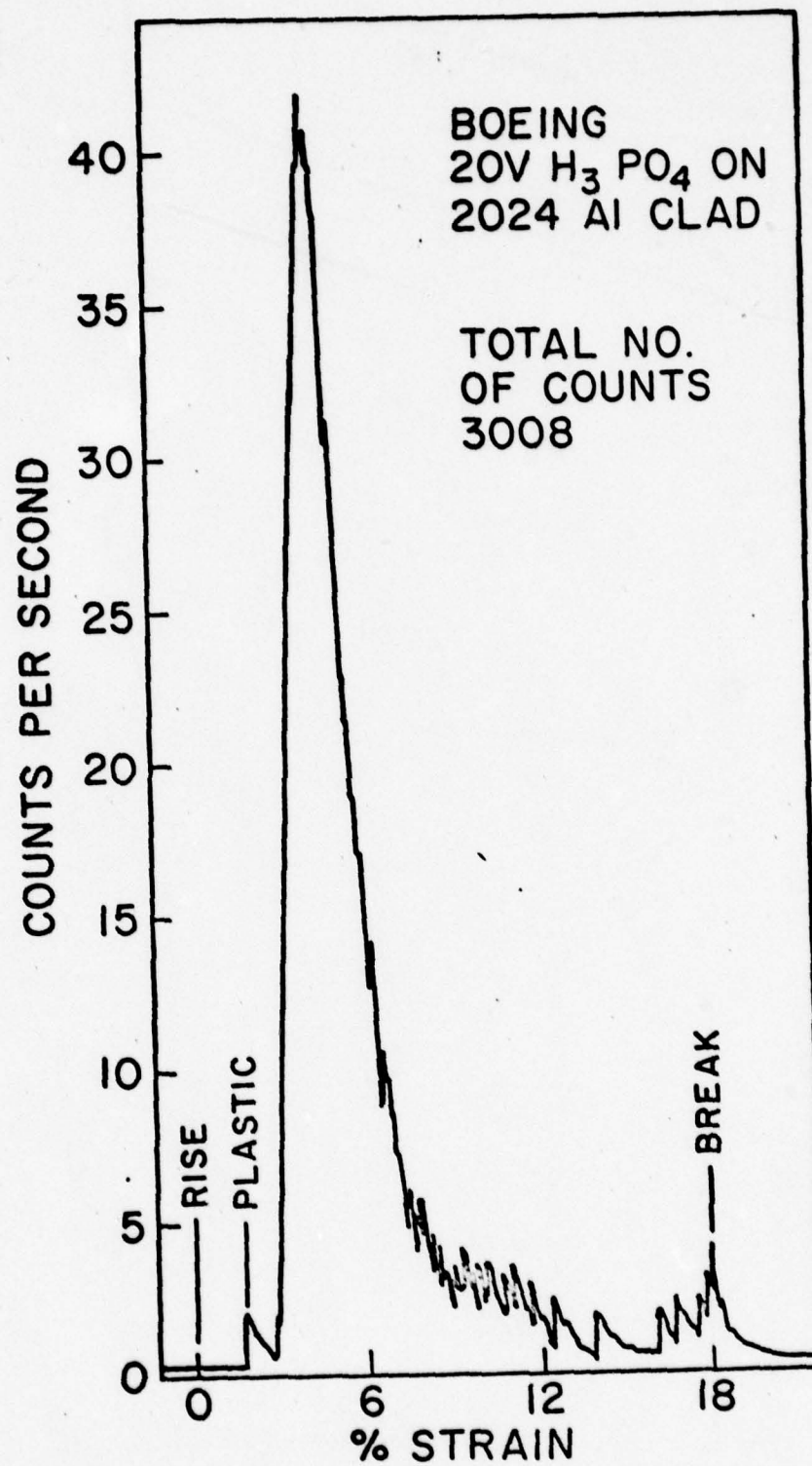


Fig. 24

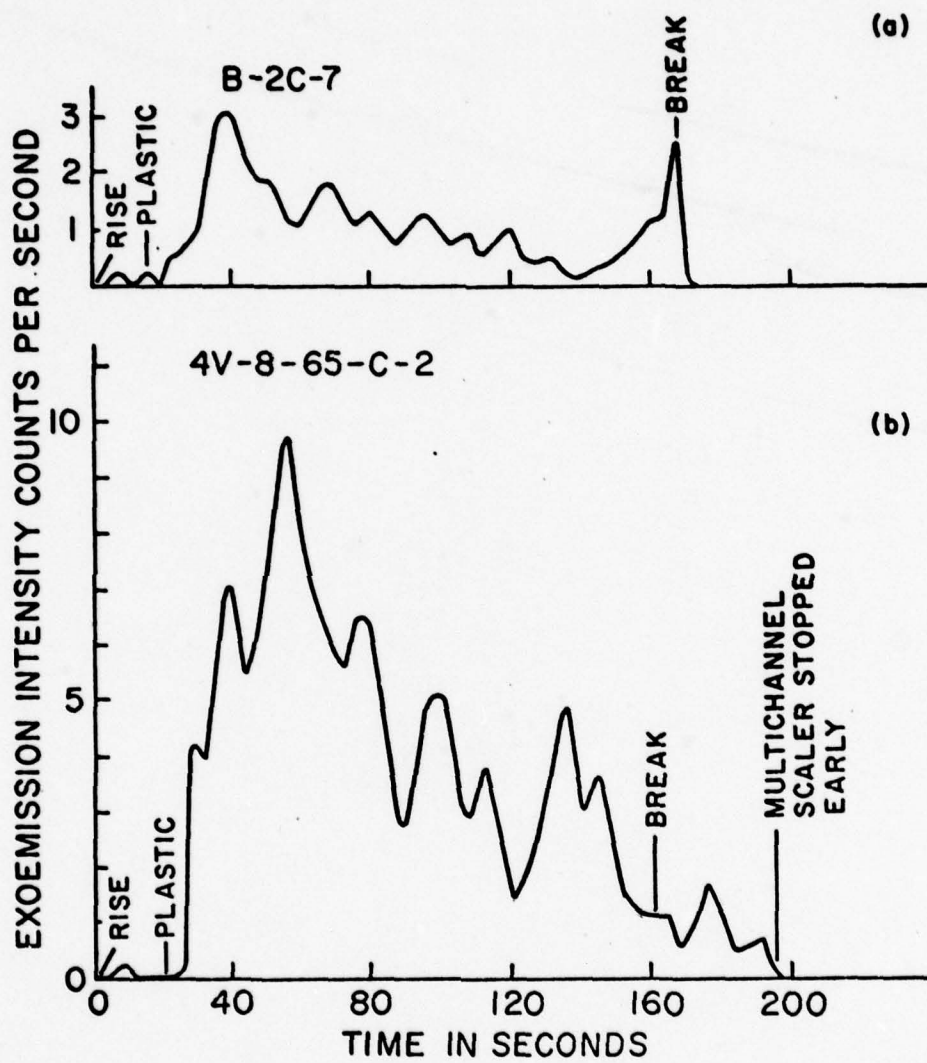
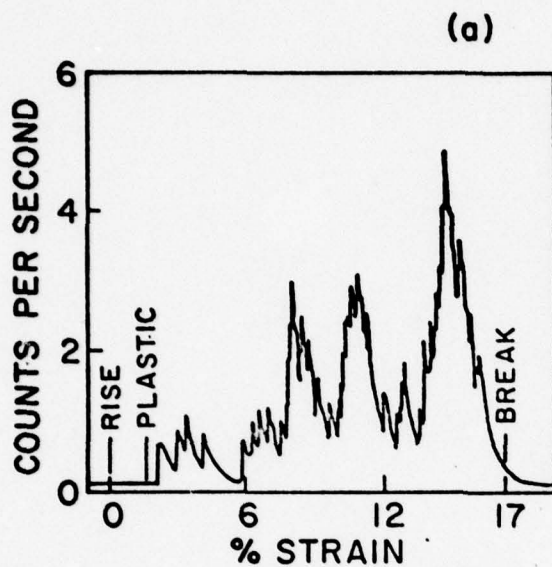
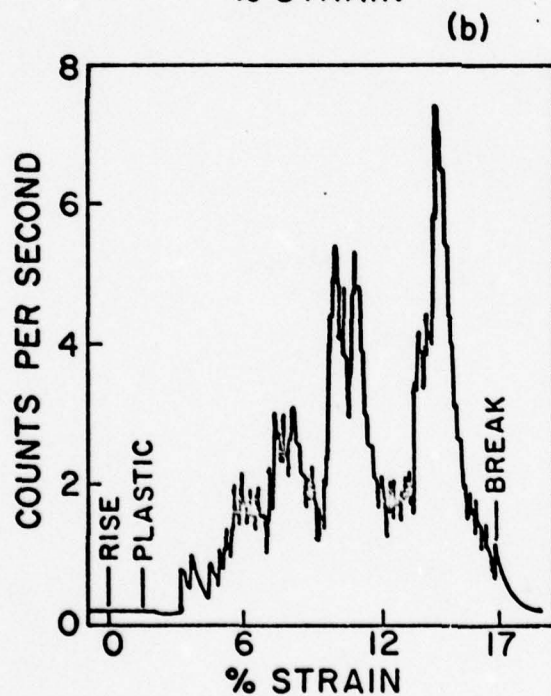


Fig. 25



BOEING
BASELINE H_3PO_4
ON 2024 Al BARE

TOTAL NUMBER
OF COUNTS
262



BOEING
WITHOUT ETCH
BASELINE H_3PO_4
ON 2024 Al BARE

TOTAL NUMBER
OF COUNTS
466

Fig. 26

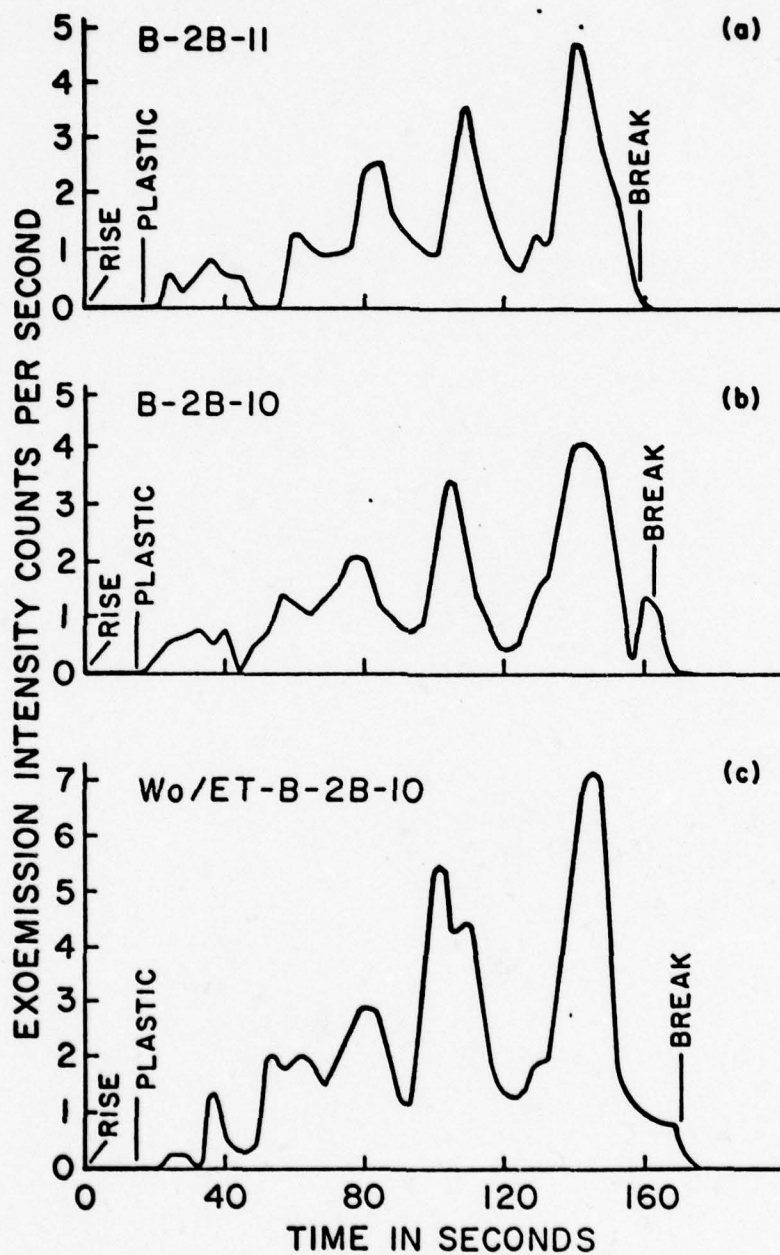


Fig. 27

Auger Electron Spectra 2024 Bare Al Sample

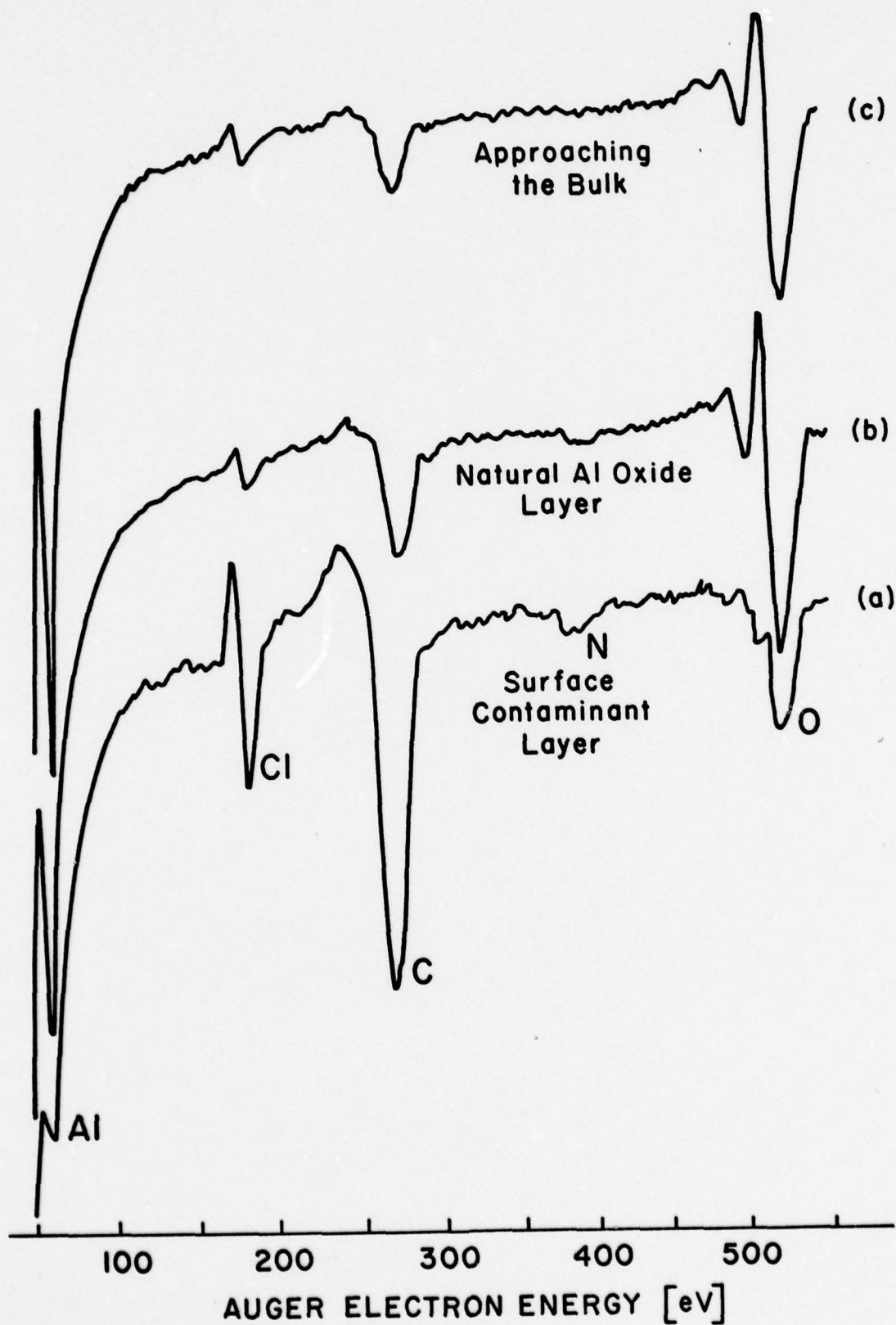


Fig. 28

Auger Peak Heights vs Depth
2024 Al Sample, Natural Oxide Layer

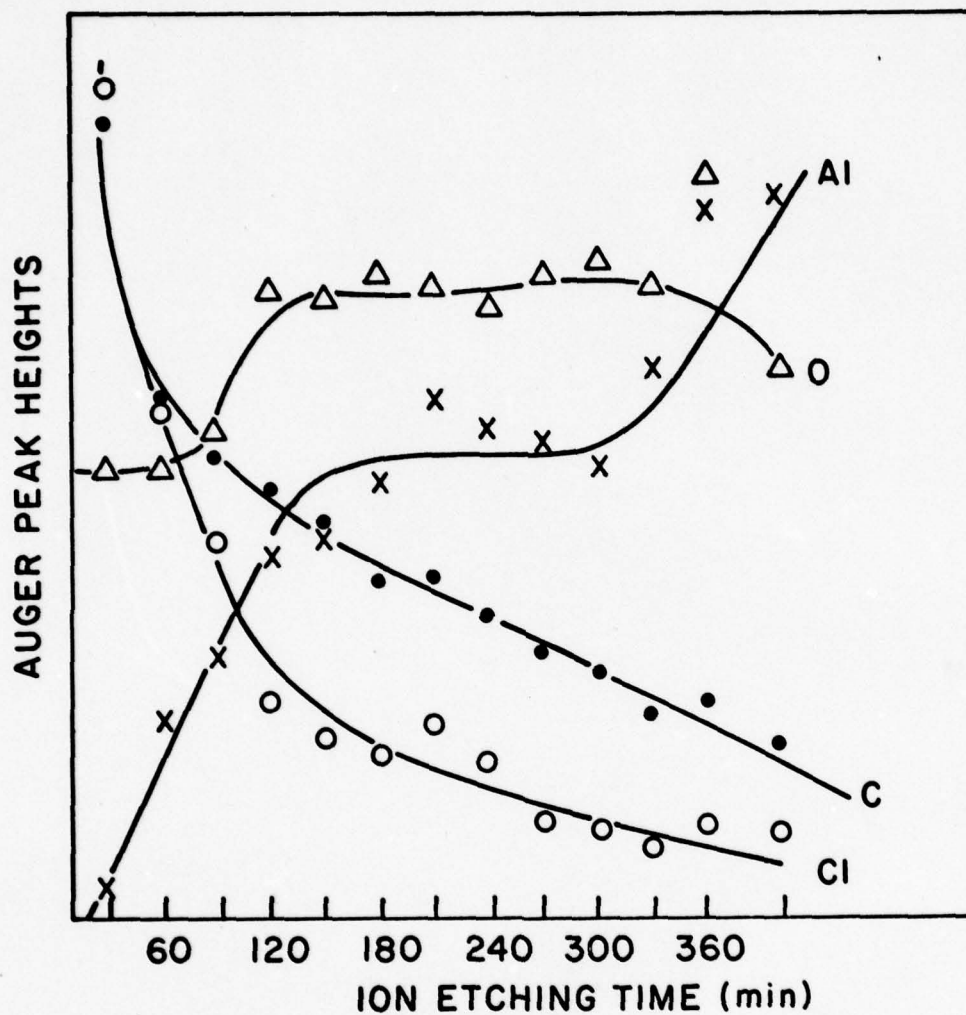


Fig. 29

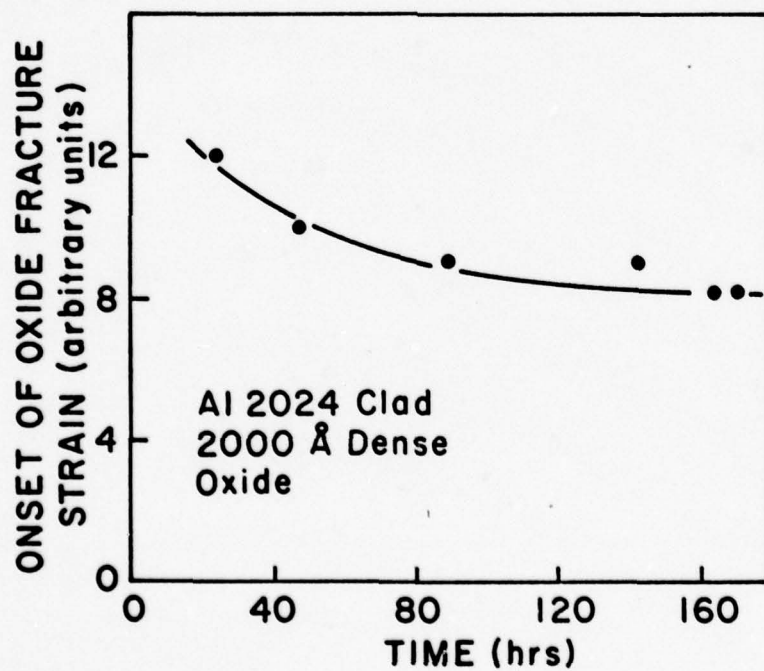
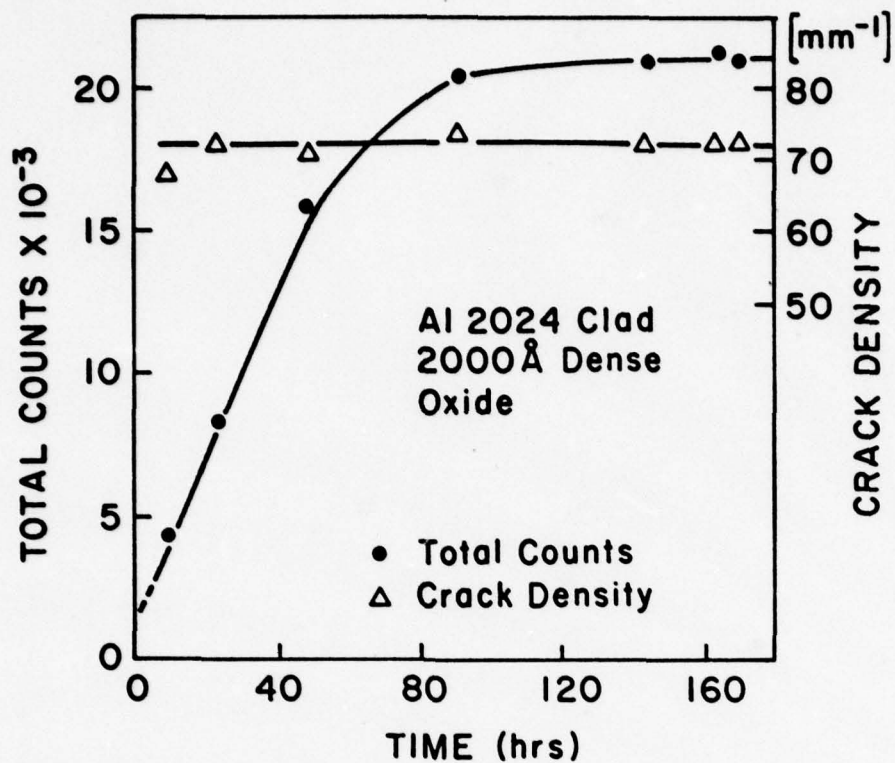


Fig. 30

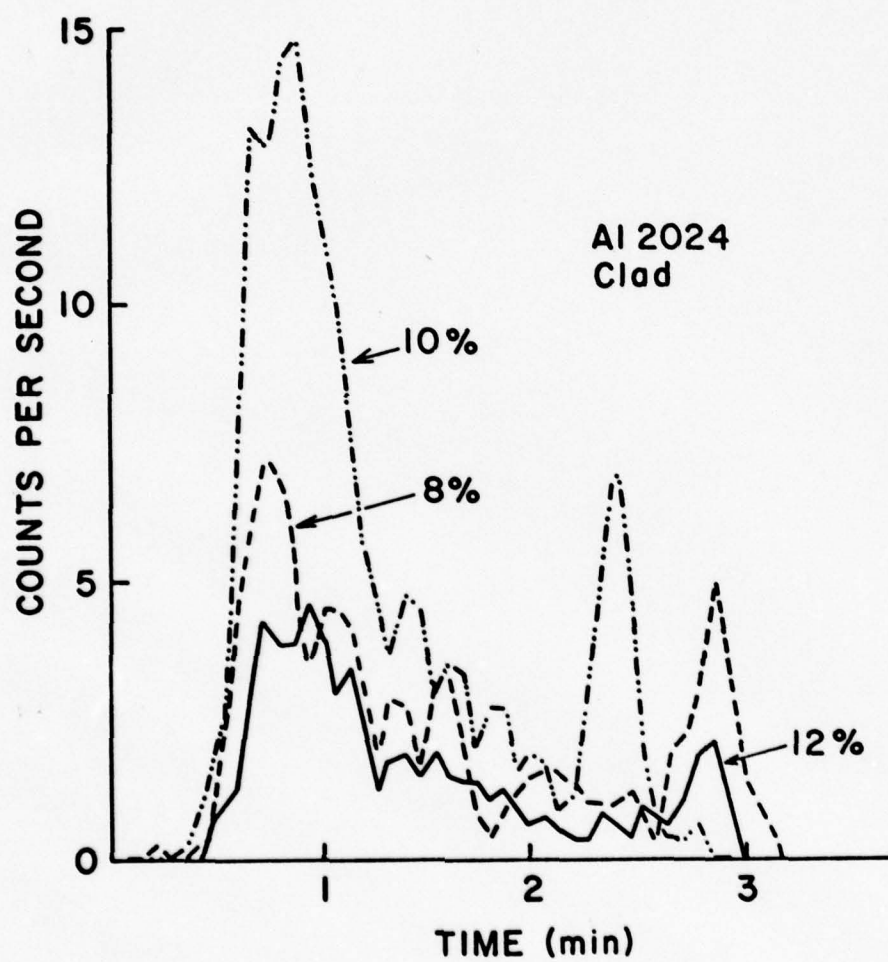


Fig. 31

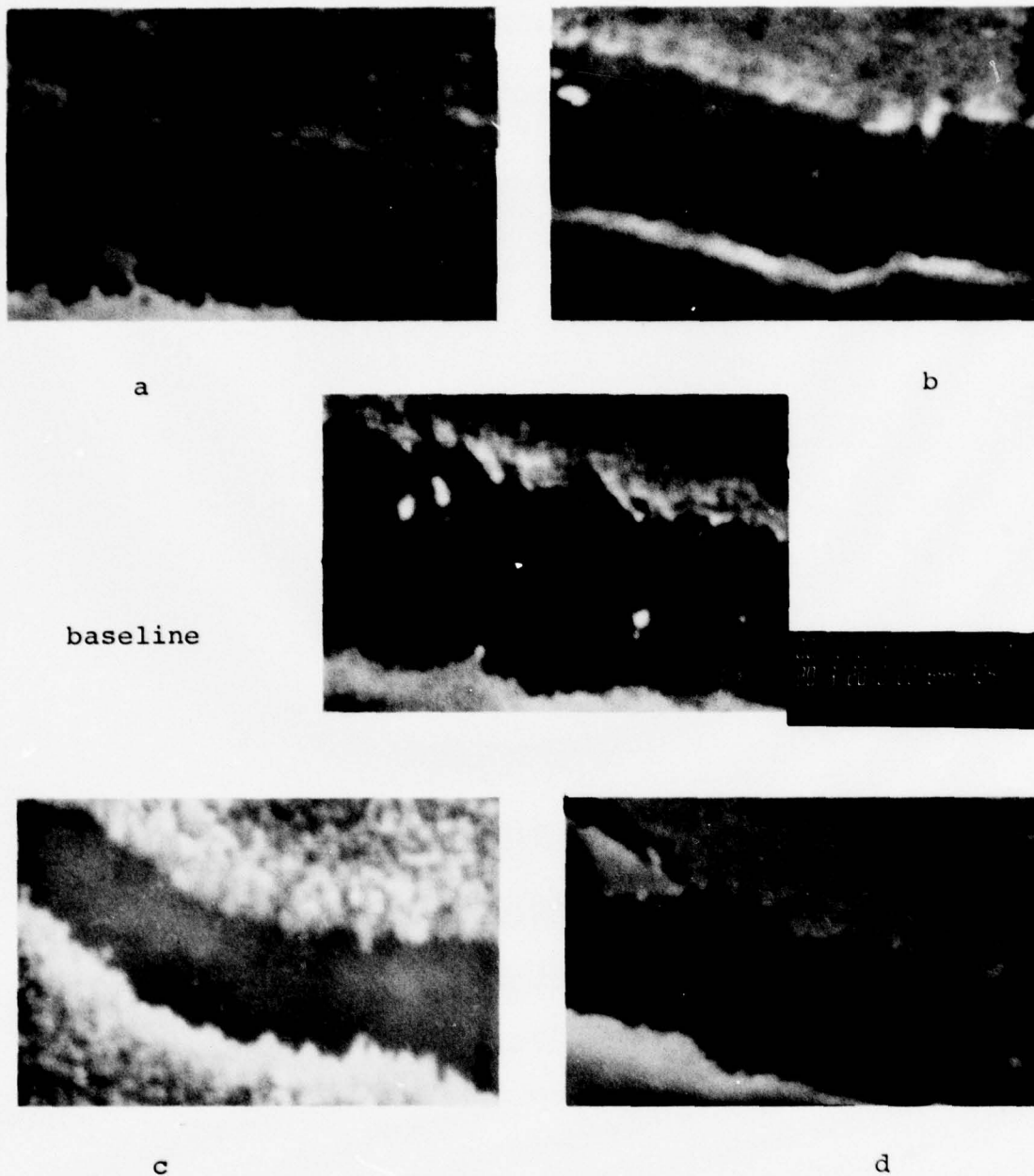


Figure 32 SEM photographs of ruptured oxide on aluminum-clad Al 2024.

Center: Boeing baseline (anodized at 10V, 74 deg. F in 10 wt.% orthophosphoric acid)

a: potential increased to 20V

b: potential decreased to 4V

c: temperature increased to 85 deg.F

d: temperature decreased to 65 deg.F

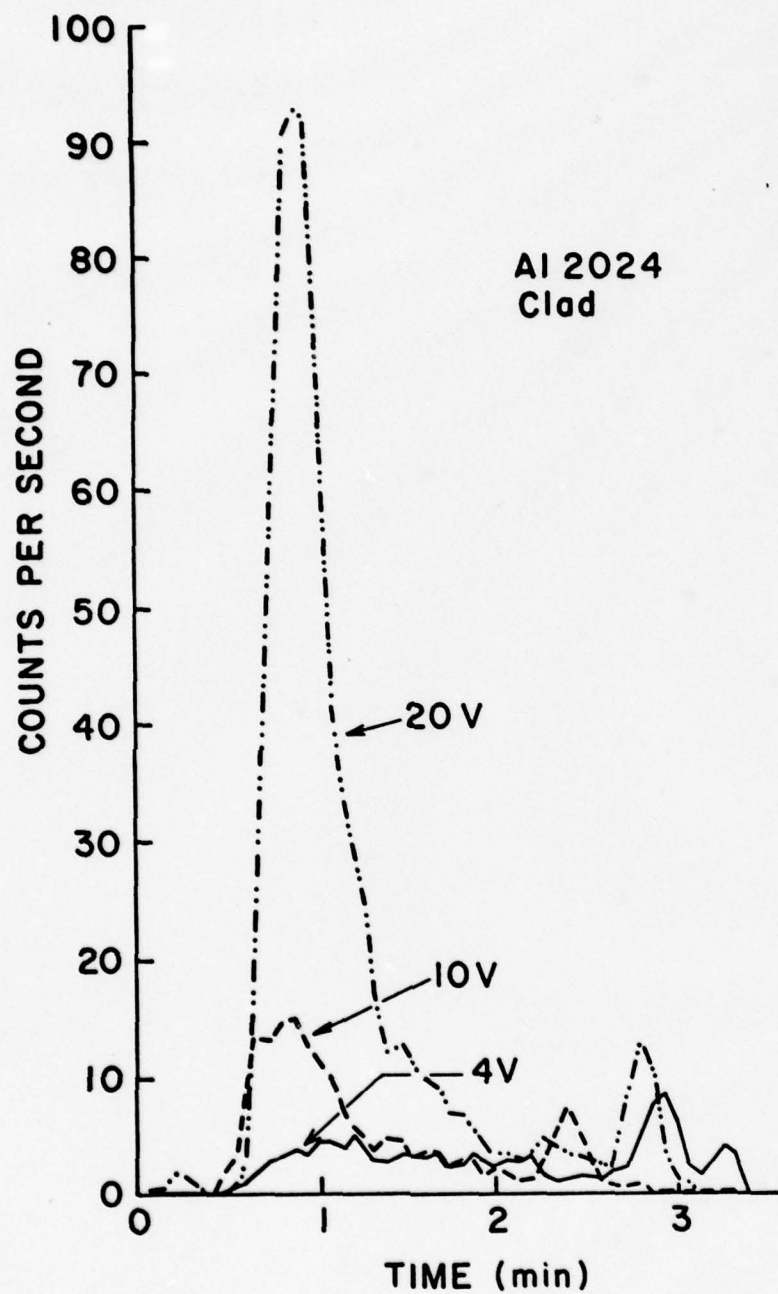


Fig. 33

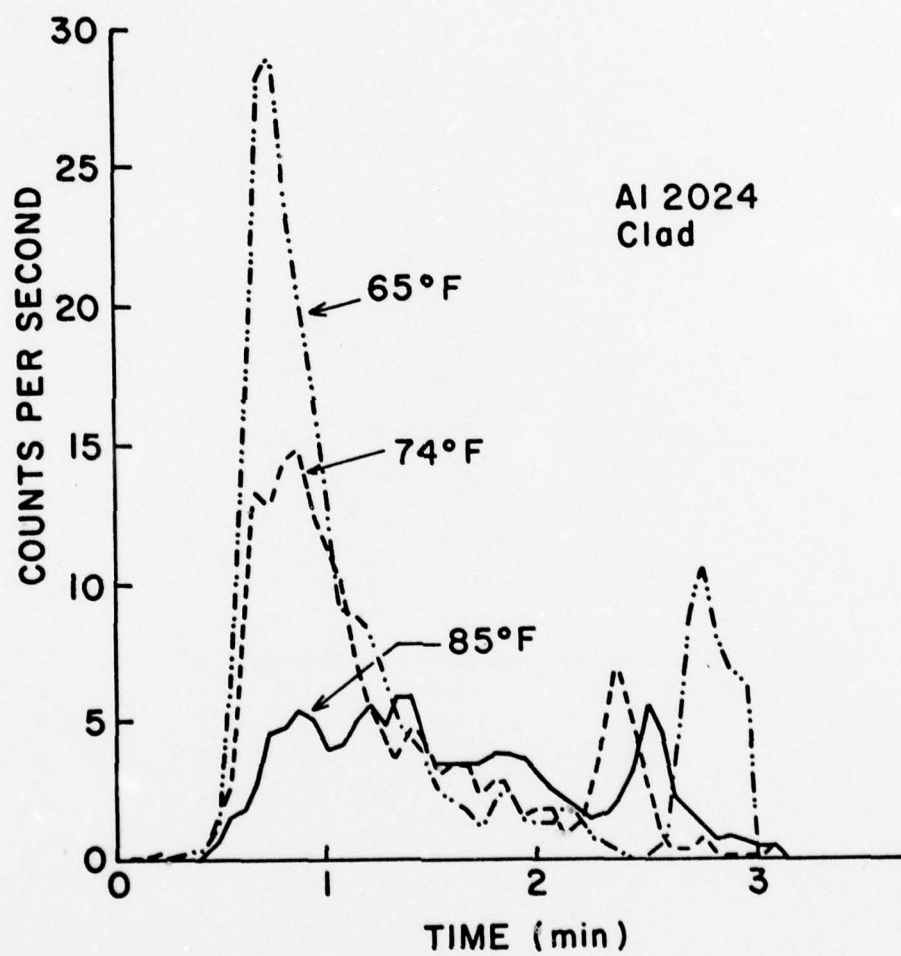


Fig. 34

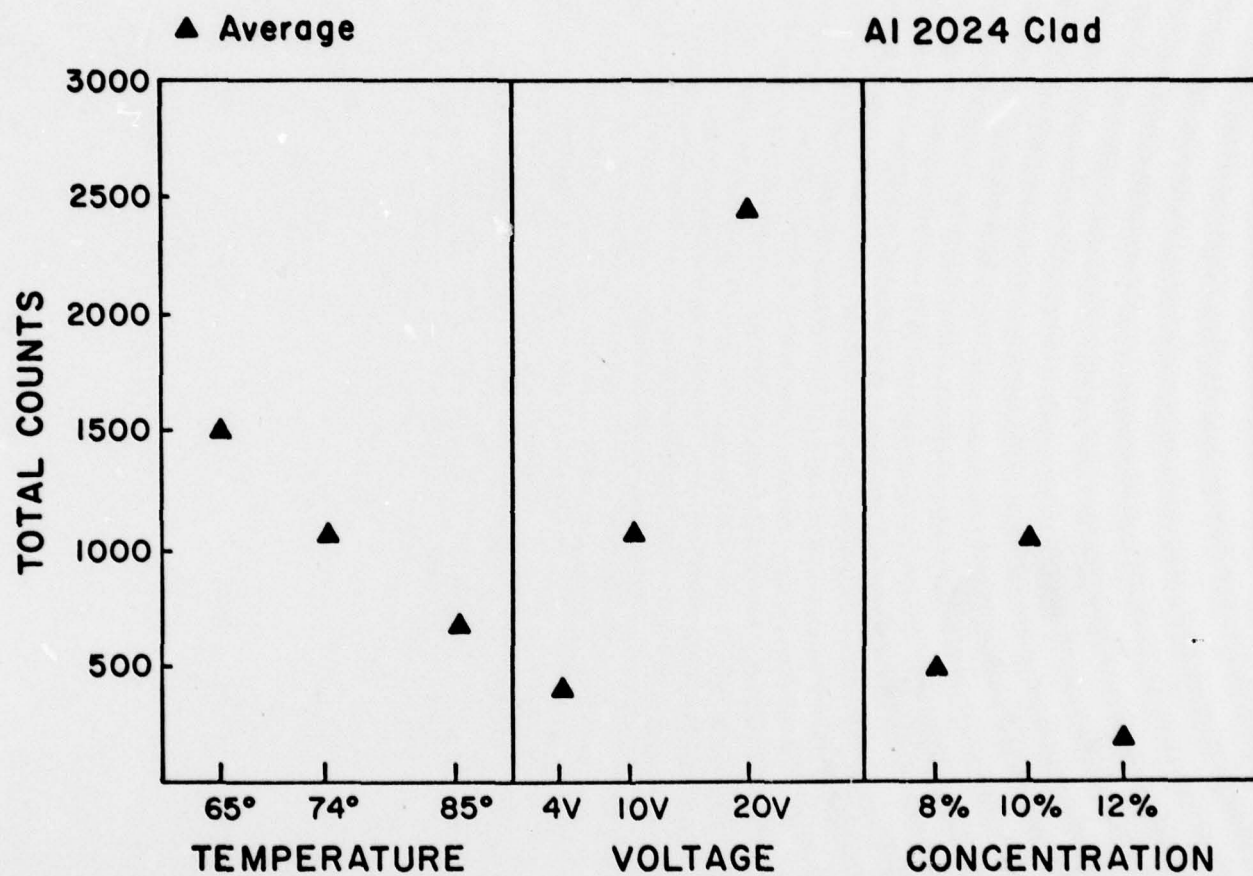


Fig. 35

Quadrupole Mass Separating
Al 2024 Clad,
Porous Oxide, 3,500Å

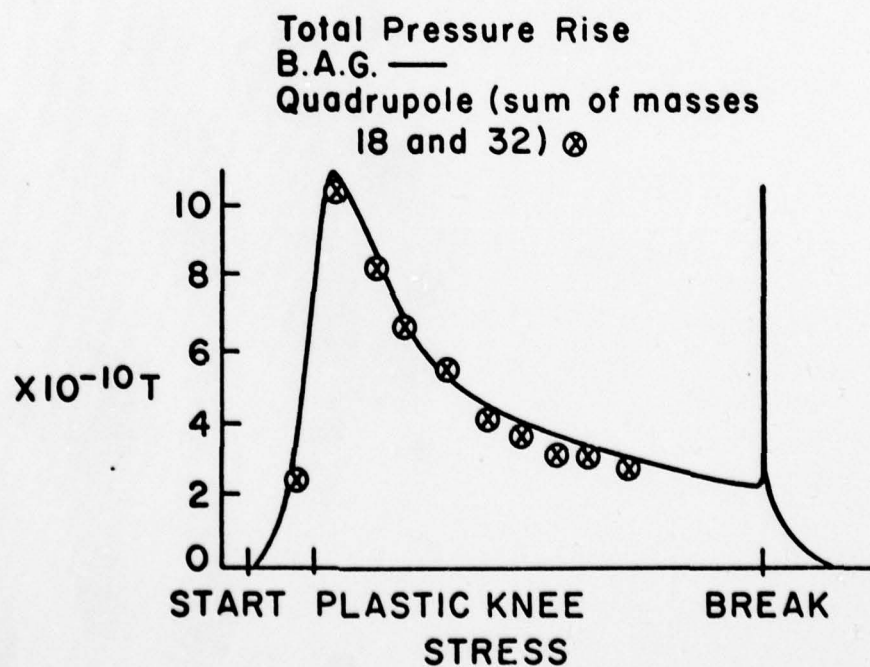
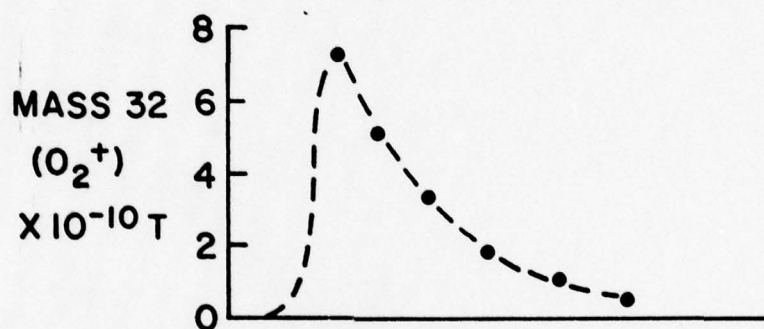
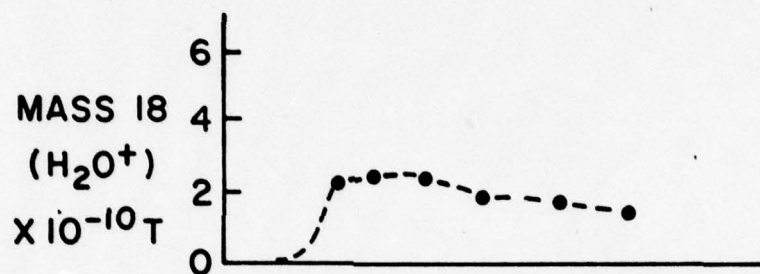


Fig. 36

Total Emission (Neutral and Electron) vs Strain

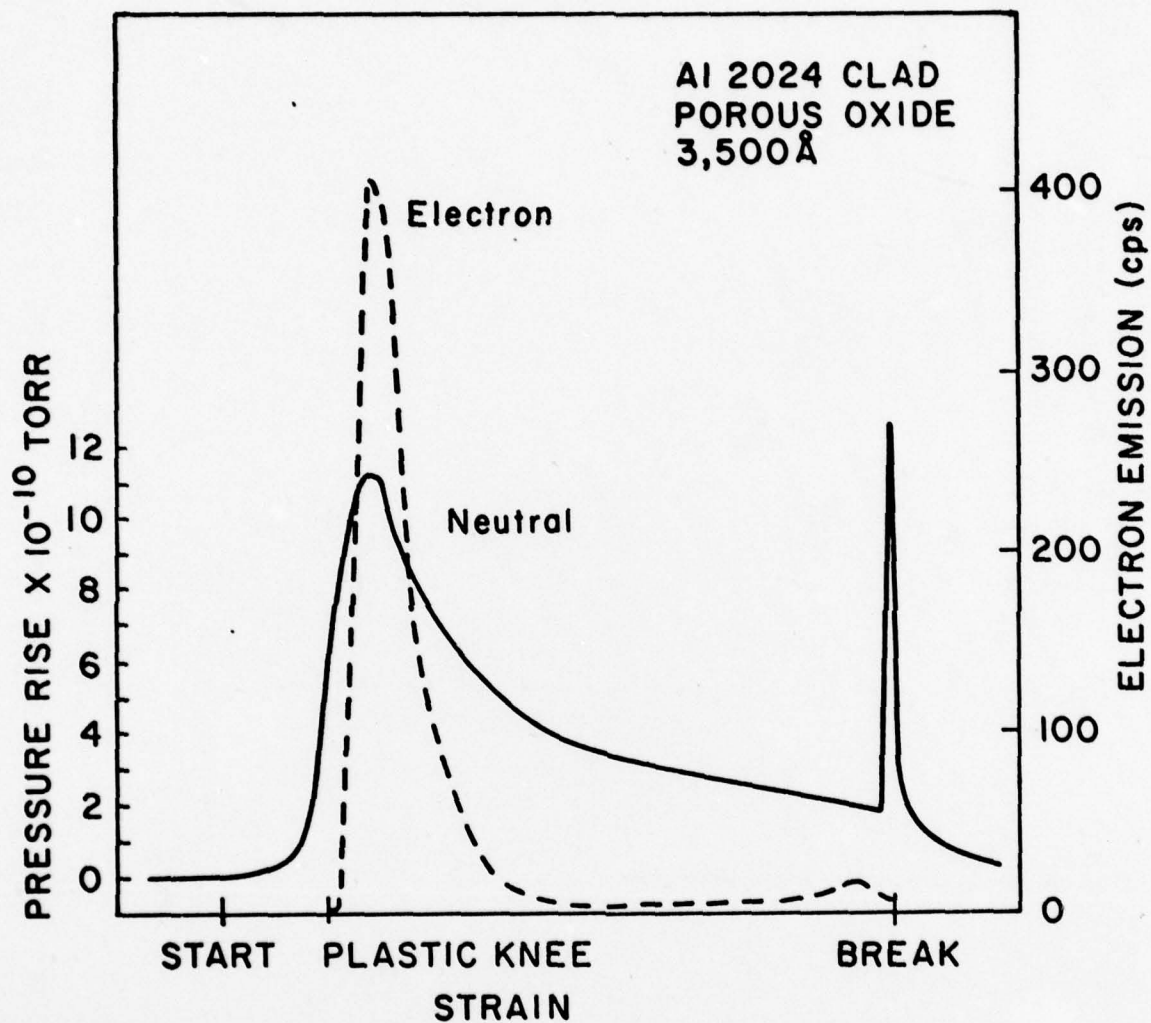


Fig. 37

Total Emission (Neutral and Electron) vs Strain

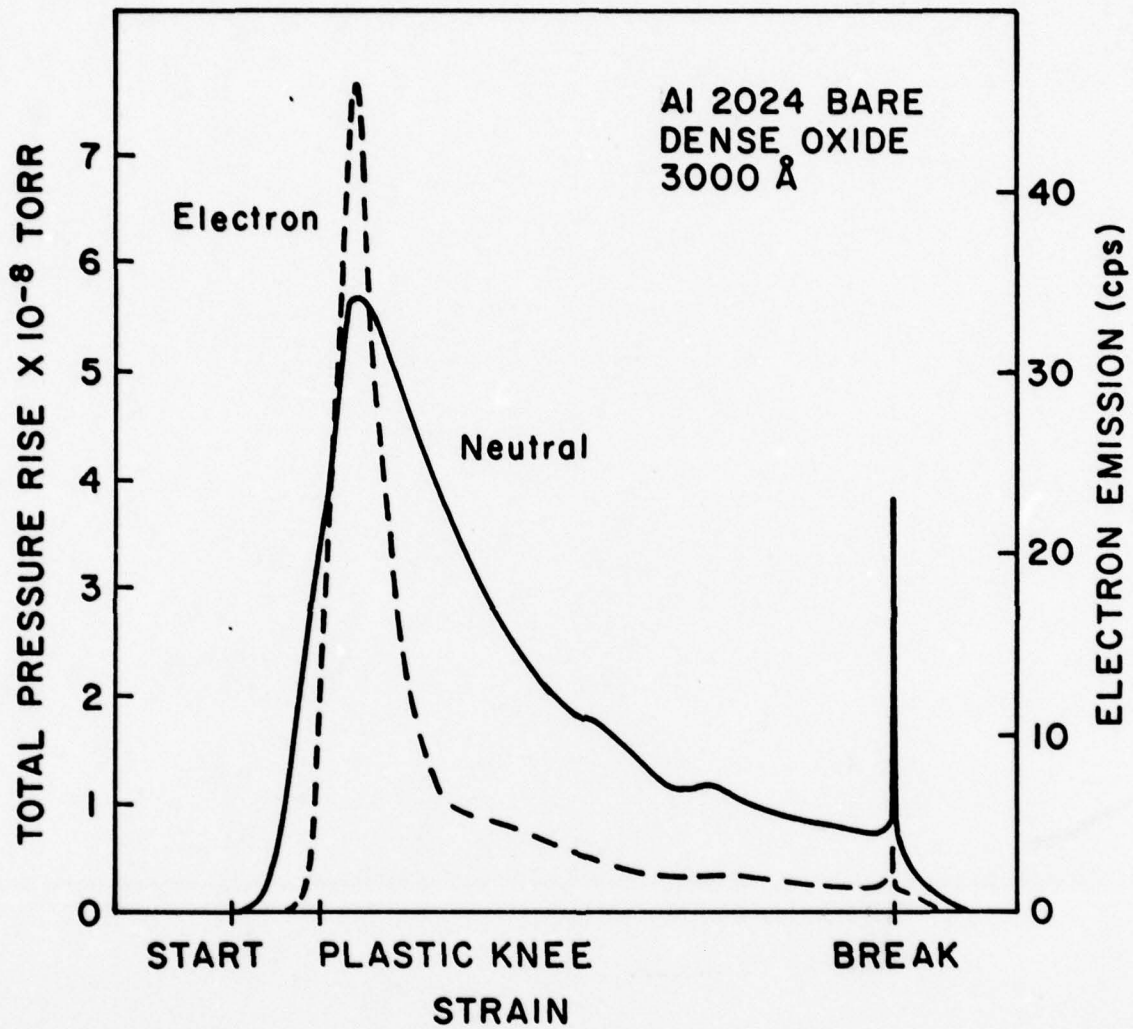


Fig. 38

Measurement of tribo-emission from oxide-covered metals

J. Phys. E, Scientific Instruments,
Vol. 10, 1977

ATTACHMENT A

Ben-Zion Rosenblum[‡], J P Carricot[†], P Brünlich[†] and L Himmel[‡]

[†] Bendix Research Laboratories, Bendix Center, Southfield, Michigan 48076, USA

[‡] College of Engineering, Wayne State University, Detroit, Michigan 48202, USA

Received 19 October 1976, in final form 18 April 1977

Abstract An apparatus is described for the investigation of chemically stimulated, photostimulated and tribostimulated exoelectron emission. Emphasis was placed on tribostimulated emission from uniaxially deformed oxide-covered metals (aluminium, titanium and nickel). Experiments were performed in either ultra-high vacuum or a controlled atmosphere using single-particle counting techniques. The emission of positive and negative ions as well as of photons during the propagation of fracture cracks in the oxide is reported for the first time.

1 Introduction

An apparatus is described which is used to study a wide variety of exoelectron emission phenomena such as chemically stimulated, photostimulated and tribostimulated emission (Grunberg 1958, Brotzen 1967, Kelly and Himmel 1976).

Chemically stimulated emission refers to spontaneous emission arising when chemically reactive gases interact with initially clean metal surfaces (Bohun *et al* 1965, Delchar 1967, Brus and Comas 1971, McCarroll 1969) or with fresh metal surfaces created when the oxide-covered metal is mechanically abraded or deformed (Gesell *et al* 1970). Abrasion or plastic deformation of metals may also temporarily enhance photoemission (Gieroszynski and Sujak 1965, Sujak *et al* 1965, Sujak and Gieroszynski 1970). Tribostimulated emission is detectable in darkness under high-vacuum conditions only during abrasion or deformation of the oxide-covered metal (Kelly and Himmel 1976, Brotzen 1967, Gieroszynski and Sujak 1965, Sujak *et al* 1965, Sujak and Gieroszynski 1970, Arnott and Ramsey 1971, Linke 1970, Rosenblum 1976). This emission arises spontaneously without external stimulation as a result of the rupture of the superficial oxide film.

The equipment described here was developed for investiga-

tion of all three types of emission phenomena with emphasis on tribostimulated emission, of which little is known, and, because of potential applications in non-destructive testing, in studies of brittle fracture of ceramics, and in several fields of tribology. The only metals so far investigated are oxide-covered aluminium, zinc, nickel and titanium, all of which emit charged particles (Gieroszynski and Sujak 1965, Sujak *et al* 1965, Sujak and Gieroszynski 1970, Arnott and Ramsey 1971, Linke 1970, Rosenblum 1976) except zinc (Linke 1970). Qualitatively, the same emission behaviour is observed when these oxide-covered metals are mechanically abraded (Kortov *et al* 1970, Kortov and Myasnikov 1972) or plastically deformed in tension (Gieroszynski and Sujak 1965, Sujak *et al* 1965, Sujak and Gieroszynski 1970, Arnott and Ramsey 1971, Rosenblum 1976). The emission current is discontinuous and very weak (10^{-13} A m⁻²). In tension, the emission is strain dependent. For a constant strain rate it increases to a maximum, followed by a monotonic decrease with increasing strain and ceases abruptly when the deformation stops. This emission depends on the strain rate as well as the oxide thickness and is proportional to the rate at which cracks are nucleated.

Two distinctly different models have been suggested to account for tribostimulated emission from oxide-covered metals. The first (Gieroszynski and Sujak 1965, Sujak *et al* 1965, Sujak and Gieroszynski 1970) postulates that cracking of the oxide film during plastic deformation of the metal substrate is accompanied by charge separation across opposing crack surfaces, resulting in the creation of strong local fields within the cracks. These transverse fields are believed to be sufficiently intense to give rise to field emission of electrons from the crack walls. This model is known as the electrified fissure model. The other model (Arnott and Ramsey 1971) is based on the proposition that the release of stored elastic strain energy in the oxide film at the tips of rapidly propagating cracks in the brittle oxide is responsible for the emission which is thought to originate in the oxide. However, no suggestions are offered as to the mechanism for transfer of the available strain energy to electrons in the oxide to induce their escape.

In an attempt to determine the applicable model, we compared the emission behaviour of dense, adherent Al₂O₃ films on aluminium with that of dense NiO films or nickel under identical conditions. We also studied titanium and its alloys because of their importance as aerospace material and because the emission characteristics of oxide-covered titanium were unknown. All previous investigators have assumed that the tribo-emitted particles are electrons (Gieroszynski and Sujak 1965, Sujak *et al* 1965, Sujak and Gieroszynski 1970, Arnott and Ramsey 1971, Linke 1970, Kortov *et al* 1970, Kortov and Myasnikov 1972). However, they were unable to distinguish between electrons and negatively charged ions. Furthermore, there is abundant evidence that the rupture or cleavage of dielectric crystals such as alkali halides often induces photon emission – a phenomenon known as triboluminescence (Kelly and Himmel 1976, Brotzen 1967, Rosenblum 1976, Bohun 1970). We therefore developed procedures for detection and measurement of the emission yields of ions, photons and electrons.

The nature of tribostimulated emission must be investigated under conditions where the emitting surface is well defined and that prevent unrelated emission phenomena which can increase the background count rate. Also, it is important that a complete characterization (particle identification and energy spectrum) of the emission products be implemented.

The apparatus and experimental procedures were designed for studies of tribostimulated emission during uniaxial tensile deformation of high-purity metals (e.g. aluminium, nickel and titanium) covered with oxide films of various thicknesses and

[§] Also affiliated with the College of Engineering, Wayne State University, Detroit, Michigan 48202, USA.

^{||} Present address: Department of Physics, Washington State University, Pullman, Washington 99164, USA.

structures. Experiments were conducted in total darkness under ultrahigh-vacuum conditions for precise control of the environment. Deformation of the samples was carried out at constant strain rates during which loads and displacements were recorded autographically. Tribostimulated emission of charged particles and/or photons was detected with single-event detectors. Discrimination between negatively charged particles (electrons and ions) was achieved using a magnetic technique in conjunction with the inherent discrimination characteristics of the charged particle detector.

A specially designed high-resolution spectrometer permitted surface characterization by employing Auger electron spectroscopy (AES). Energy distribution measurements of tribo-emitted charged particles were carried out with the aid of a high-sensitivity retarding potential analyser. A gas-dosing system for chemically stimulated emission, an ion gun for *in situ* cleaning of the specimens and internal quartz and LiF optics (including a uv monochromator) for photostimulated emission were also incorporated into the system. However, since we were primarily concerned with tribostimulated phenomena, these latter items were not used in the present work.

After deformation, the specimens were viewed with the aid of a scanning electron microscope which facilitated the study of the mechanical behaviour of oxide films on strained metal substrates and their correlation with tribostimulated emission.

In addition to the apparatus, experimental techniques are described and results presented which demonstrate the capabilities of the system.

2 Apparatus

The apparatus for measurement of tribostimulated emission during uniaxial tensile deformation of high-purity materials consisted of the following principal components: an ultrahigh-vacuum (UHV) system, a uniaxial tensile straining device, a charged particle discrimination detector, an Auger electron spectrometer, a photon emission detector, and an energy analyser for tribostimulated emission. The UHV system was originally part of a LEED system. The composition of the residual gases in the chamber was determined with the aid of a quadrupole mass spectrometer. After bake-out at 250 °C for 24 h, the pressure was typically about 1.33×10^{-9} Pa.

2.1 Uniaxial tensile straining device

The uniaxial tensile straining device is shown in figure 1. Two

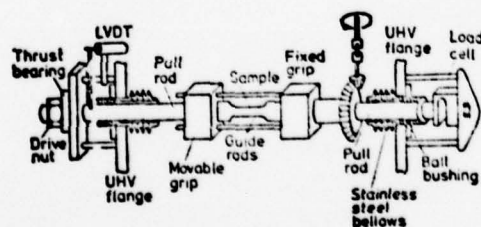


Figure 1 The tensile straining device.

pull rods were supported in a horizontal position by ball bushings mounted outside the chamber. The pull rods entered the vacuum chamber through diametrically opposed flanges. The specimen was mounted and pinned in split grips having serrated faces. The grips could be externally rotated 360° about the tensile axis to facilitate installation of the specimen. The specimens were normally kept at ground potential. How-

ever, with alumina inserts in the grips, they could be held at any desired potential.

Linear motion of the movable pull rod was achieved by rotation of an external drive nut threaded on to the end of the pull rod and forced against a thrust bearing mounted on the pull rod. The speed of rotation of the drive nut, and hence the strain rate, were controlled by a variable-speed DC motor coupled to the drive nut through a reducing gear.

To obtain load-elongation curves for the tensile specimens, the fixed pull rod was rigidly attached to a load cell mounted externally to the flange. Displacement of the movable pull rod with respect to the flange was measured with a linear variable differential transformer (LVDT).

The maximum allowed linear displacement of the stainless steel bellows restricted the linear motion of the movable pull rod to 1.25 cm. With a specimen gauge length of approximately 2.5 cm, the maximum tensile strain was 50%. The displacement sensitivity of the LVDT was about 0.025 mm, thereby allowing measurements of tensile strains to within approximately 0.1%. The specimen gauge dimensions (0.5 cm wide, 0.05 cm thick) and 227 kg maximum capacity for the load cell permitted maximum tensile stresses of the order of 10^9 N m⁻² with an accuracy of 0.45 kg. LP
AP

The straining system was capable of uniaxially deforming a specimen in tension at controlled strain rates between 0.5 and 10^{-4} s⁻¹. During this time, the load-elongation curve was recorded and tribostimulated emission was detected without significant mechanical or electrical noise.

2.2 Particle detection and discrimination schemes

Since tribostimulated emission from oxide-covered metal surfaces is a very weak phenomenon with fluxes of 10^1 – 10^6 particles s⁻¹ m⁻², it was necessary to use single-event charged particle and photon detectors. A channel electron multiplier (CEM) with an input cone was used because of restricted space (Schmidt 1969). Also, the CEM has different detection efficiencies for electrons and ions which is useful for charged particle discrimination. This detector was shielded to minimize detection of charged particles from the ion pump as well as to control the electrostatic field which accelerated the charged particles emitted from the specimen into the cone. The shield ensured that this field was due to the CEM's biasing potential relative to the specimen and not to the potential applied across the CEM. The CEM was attached to a precision x-y-z manipulator which allowed its precise positioning with respect to the centre of the specimen (figure 2). Shielded wire was used

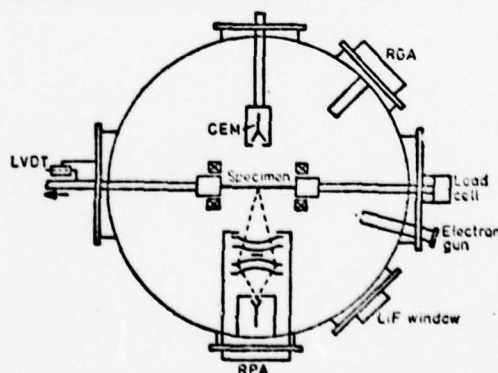


Figure 2 Arrangement for surface characterization and charged particle detection and discrimination. RGA, retarding grid analyser.

inside the vacuum chamber to prevent stray electrostatic fields from influencing the charged particle trajectories. The electrostatic field developed between the emitting surface and the cone focused and accelerated the emitted charged particles into the CEM.

The energy-dependent detection efficiency of the CEM for various charged species (Adams and Manley 1966) was important for our work. For example, with a cone bias of +75 V with respect to the specimen, the detection efficiency for electrons was about 0.25 while that for negative ions was much lower. On the other hand, a cone bias of +1000 V results in a near-unity detection efficiency for negative ions and about 0.25 for electrons (Frank *et al* 1969, Crandall *et al* 1975, Borrous *et al* 1967). For the detection of positive ions with unity efficiency, the bias should be -1000 V.

For absolute discrimination between electrons and negative ions, a low biasing potential and a suitable transverse magnetic field were necessary (figure 3, inset). This magnetic particle discriminator was calibrated with the aid of low-energy photoelectrons produced by irradiation of an Al specimen with focused monochromatic UV radiation of 220.0 nm. The Al was irradiated on the side opposite to the shielded CEM to prevent detection of scattered photons. With no magnetic field, photoelectrons were drawn into the cone of the CEM with a bias field of about 40 kV m⁻¹. For a transverse magnetic field of approximately 1.4 mT, the CEM signal was reduced to the background level shown in figure 3. The relative yields of

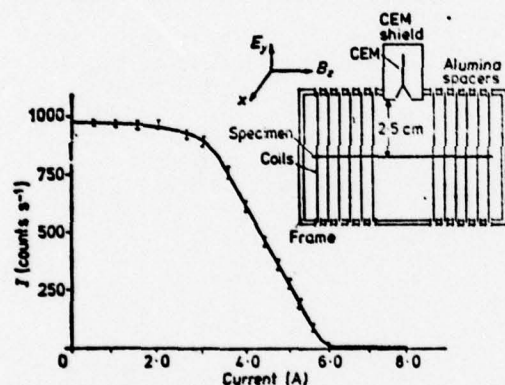


Figure 3 Magnetic discrimination scheme. Photoelectric current I reaching the CEM is plotted as a function of DC current passed through the coils. Electrostatic field strength: 40 kV m⁻¹. Inset: positioning of the specimen with respect to the coils and the shielded CEM.

electrons and negatively charged ions were measured in each run by switching back and forth between the electron and negative ion detection modes.

For measurement of photons, a miniature single-photon counter tube (Bendix BX754) was used. The retarding potential analyser (see §2.3) and coils were removed and the photon tube was installed facing the front surface of the specimen (see figure 2).

Since the S-20 photocathode could not withstand baking temperatures above 80–100 °C, a special stainless steel tube having a quartz window was devised which permitted insertion of the photon tube after baking in close proximity (1.5 mm) to the specimen's surface. Photon emission was indeed observed during deformation, but the photon flux was too low to determine its spectral distribution.

2.3 Auger electron spectrometer

An analyser was needed also for Auger and photoelectron spectrometry. A somewhat modified version of Staib's retarding potential analyser (RPA) (Staib 1972) was built. It consisted of two sets of two hemispherical concentric grids G_1 and G_2 (retarding section) and G_3 and G_4 (focusing section). These two parts were separated by a field-free region. The charged particle source was located at the centre of curvature of the retarding section while an aperture D was located at the centre of curvature of the focusing section, behind which the charged particle detector was mounted.

Type 304 stainless steel was used whenever possible. The four hemispherical grids were made from etched 304 stainless steel mesh 0.025 mm thick and having 100 lines in⁻¹ with mesh openings of 0.15 mm. The grids were shaped by hot pressing in an inert atmosphere between specially designed graphite dies. After forming, the retarding grid G_2 was coated with a thin film of gold by vacuum deposition. This step was necessary for precise determination of the grid's work function. The radii of curvature were 33.5 mm for G_1 and G_4 and 42.5 mm for G_2 and G_3 . The radius of curvature of each grid was measured with the aid of a calibrated shadowgraph and found to be within 0.1 mm of the specified value.

Again, a shielded CEM was employed as the charged particle detector. The entrance aperture was 1.6 mm in diameter. A stop S was used to prevent detection of photons generated as a by-product during Auger electron stimulation with high-energy electrons. Two sets of fringing rings were added to minimize the distortion of the equipotential surfaces of the electrostatic field between G_1 and G_2 (Goto and Ishikawa 1972). The grids section was shielded with Mumetal foil and the entire spectrometer was shielded with a thin 304 stainless steel shroud.

The resolution of the RPA, inferred from its ability to reveal small concentrations of impurities, was approximately 1%.

The primary-electron beam (0.5 mm diameter, 3 keV, 80 μ A) was aimed at the point of intersection of the optical axis of the spectrometer with the specimen's surface (15° angle of incidence). AES modulation techniques were employed and the resulting signal was electronically processed by a lock-in amplifier (Keithley 840). Auger electrons were modulated in the field-free region at 915 Hz peak-to-peak voltage range between 3.5 and 10 V.

2.4 Energy analyser for tribostimulated particles

Modulation techniques could not be easily implemented to measure the energy distribution of tribostimulated particles because of the non-steady-state nature of the measured phenomena: the emission occurred intermittently in bursts which were time or strain dependent. A modulation technique involving repeated energy distribution measurements and digital counting data storage in a multichannel analyser was not feasible since the sweep rate required for an adequate signal-to-noise ratio was too slow. Also, the RPA used in AES was not suitable for energy distribution measurements of tribostimulated charged particles because this emission originated from the entire gauge length (2.5 cm) of the specimen. In addition, the RPA's low solid angle of detection and losses due to four grids limited its use to AES and photoemission spectroscopy where the emission currents were relatively high. Thus, an electron spectrometer designed specifically for energy distribution measurements of tribostimulated particles had to be developed.

The basic requirements for this device were high sensitivity and a large solid angle of detection. Resolution of fine structure in the energy distribution was not anticipated. Thus, resolution could be sacrificed somewhat for sensitivity. A retarding-field-type analyser having two flat grids was suitable

for this application. The first grid G_1 located 3 mm in front of the sample, was biased positively with respect to the specimen and the second G_2 served as a retarding grid. The grid diameters were 3.2 cm, slightly larger than the gauge of the tensile specimen. They were made from photo-etched pure nickel foil (0.025 mm thick) having 80 lines in^{-1} with square mesh openings of 0.2 mm and 97% transmission and mounted 6 mm apart. A fringing ring was used to minimize distortion of the electrostatic field between the grids (Goto and Ishikawa 1972). A post-monochromator selectively focused the electrons passing through the retarding grid on to the entrance aperture of a CEM (Huchital and Rigden 1972).

Since resolution was of secondary importance, no attempt was made to determine it experimentally, whereas overall performance was determined in the energy range 0–4 eV for tribostimulated electrons from the energy distribution of thermionic electrons emitted from a tungsten filament. From this the resolution was estimated to be at least 0.5 eV.

In measuring the energy distribution of negatively charge tribostimulated particles, the retarding potentials were applied to G_2 in 1 V increments and held constant during a pulse counting period of 10 s. Since this emission is not a steady state phenomenon, the count rates were normalized with respect to the emission peak height.

3 Specimen preparation and measurement techniques

Materials used for the present investigation were high-purity polycrystalline aluminum, nickel and titanium (Materials Research Corp.). After formation into strips 25 mm wide and 0.5 mm thick by six stages of cold-rolling, the strips were degreased and cleaned with non-alkaline solvents but not polished. The metal strips were received on spools in argon-filled polyethylene bags. The lengths of these strips varied from 30 to 150 cm. To avoid contamination, the materials were handled using clean-room techniques.

Tensile specimens were obtained from the strips by carefully machining without forced cooling using a template and a sharp end mill. Small cuts were taken to prevent excessive deformation. After machining, the edges of the tensile specimens were carefully de-burred with 400 grit SiC paper. They were of the conventional flat 'dog-bone' shape with 2.5 cm gauge length and a parallel width of 0.5 cm. The specimens were then degreased in research grade acetone and stored in a desiccator.

To obtain maximum tensile strains, it was necessary to carry out recrystallization anneal treatments on the tensile specimens. The recrystallization anneal was carried out in a Vycor tube furnace. Tests on samples were conducted to determine the anneal conditions. The average Knoop hardnesses of unannealed and annealed test samples were compared and the average recrystallized grain sizes of the latter were determined. Results showed that the aluminium specimens did not require the anneal treatment since they recrystallized at room temperature. The nickel and titanium tensile specimens were annealed in vacuum (encapsulated in a quartz tube pumped to about 6.65×10^{-7} Pa for one hour at 580 and 635°C respectively).

Surface oxidation was carried out according to procedures which produced dense, adherent oxide films with uniform and known thicknesses. Al_2O_3 films were grown by wet anodization (Tajima 1970), TiO_2 by wet anodization (Tibol 1964) and plasma oxidation (Knorr and Leslie 1974), and nickel oxides by thermal oxidation (Graham *et al* 1972).

Prior to strain/emission measurements, the composition of the residual gases was determined. The partial pressures of oxygen and water vapour were approximately 2.66×10^{-9} and 1.33×10^{-9} Pa respectively, as estimated by their relative peak heights. Subsequent surface characterization was accom-

plished with the AES. Thereafter, the ion pump was turned off in order to eliminate background electrons and negative ions originating in the ion pump. UHV conditions were maintained by the titanium sublimation pump. The procedure resulted in a constant background count rate of approximately 9 counts s^{-1} . Positively charged ions were detected in the proper mode with the ion pump on. At a CEM gain of approximately 10^6 the background count rate was again 9 counts s^{-1} .

4 Results of preliminary experiments

Preliminary experiments with anodically oxidized aluminium covered with a dense oxide film approximately 200.0 nm thick served to confirm several characteristics of tribostimulated emission which have been established by previous investigators (Gieroszynski and Sujak 1965, Sujak *et al* 1965, Sujak and Gieroszynski 1970, Arnott and Ramsey 1971). These are summarized below.

(i) Emission begins within the first 10 s after deformation commenced at a rate of 2.2×10^{-4} , i.e. at strains of less than 0.2%. An independent study of the fracture of anodically grown aluminium oxide deformed in vacuum (Grosskreutz 1967) suggests that the fracture strain of the oxide is of the order of $(2.3 \pm 1.3) \times 10^{-2}$. This observation indicates that the emission is associated with cracking or fracture of the oxide film.

(ii) As illustrated in figure 4, emission is observed only at finite or non-zero strain rates, and ceases abruptly once deformation is stopped.

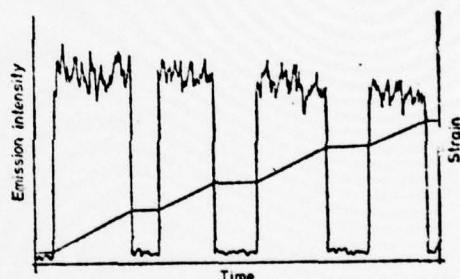


Figure 4 The dependence of tribo-stimulated emission on time and strain.

(iii) Emission occurs discontinuously, i.e. in bursts. This was noted by observing the output pulses of the CEM on the oscilloscope and by the spiked nature of the emission (figure 4).

(iv) During continuous deformation in total darkness at a constant strain rate, the electron emission rate increases rapidly to a maximum, then decreases monotonically as shown in figure 5, where electron emission rates and the stress-strain curve for a specimen deformed at a rate of $2.2 \times 10^{-4} \text{ s}^{-1}$ are compared. The emission rate plotted in figure 5 represents the emission above background and has been corrected for the detection efficiency of the CEM which, for electrons, was assumed to be 0.25. For a 200.0 nm thick oxide film and a strain rate of $2.2 \times 10^{-4} \text{ s}^{-1}$, the emission peak occurred at about 4% strain, in fair agreement with observations by Gieroszynski and Sujak (Gieroszynski and Sujak 1965, Sujak *et al* 1965, Sujak and Gieroszynski 1970) and Arnott and Ramsey (1971). The emission showed no apparent correlation with macroscopic deformation behaviour of the substrate, again implying that the emission is associated with cracking or fracture of the oxide film.

(v) Even under the most favourable conditions, the emission

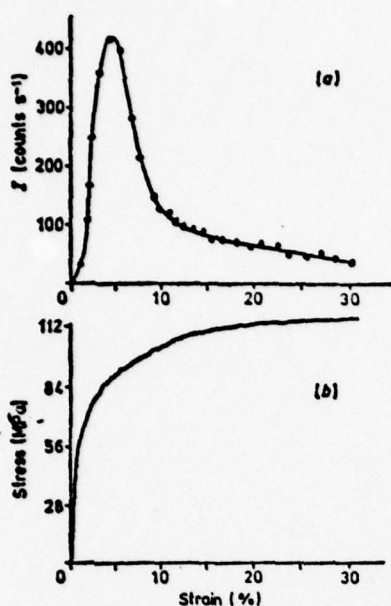


Figure 5 (a) Tribostimulated electron emission as a function of strain for an aluminium specimen covered with dense oxide film 200.0 nm thick, deformed at a rate of $2.2 \times 10^{-4} \text{ s}^{-1}$. (b) Corresponding stress-strain curve.

yield of tribostimulated electrons was extremely low. For example, for electron emission from aluminium covered with 226.0 nm thick anodized oxide film deformed in tension at a rate of $7.34 \times 10^{-3} \text{ s}^{-1}$, the emission was 400 counts s^{-1} , corresponding to a maximum emission rate of approximately $5 \times 10^{-13} \text{ A m}^{-2}$. The sensitivity of the described apparatus was sufficient to detect previously unobserved tribo-emission from naturally ($\sim 5.0 \text{ nm}$) grown oxide films on aluminium. Thus, the charged particle detection and counting technique employed in the present investigation proved to be sufficiently sensitive and yielded reproducible results to within 10% (figure 6).

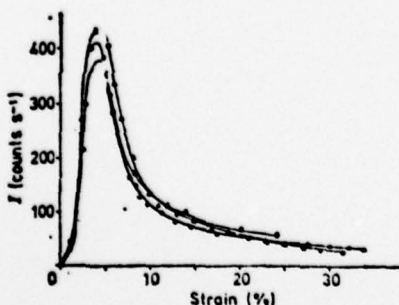


Figure 6 Tribostimulated electron emission as a function of tensile strain for aluminium specimens covered with dense oxide film 200.0 nm thick, deformed at a strain rate of $2.2 \times 10^{-4} \text{ s}^{-1}$. The three curves shown here were obtained on supposedly identical specimens and illustrate the degree of reproducibility achieved.

Using magnetic discrimination, it was established that the current of negatively charged particles emitted from oxide-covered aluminium consisted of both electrons and negative ions (figure 7). The emission of both species showed the same

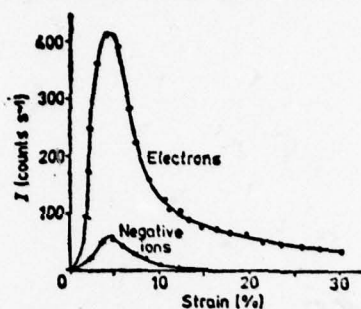


Figure 7 The rates of tribostimulated emission of electrons and negatively charged ions as a function of tensile strain, emitted from aluminium covered with anodically grown dense oxide 200.0 nm thick, deformed at a rate of $2.2 \times 10^{-4} \text{ s}^{-1}$.

behaviour as a function of strain, namely initiation at low strains (0.2%) and a rapid increase to a peak at about 4% strain, followed by a monotonic decrease in intensity at higher strains. The emission rate for electrons was corrected for the 0.25 detection efficiency; negatively charged ions were detected with near-unity efficiency. Since the positive-ion emission was extremely weak, higher strain rates had to be used for this case (figure 8). The strain dependence of the positive-ion emission is

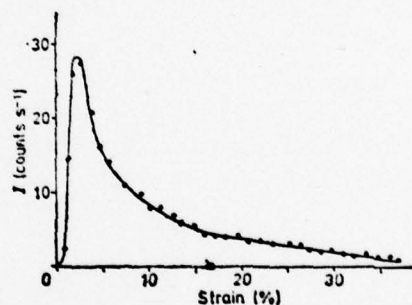


Figure 8 Tribostimulated emission rates of positively charged ions as a function of strain, emitted from dense aluminium oxide film, 200.0 nm thick, on aluminium deformed at a rate of $5.3 \times 10^{-4} \text{ s}^{-1}$.

essentially the same as that of negatively charged particles; however, due to the higher strain rate, the peak shifted to lower strain as expected (Gieroszynski and Sujak 1965, Sujak *et al* 1965, Sujak and Gieroszynski 1970).

The spontaneous emission of photons was detected in a separate experiment. Figure 9 shows the relative photon yield above background as a function of strain. Since the yield of tribostimulated photons was very small, no attempt was made to determine their spectral distribution. Consequently no correction could be made to account for the quantum efficiency of the S-20 photocathode.

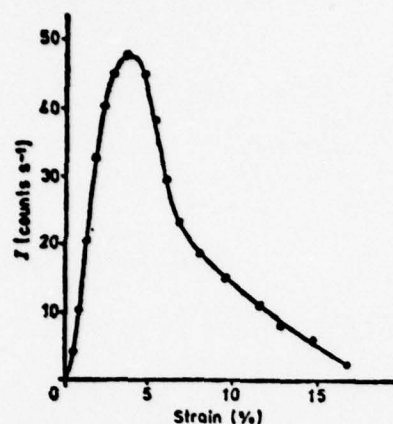


Figure 9 Relative intensity of tribostimulated photon emission as a function of strain, emitted from 200.0 nm thick, dense Al_2O_3 film on aluminium, deformed at a rate of $2.2 \times 10^{-4} \text{ s}^{-1}$.

Auger electron spectroscopy revealed a number of impurities in the surface of the electrolytically grown aluminium oxide, such as boron which was introduced during oxidation in the ammonium borate electrolyte. In addition, the appearance of the 'metallic' aluminium Auger line after deformation was a clear indication that the oxide layer had indeed ruptured, exposing fresh aluminium surfaces inside the cracks. Prior to deformation only the 'oxidic' aluminium line was detectable.

Measurements of the energy of tribostimulated emission of negatively charged particles yielded retardation curves (figure 10). We assumed that the measured energies corresponded to the energy of the emitted electrons and not of negative ions for the following reasons. (a) Since the input of the CEM in the high-sensitivity RPA was biased at +300 V with respect to the specimen, the detection efficiency for ions was small compared to that for electrons; and (b) it was shown previously that electrons were the predominant species in the emitted current.

The energy distribution was obtained by graphical differentiation of the retardation curve and is shown as curve A in figure 10(b), together with the energy distribution (for calibration purposes) of thermionic electrons emitted from a tungsten filament. The energy distribution of the tribostimulated electrons is broad: (the full width at half-maximum (FWHM) is approximately 3 eV). The FWHM of the energy distribution of the thermionic electrons is approximately 1 eV and is attributed to the potential drop across the filament.

The energy values indicated on the abscissa of figure 10(b) are relative to the Fermi level of the retarding grid. In measuring energy distributions of charged particles with retarding-potential-type analysers, we obtain the absolute energy from the measured value, i.e. the value of the retarding potential, by correcting the latter for the work function of the retarding grid. Since the thermionic emission of electrons from metals originates at the Fermi level, the true electron energy is obtained by adding the contact potential difference (i.e. the difference between the work functions of the retarding grid and emitter) to the measured energy (Parker and Wilson 1971). In the case of tribostimulated emission from oxide-covered metals, the origin of the emitted electrons and the precise value of the work function of the oxide are not known. The electrons may originate from within the oxide or, as pointed out by Arnott and Ramsey (1971), from dangling bonds created during fracturing of the oxide. Consequently, the true energy of the

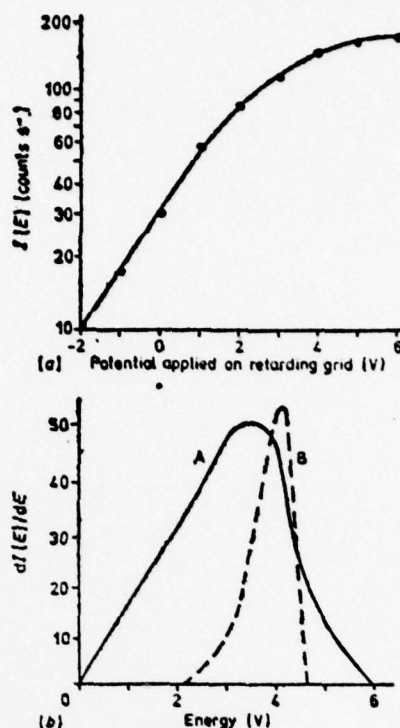


Figure 10 (a) A retardation curve for tribostimulated electrons emitted from an aluminium specimen covered with dense oxide film 200.0 nm thick, deformed at a rate of $2.2 \times 10^{-4} \text{ s}^{-1}$. (b) Energy distribution of tribostimulated electrons emitted under the above conditions shown in curve A, and energy distribution of thermionic electrons shown in curve B.

tribo-emitted electrons could not be determined since no correction factor could be established. Therefore, we present the energy of the emitted electrons with respect to the Fermi level of the retarding grid made from pure polycrystalline nickel. Its average work function was taken as 5 eV; this value was added to the measured value of the energy, i.e. to the negative of the value given on the abscissa of figure 10(a).

5 Conclusion

Results obtained with the tribostimulated emission apparatus described in this paper underscore its versatility and sensitivity. An important aspect of this apparatus lies in the ability to perform tribo-emission studies under well defined surface and environmental conditions as well as the ability to characterize the emission products in terms of their particle identity and energy. These steps are important for obtaining reliable quantitative data necessary to develop an understanding of the types of emission phenomena discussed in this paper.

With this apparatus, previously established characteristics of the tribostimulated emission were confirmed and important new insights into the mechanism responsible for it were developed.

Results of more detailed experiments with oxide-covered aluminium, nickel, and titanium will be reported elsewhere together with a detailed discussion of the correlations between

the fracture dynamics of the oxide layer and features of associated tribo-emission.

Acknowledgments

The authors would like to express their appreciation to Professor P K Rol for his keen interest, numerous suggestions and comments. Thanks are also extended to Mr M Haiman for his excellent service in machining parts for the apparatus. This work was sponsored by the Air Force Office of Scientific Research.

References

- Adams J and Manley B W 1966 *IEEE Trans. Nucl. Sci.* NS 66 88
- Arnott D R and Ramsey J A 1971 *Surface Sci.* 28 1
- Bohun A, Sak J and Psenickova M 1965 *Czech. Z. Phys.* 15 667
- Bohun A 1970 *Proc. 3rd Int. Symp. on Exoelectrons*, eds O Holzapfel and W Kaul (Braunschweig: PTB) pp 318-54
- Borroun C N, Lieber A J and Zaviantseff V T 1967 *Rev. Sci. Instrum.* 38 1477
- Brotzen F R 1967 *Phys. Stat. Solidi* 22 9
- Brus L E and Comas J 1971 *J. Chem. Phys.* 54 2771
- Grandall D H, Ray J A and Cisneros C 1975 *Rev. Sci. Instrum.* 46 562
- Delchar T A 1967 *J. Appl. Phys.* 38 2403
- Frank L A, Henderson N K and Swisher R L 1969 *Rev. Sci. Instrum.* 40 685
- Gesell T F, Arakawa E T and Callicott T A 1970 *Surface Sci.* 20 174
- Gieroszynski A and Sujak B 1965 *Acta Phys. Pol.* 28 311
- Goto K and Ishikawa K 1972 *Rev. Sci. Instrum.* 43 427
- Graham M J, Sproule G I, Caplan D and Cohen M 1972 *Electrochem. Soc.* 119 883
- Grosskreuz J C 1967 *Surface Sci.* 8 173
- Grunberg L 1958 *Br. J. Appl. Phys.* 9 85
- Huchital D A and Rigden J D 1972 *J. Appl. Phys.* 43 2291
- Kelly P and Himmel L 1976 *Comm. Solid St. Phys.* 7 81
- Knorr K and Leslie J D 1974 *Thin Solid Films* 23 101
- Kortov V S, Mints R I, Myasnikov I E and Gaprindoshvili A Y 1970 *Phys. Stat. Solidi a* 3 13
- Kortov V S and Myasnikov I E 1972 *Phys. Stat. Solidi a* 9 119
- Linke E 1970 *Angew. Phys.* 29 241
- McCarrol B 1969 *J. Chem. Phys.* 50 4758
- Parker M E and Wilson J M 1971 *Auger Transitions Between 0 and 1500 eV* (London and Bristol: Institute of Physics)
- Rosenblum B 1976 *PhD Dissertation* Wayne State University, Detroit, Michigan
- Schmidt K C 1969 *Bendix Corporation Technical Note* 9803
- Staib P 1972 *J. Phys. E: Sci. Instrum.* 5 484
- Sujak B, Gieroszynski A and Pega E 1965 *Acta Phys. Pol.* 28 61
- Sujak B and Gieroszynski A 1970 *Acta Phys. Pol. A* 37 733
- Tajima S 1970 *Adv. Corrosion Sci. Tech.* 1 229
- Tibol G J 1964 *J. Electrochem. Soc.* 111 1368

Spontaneous emission of charged particles and photons during tensile deformation of oxide-covered metals under ultrahigh-vacuum conditions^{a)}

B. Rosenblum,^{b)} P. Bräunlich,^{c)} and L. Himmel

College of Engineering, Wayne State University, Detroit, Michigan 48202

and

The Bendix Corporation, Southfield, Michigan 48076

(Received 16 June 1977; accepted for publication 9 August 1977)

Using Channeltron-type detectors and magnetic discrimination techniques, it has been shown that electrons, positive and negative ions, and photons are all emitted spontaneously while oxide-covered metals such as Al and Ni are being deformed in a tensile mode in a vacuum of approximately 10^{-10} Torr in total darkness. For dense anodically grown Al_2O_3 films of a given thickness on high-purity Al substrates, the emission yields of all charged particles and photons are found to exhibit identically the same strain dependence. The same applies to compact thermally grown NiO films on Ni. It is concluded from these and other observations that the entire emission spectrum is generated simultaneously as a result of the formation and propagation of cracks in the oxide film during the deformation process. The shortcomings of previously proposed models for this type of triboinduced emission are pointed out, and some alternative suggestions regarding the emission mechanism are offered.

PACS numbers: 79.75.+g

I. INTRODUCTION

Tribostimulated exoemission of charged particles is a weak transient phenomenon that is observed from a variety of oxide-covered metals during mechanical deformation or abrasion.¹⁻⁵ It has to be distinguished from a number of other so-called exoemission processes that occur when dielectric or semiconducting materials are subjected to external stimulation in the form of photons (photostimulated exoemission)^{6,7} or temperature increase (thermally stimulated exoemission).⁸ Freshly prepared metal surfaces may give rise to chemistimulated exoemission when they are allowed to react with certain chemical active gases.⁹

In order to study one of these emission processes, the experiments have to be performed such that all other sources of stimulation are eliminated. Tribostimulated exoemission from oxide-covered metals must therefore be investigated under conditions which preclude the occurrence of chemical and thermal stimulation as well as photostimulation. This can be done in ultrahigh vacuum in total darkness at a fixed temperature, e.g., room temperature.

In the past 10 years, a number of experiments on tribostimulated emission from oxide-covered metals have been carried out under fairly well-controlled environmental conditions. Basically, two modes of surface deformation were employed: (a) scratching the specimen with a scribe or abrading it with a steel brush and (b) tensile deformation. The emission from oxide-covered aluminum,^{1-3,5} magnesium,² and nickel^{4,5} was studied at various oxide thicknesses and strain rates. During tensile deformation, the emission was found to occur in bursts after initiation at a rather low strain ($\approx 0.2\%$). Its intensity depends on oxide thickness

and on the rate at which the sample strain increases with time. Emission is observed only during ongoing deformation or abrasion and ceases abruptly when these forms of mechanical stimulation are interrupted.

The mechanism responsible for tribostimulated exoemission is not known in detail. Clearly, emission occurs only during the propagation of cracks or during the disruption of the continuity of the oxide film during abrasion. Gieroszynski *et al.*^{1,4,6} have suggested the so-called electrified fissure mechanism, according to which the walls of propagating cracks are assumed to be oppositely charged and the resulting intense electric fields to be sufficient to cause field emission of electrons. On the other hand, Arnott and Ramsey³ proposed that the strain energy released at the tip of the propagating crack may lead in some unspecified way to the emission of electrons. All previous authors observed only negatively charged particles and assumed these to be electrons.

The present investigation was carried out with the goal to contribute toward a better understanding of tribostimulated exoemission by measuring the properties of the emitted particles and by correlating the obtained experimental results with known properties of the fracture of oxide layers on metals.

II. EXPERIMENTAL PROCEDURES

The apparatus assembled for these studies consisted of an ultrahigh-vacuum system which incorporated a fully instrumented tensile straining device, an Auger electron spectrometer, a residual gas analyzer, and a special high-sensitivity low-resolution electron energy analyzer. Single-event Channeltron electron multipliers (CEM) were employed for the detection of charged particles and a single photon counter with a S-20 photocathode (Bendix BX754) for the measurement of photons in the visible region of the electromagnetic spectrum. This system is described in detail elsewhere.^{5,10}

^{a)}Sponsored by the Air Force Office of Scientific Research.

^{b)}Present Address: Bendix Corporation, Kansas City Division, Kansas City, Mo. 64141.

^{c)}Present Address: Department of Physics, Washington State University, Pullman, Wash. 99164.

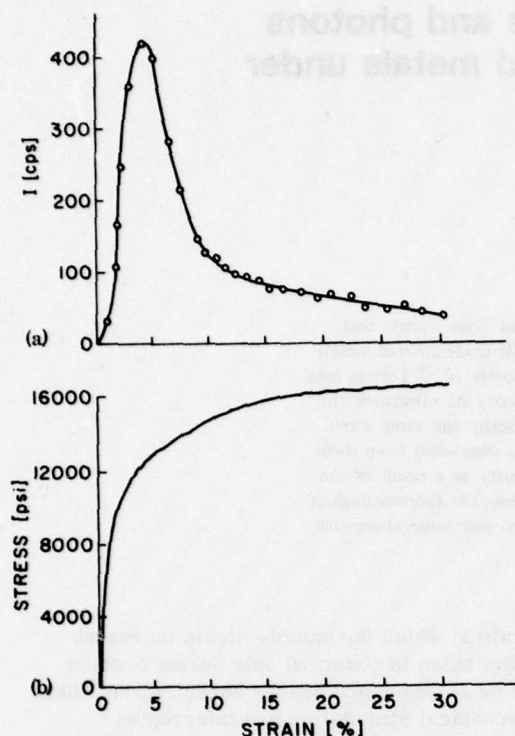


FIG. 1. Tribostimulated electron emission rates versus strain obtained from an aluminum specimen covered with dense 2000-Å-thick aluminum oxide. Deformation rate $\dot{\epsilon} = 2.2 \times 10^{-4} \text{ sec}^{-1}$. (b) Stress-strain curve.

All experiments were carried out at room temperature in total darkness at a pressure of 10^{-10} Torr. This reduced the background count rate to approximately 5 cps. These experimental conditions also eliminated any possibility of chemistimulated, photostimulated or thermally stimulated emission. All samples were high-purity polycrystalline metals obtained from MRC in the form of cold-rolled 0.5-mm-thick sheets. Tensile specimens were machined from the "as-received" strips and then recrystallized in vacuum to obtain an average grain size of approximately 0.1 mm. Dense adherent Al_2O_3 films were grown on Al by anodic oxidation using ammonium pentaborate in water as the electrolyte.¹¹ Dense adherent NiO films were formed on Ni by thermal oxidation in high-purity oxygen.¹² TiO_2 films between 1500 and 2000 Å thick were grown on Ti electrolytically¹³ and by plasma oxidation.¹⁴ In all anodic oxidation procedures, the voltage across the cell was increased linearly with time over several min until it reached the specified value necessary to produce the desired oxide film thickness. Thereafter, it was held constant for 1 h. This precaution was taken in order to minimize the stresses induced in the oxide during growth and to achieve nearly stoichiometric oxides.¹⁵ During specimen installation, extreme care was taken to avoid contamination of the surfaces and to prevent cracking or rupture of the film. After installation, the system was baked at $\approx 150^\circ\text{C}$ for 24 h.

III. RESULTS

Several characteristics of tribostimulated emission from dense oxides on nominally pure aluminum and nickel which had been established by previous investigators^{1,3,4} were confirmed by our experiments:

(i) It commences at strains less than 0.2%, corresponding to the fracture strain ($0.23 \pm 0.3\%$) of anodically grown oxide on Al.¹⁶

(ii) It is observed only at finite or nonzero strain rates and ceases abruptly once deformation is stopped.

(iii) On continuous deformation in total darkness at a constant strain rate, the electron emission rate increases rapidly to a maximum, then decreases monotonically as shown in Fig. 1, where a comparison is given between electron emission rates and the stress-strain curve for a specimen deformed at a rate of $2.2 \times 10^{-4} \text{ sec}^{-1}$. In aluminum covered with 2000 Å aluminum oxide, the peak occurs at approximately 4% strain in agreement with the observations made by Gieroszynski and Sujak¹ and Arnott and Ramsey.³

(iv) The emission yield of tribostimulated electrons is extremely low. At the peak, the emission flux is typically $5 \times 10^{-17} \text{ A/cm}^2$ of specimen surface area at a strain rate of $2.2 \times 10^{-4} \text{ sec}^{-1}$. This is of the same order of magnitude as found by Arnott and Ramsey.³

(v) Upon deformation, a system of more or less equally spaced cracks develops in thick ($> 500 \text{ Å}$) aluminium oxide, running normal to the tensile direction.

Our experiments with oxide-covered aluminum, nickel, and titanium have revealed new features, the most important being that electron emission from oxidized Al and Ni is accompanied by the simultaneous emission of low-energy positive and negative ions as well as photons. These results are described in Secs. IIIA–IIIC.

A. Emission from dense-oxide-covered aluminum

Aluminum covered with oxide films between approxi-

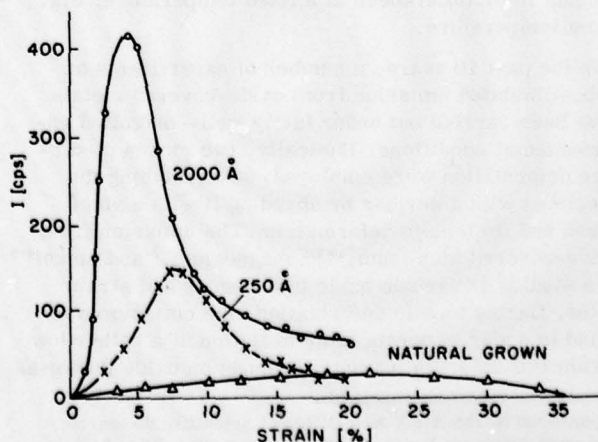


FIG. 2. Tribostimulated emission rates versus strain obtained from dense aluminum oxide of various thicknesses on aluminum. Deformation rate $\dot{\epsilon} = 2.2 \times 10^{-4} \text{ sec}^{-1}$.

AD-A059 562

WASHINGTON STATE UNIV PULLMAN DEPT OF PHYSICS

F/G 11/6

CHARACTERISTIC EXOEMISSION FROM OXIDE COVERED ALUMINUM ALLOYS.(U)

JUL 78 P BRAUNLICH, J T DICKINSON

F49620-77-C-0042

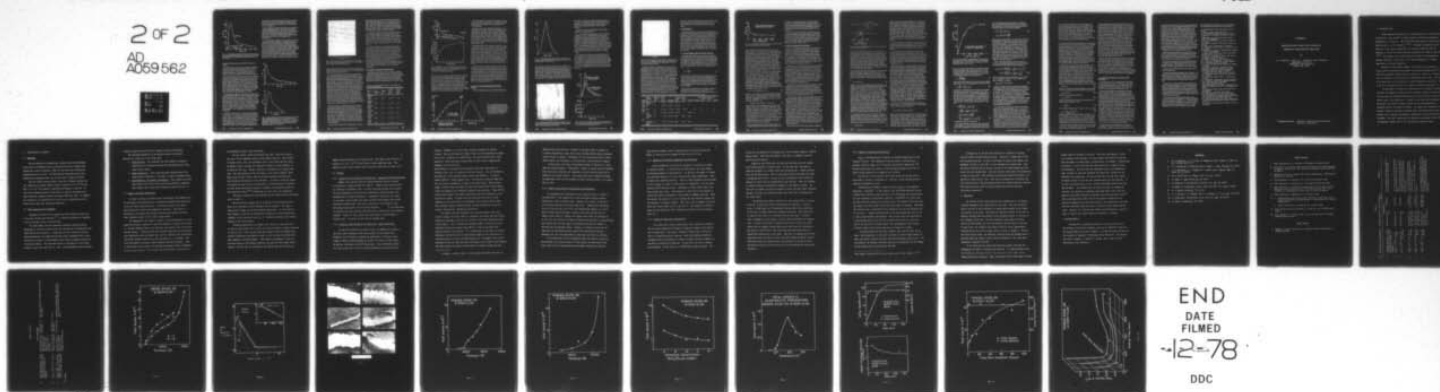
UNCLASSIFIED

AFOSR-TR-78-1354

NL

2 of 2

AD
A059562



END

DATE

FILMED

12-78

DDC

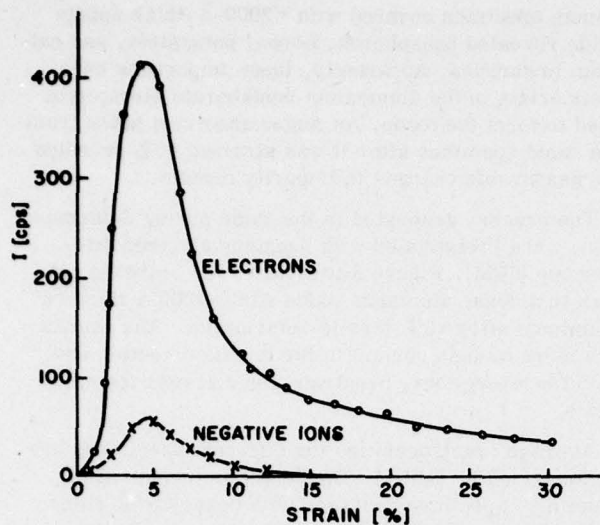


FIG. 3. Tribostimulated emission rates of electrons and negative ions versus strain obtained from aluminum covered with 2000-Å-thick dense aluminum oxide. Deformation rate $\dot{\epsilon} = 2.2 \times 10^{-4} \text{ sec}^{-1}$.

mately 50 (naturally grown) and 2000 Å thick were studied.

The dependence of the electron emission intensity on strain at a constant strain rate of $2.2 \times 10^{-4} \text{ sec}^{-1}$ is illustrated in Fig. 2 for dense-oxide films on Al of various thicknesses. The peak position shifts to a higher strain as the thickness of the oxide decreases.

Similar observations were made by Gieroszynski and Sujak¹ and Arnott and Ramsey.³ However, the former authors¹ have reported a limiting oxide thickness of approximately 500 Å below which no emission was detected. Arnott and Ramsey³ also failed to observe any tribostimulated emission from oxide thickness below 450 Å, attributing this to the limitations of their detection and recording technique. In the present investigation, emission was detected even from natural air-formed oxide films approximately 50 Å thick.

By employing a magnetic discrimination technique,¹⁰ it was established that the current of negatively charged particles emitted from oxide-covered aluminum consists of both electrons and negative ions (Fig. 3). The emission rate for electrons was corrected for the estimated detection efficiency of 0.25.¹⁰ Negatively charged ions were detected with an efficiency of approximately unity.¹⁰ Since electrons and negatively charged ions are emitted simultaneously, one common mechanism appears to be responsible for both emission phenomena.

Emission of positive ions and photons was detected for the first time. However, at the low strain rate of $2.2 \times 10^{-4} \text{ sec}^{-1}$, the emitted particle flux was weak and almost buried in the background. In order to obtain higher emission currents, the specimen was deformed at the higher rate of $5.3 \times 10^{-4} \text{ sec}^{-1}$ [Fig. 4(a)]. The strain dependence of the positive ion emission is essentially the same as that of negatively charged parti-

cles; however, due to the higher strain rate, the peak is shifted to a lower strain. Similar shifts were observed by Sujak and Gieroszynski for tribostimulated electron emission.¹

The spontaneous emission of photons was detected in separate experiments [Fig. 4(b)]. Since the yield of tribostimulated photons is very small, no attempt was made to determine their spectral distribution. Consequently, no correction could be made to account for the quantum efficiency of the employed S-20 photocathode.

In order to better understand the mechanism of tribostimulated particle emission, an attempt was made to measure the energy of negatively charged particles. Due to the low emission currents, the measurements of only retardation curves was possible without magnetic particle discrimination. We assumed, however, that the measured energies correspond to the energy of the emitted electrons since (a) the input of the charged-particle detector (CEM) in the high-sensitivity electron energy analyzer biased at +300 V with respect to the specimen, for which the detection efficiency for ions is

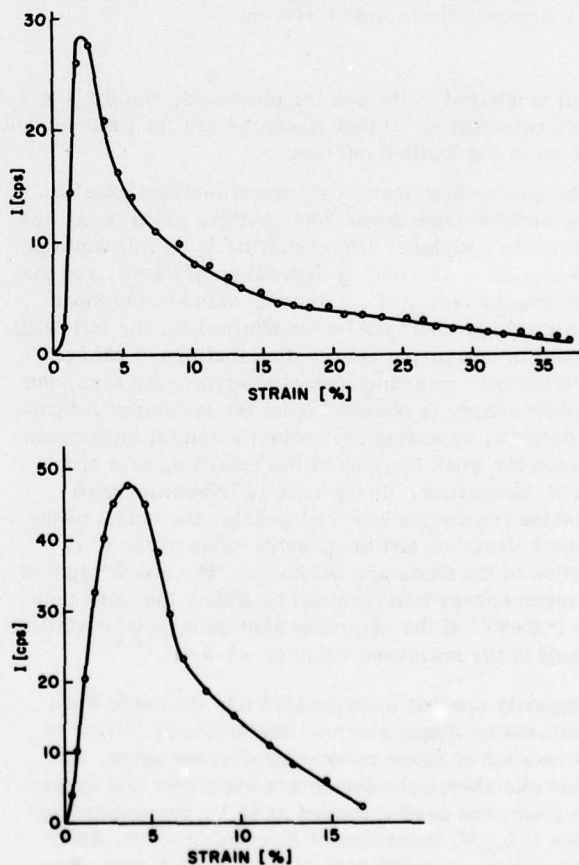


FIG. 4. Tribostimulated emission rates of positive ions versus strain obtained from aluminum covered with 2000-Å-thick dense oxide. Deformation rate $\dot{\epsilon} = 5.3 \times 10^{-4} \text{ sec}^{-1}$. (b) Relative intensity of tribostimulated photon emission versus strain obtained from aluminum covered with dense aluminum oxide. Deformation rate $\dot{\epsilon} = 2.2 \times 10^{-4} \text{ sec}^{-1}$.

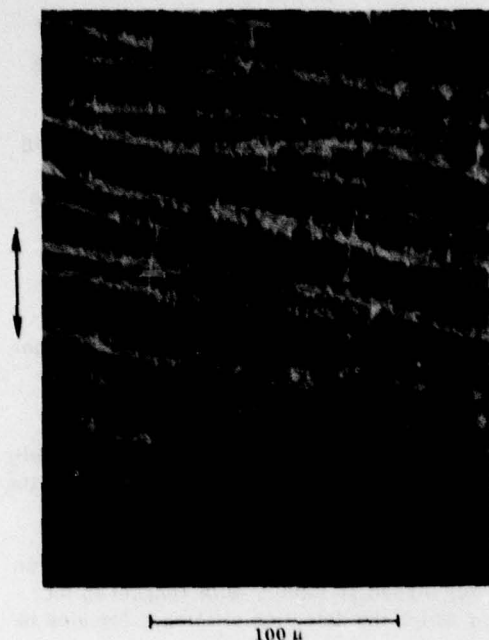


FIG. 5. SEM micrograph of crack pattern in a 2000-Å-thick dense-oxide layer on aluminum after 40% strain. Magnification 500 \times . Arrows indicate tensile direction.

small compared to the one for electrons, and (b) it was shown before (Fig. 3) that electrons are the predominant species in the emitted current.

The energy distribution of tribostimulated exoelectrons emitted from dense 2000-Å-thick oxide on Al was obtained by graphical differentiation.¹⁰ Its full width at half-maximum (FWHM) is approximately 3 eV, and the mean energy is 3.5 eV. The exact value of the mean kinetic energy could not be determined for the following reason: In measuring energy distributions of charge particles with retarding-potential-type analyzers, the absolute energy is obtained from the measured retarding potential by adding the contact potential (difference between the work function of the retarding grid and that of the emitter). In the case of tribostimulated emission from oxide-covered metals, the origin of the emitted electrons and the precise value of the work function of the oxide are not known. The above value of the mean energy was obtained by adding the work function (~ 5 eV)¹⁷ of the retarding grid (pure polycrystalline nickel) to the measured value of -1.5 eV.¹⁸

Impurity species incorporated into the oxide were monitored by Auger electron spectroscopy. Prior to deformation of dense natural air-formed oxide, the detectable chemical species are aluminum and oxygen. The aluminum peak appeared at 45 V, corresponding to the $L_{2,3}M_1$ transition of Al in oxide form. After deformation, an additional Al peak at 64 V was measured which is characteristic of metallic aluminum.¹⁹ This provides clear evidence that aluminum surfaces were exposed due to cracking of the oxide during tensile deformation.

Auger spectra taken prior to deformation of an alu-

minum specimen covered with ≈ 2000 -Å-thick anodic oxide revealed phosphorus, boron, potassium, and calcium impurities. Apparently, these impurities have their origin in the ammonium pentaborate electrolyte used to form the oxide. An Auger spectrum taken from the same specimen after it was strained 40% revealed no measurable changes in impurity content.

The cracks, generated in the oxide during deformation, were investigated with scanning electron microscopy (SEM). Figure 5 illustrates the cracking pattern in a dense aluminum oxide film ≈ 2000 Å thick on aluminum after 40% tensile deformation. The cracks run more or less normal to the tensile direction and, with few exceptions, penetrate clear across the gauge width.

Average crack densities for different specimens are summarized in Table I. The densities measured for aluminum specimens covered with dense-oxide films approximately 1000–2000 Å thick are only about one-third of the values reported by Arnott and Ramsey.³ This discrepancy may be due to the fact that they deformed the specimens for crack density measurements in air, while the values reported in Table I were obtained by deformation in an ultrahigh vacuum. Grosskreutz¹⁶ pointed out that the mechanical properties of oxide films depend strongly on environmental conditions, especially the humidity of the surrounding atmosphere.

B. Emission from thermally oxidized nickel

Tribostimulated emission from thermally oxidized nickel shows characteristics similar to those observed in dense anodically grown aluminum oxide. The emitted particles are electrons and ions, as well as photons. Emission commences at low strains ($< 0.2\%$) and is observed only during ongoing deformation. Figure 6(a)

TABLE I. Average crack spacings and crack densities for oxide-covered specimens.

Substrate and oxide	Oxide thickness (Å)	Tensile strain (%)	Average crack spacing (mm)	Average crack density (mm ⁻¹)
Aluminum Dense oxide	1000	42.5	1.4×10^{-2}	71.4
Aluminum Dense oxide	2000	40.5	1.9×10^{-2}	52.6
Aluminum Dense oxide	2000	44.5	1.7×10^{-2}	58.8
Aluminum Dense oxide	2000	27.5	2.0×10^{-2}	50
Aluminum Dense oxide	2000	28.2	2.1×10^{-2}	47.6
Nickel Dense oxide	2000	40	3.7×10^{-3}	270.2

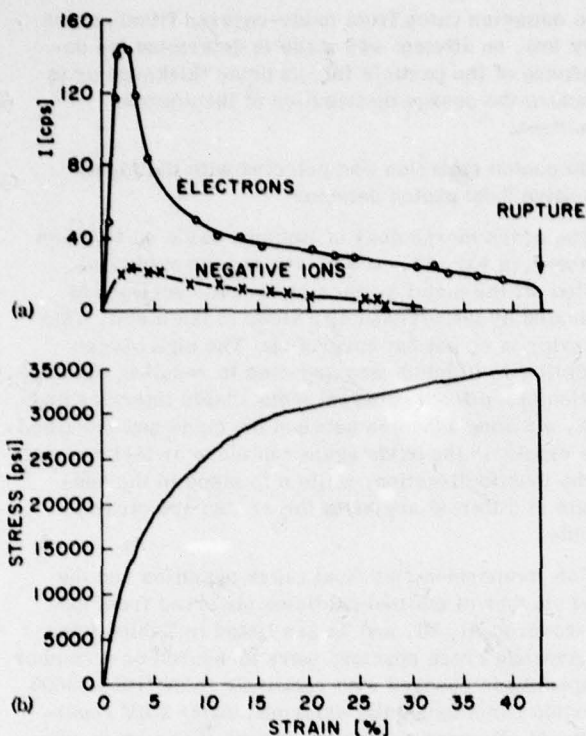


FIG. 6. (a) Relative rates of tribostimulated emission of electrons and negative ions versus strain obtained from 2000-Å-thick nickel oxide on nickel. Deformation rate: $\dot{\epsilon} = 3.3 \times 10^{-4} \text{ sec}^{-1}$. (b) Stress-strain curve.

shows the relative emission rates of electrons and negative ions as a function of strain from a nickel specimen covered with $\approx 2000\text{-}\text{\AA}$ -thick oxide film. The stress-strain curve is given for comparison in Fig. 6(b). The electron emission rates are about three times smaller as compared with those from dense aluminum oxide of comparable thickness. The FWHM of the emission curves is about 5% for NiO and 4% for Al_2O_3 , suggesting that the rate of crack formation at low strains is faster in nickel oxide than in aluminum oxide.

Due to the rather low emission rates observed even from rather thick nickel oxides, no attempt was made to determine the dependence of the particle flux on oxide thickness.

With the aid of a low-resolution spectrometer,^{5,10} retardation curves were obtained for negative particles emitted from a nickel specimen covered with oxide film $\approx 2000\text{-}\text{\AA}$ thick [Fig. 7(a)]. The energy was measured for two strain intervals, one between 0 and 5% and the other between 7 and 14%. The energy distribution (FWHM $\approx 3.5\text{ eV}$) was found to be independent of strain induced in the substrate. The energies are again reported with respect to the Fermi level of the retarding grid [Fig. 7(b)].

Spontaneous photon emission was detected in a separate experiment (Fig. 8). The photon emission shows basically the same characteristics as the emission of negatively charged particles. It is noted, however, that the photon peak appears at a higher strain ($> 5\%$). This relative shift in peak position is believed to be the result of misalignment of the photon counter tube with respect to the center of the specimen's gauge. Due to the somewhat nonuniform strain distribution along the gauge, oxide failure will occur at somewhat higher apparent substrate strains at locations away from the center.

Cracks developed in nickel oxide after deformation generally run normal to the tensile direction. They are of variable lengths and widths and do not extend clear across the gauge (Fig. 9). The measured crack density given in Table I is at least a factor of 5 greater than crack density in aluminum oxide of comparable thickness. The rather high crack density and the rough appearance of the oxide surface may be attributed to the high porosity of the thermally grown NiO film which can affect its mechanical behavior.²⁰

C. Emission from anodized and plasma-oxidized titanium

Tribostimulated particle emission from oxide-cov-

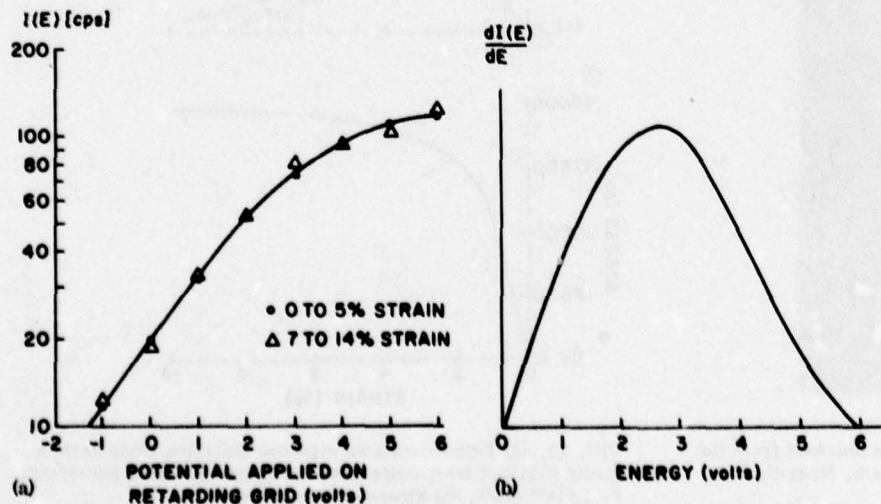


FIG. 7. (a) Retardation curve for tribostimulated electrons emitted from thermally grown 2000-Å-thick NiO on nickel. Deformation rate $\dot{\epsilon} = 3.3 \times 10^{-4} \text{ sec}^{-1}$. (b) Energy distribution of electrons emitted under conditions stated in Fig. 7(a).

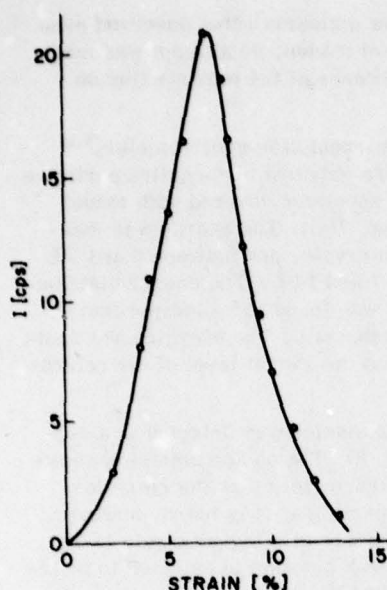


FIG. 8. Tribostimulated photon emission versus strain obtained from thermally grown 2000-Å-thick NiO on nickel. Deformation rate $\dot{\epsilon} = 3.3 \times 10^{-4} \text{ sec}^{-1}$.

ered titanium consists of electrons only. Figure 10 shows the electron emission rates as a function of strain emitted from anodized and plasma-oxidized titanium specimens with oxide coatings approximately 2000 and 1600 Å thick, respectively. The electron emission exhibits a behavior similar to those observed from dense aluminum oxides and nickel oxide of comparable thickness; however, the intensity is much lower. Since elec-



FIG. 9. SEM micrograph of crack pattern obtained from the sample described in Fig. 8 after 40% strain. Magnification 5400 \times . Arrows indicate tensile direction.

tron emission rates from oxide-covered titanium are very low, no attempt was made to determine the dependence of the particle flux on oxide thickness or to measure the energy distribution of the emitted electrons.

No photon emission was detected with the highly sensitive S-20 photon detector.

The crack morphology of titanium oxide on titanium is shown in Fig. 11. At 38% strain, the oxide had peeled off the metal surface at various locations as indicated by the exposed slip steps in the metal. This behavior is somewhat surprising. The high oxygen solubility in titanium was expected to result in the formation of a diffuse coherent metal-oxide interface and, thus, a strong adhesion between the oxide and the metal. The cracks in the oxide again run more or less normal to the tensile direction, while slip steps in the substrate at different angles to the cracks are clearly visible.

For comparison, the final crack densities and the total number of emitted particles observed from oxide-covered Al, Ni, and Ti are listed in Tables I and II. Average crack spacings were measured on a number of specimens covered with relatively thick (1000–2000 Å) oxide films uniaxially deformed under UHV conditions. In all cases examined, cracks in the oxide were more or less equispaced and ran normal to the tensile direction.

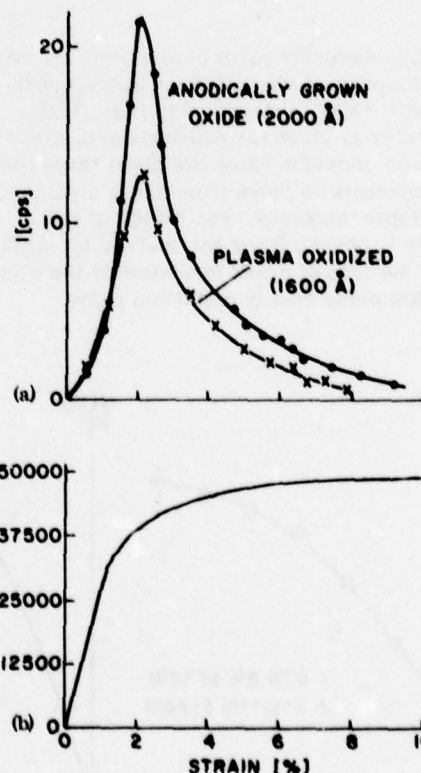


FIG. 10. (a) Tribostimulated electron emission rates versus strain obtained from oxide-covered titanium. Deformation rate $\dot{\epsilon} = 4 \times 10^{-4} \text{ sec}^{-1}$. (b) Stress-strain curve.



FIG. 11. SEM micrograph of crack pattern obtained from titanium covered with dense anodically grown 2000-Å-thick titanium oxide after 38% deformation. Magnification 1879 \times . Arrows indicate tensile direction.

The total emission of charged particles as well as photons was determined by graphical integration of the independent $I(\epsilon)$ -vs- ϵ curves. In the case of electrons, the emission was corrected to account for the 25% detection efficiency of the CEM, while no correction was necessary for ions. Furthermore, it was assumed that all charged particles emitted were collected by the detector. We believe that the electrostatic field applied between the input cone of the CEM and the specimen was strong enough to alter the trajectories of the low-energy charged particles such that they were focused into the detector. Since no focusing means were employed, we assumed that the detected photons originated from an area geometrically opposite to the photocathode. The close proximity between the specimen and the photocathode made it almost impossible for any other

photons to reach the photocathode and be detected. Thus, in calculating the total emission of photons, an area with a diameter of 6 mm was taken as the emitting region.

IV. DISCUSSION

The results obtained in the present investigation indicate that tribostimulated emission of charged particles and photons from oxide films on metal substrates depends strongly on the mechanical properties of the oxide, its thickness, and mode of fracture. In Sec. IV A, tribostimulated emission from dense oxides will be discussed first from a purely kinetic point of view; in Secs. IV B and IV C, various possible processes that may contribute to the spontaneous release of particles from the oxide film will be examined, and an attempt will be made to explain the physical nature of the emission process.

A. Tribo-stimulated emission from dense-oxide films

Tribostimulated electron emission from apparently dense-oxide films on aluminum subjected to tensile deformation under UHV conditions was first systematically investigated by Arnott and Ramsey.³ They showed that the emission is associated with rupture or fracture of the oxide layer and that the emission intensity at a given strain is proportional to the rate of crack formation, i.e.,

$$I(\epsilon) \propto \frac{dN(\epsilon)}{dt}, \quad (1)$$

where $I(\epsilon)$ is the emission current of charged particles, ϵ is the tensile strain induced in the substrate, and $N(\epsilon)$ is the total number of cracks traversing the gauge. Equation (1) is consistent with the experimental observation that triboemission occurs only while deformation is taking place and ceases abruptly once the deformation stopped.

The fracture of brittle surface coatings on strained substrates was investigated, among others,²¹ by Grosskreutz and McNeil²² who analyzed the process of

TABLE II. Total emission of tribostimulated charged particles and photons and average emission per crack.

Oxide	Oxide thickness (Å)	Maximum strain (%)	Strain rate (sec ⁻¹)	Electrons	Total emission			Average emission per crack			
					Negative ions	Positive ions	Photons	Electrons	Negative ions	Positive ions	Photons
Dense Al ₂ O ₃	Natural grown \approx 50	38	2.2×10^{-4}	1.8×10^4	2.5×10^3				
Dense Al ₂ O ₃	250	38	2.2×10^{-4}	6.5×10^4	9.3×10^3				
Dense Al ₂ O ₃	2000	38	2.2×10^{-4}	1.7×10^5	1.8×10^4	1.2×10^4		95	10	6	40
NiO	2000	38	3.3×10^{-4}	4.2×10^4	1.3×10^4	...	4.2×10^3	4	1		2
	Plasma oxidized 1600	38	4×10^{-4}	2.6×10^3	None	None	None				
TiO ₂	Anodically grown 2000	38	4×10^{-4}	4.1×10^3	None	None	None				

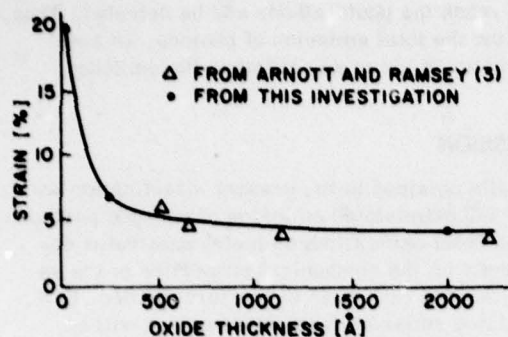


FIG. 12. Peak position of electron emission curves from dense Al_2O_3 on aluminum versus oxide thickness.

crack formation in the oxide layer in terms of its elastic properties, thickness, and the strain imposed on the substrate. They found that thin oxide films (up to about 500 Å thick) may fracture only at slip steps developed in the substrate. In polycrystalline metals, slip steps are confined to individual grains. The cracks which develop in their oxide films will, therefore, normally not run perpendicular to the tensile strain direction. This behavior was clearly demonstrated by Arnott and Ramsey.³ On the other hand, oxide films greater than about 500 Å thick on pure aluminum exhibit a system of regularly spaced cracks running normal to the tensile direction (see, e.g., Fig. 5). According to Grosskreutz,²³ the first few cracks nucleate at microimperfections or defects in the oxide film. They are randomly spaced at rather wide intervals and, upon further straining of the substrate, they increase in number until most of the "available" microimperfections have developed into cracks at $\epsilon = \epsilon_0$, resulting in a fairly regular average spacing d_0 between cracks. Thereafter, further straining will predominantly result in crack formation according to the Grosskreutz mechanism.^{22,23} The crack density $\rho(\epsilon)$ per unit gauge length is then given by

$$\rho(\epsilon) = \rho_0 + (1/4g) \ln(\epsilon/\epsilon_0), \quad \epsilon > \epsilon_0, \quad (2)$$

where $\rho_0 = 1/d_0$ and g is related to the oxide thickness D via $g = KD^{1/2}$, K being a constant.²³ During the deformation, the gauge length $L_g(\epsilon) = L_g(0)(1 + \epsilon)$, and we have $N(\epsilon) = \rho(\epsilon)L_g(0)(1 + \epsilon)$. Thus, for $\rho > \rho_0$ (or $\epsilon > \epsilon_0$), one obtains with Eq. (2)

$$I = \zeta L_g(0) \{ \rho_0 + (1/4g) [1 + \epsilon^{-1} + \ln(\epsilon/\epsilon_0)] \}. \quad (3)$$

The parameter ζ does not depend on ϵ and will be discussed in Sec. IV B. At a constant strain rate $\dot{\epsilon}$, the emission intensity I is, according to Eq. (3), a monotonically decreasing function of ϵ which describes the tail of the emission curve ($\epsilon > 5\%$ or so). However, it does not account for the occurrence of the peak. This is to be expected since Eq. (3) is restricted to $\epsilon > \epsilon_0$. At the present time, the rate of crack formation in the strain region for $0 \leq \epsilon \leq \epsilon_0$ is not known, and, thus, a complete description of the exoemission curve as a function of strain is still unavailable.

Thin dense-oxide films in which cracks develop at slip steps exhibit much broader emission peaks, and,

in addition, the peak position is a function of oxide thickness (Fig. 12). Above 500 Å, the peak position remains unaffected by the oxide thickness. This may be interpreted as an indication of the different fracture modes observed for thin and thicker oxide layers on aluminum.

The above analysis is additional evidence that tribo-stimulated emission from dense oxides is correlated with the rate of crack formation in oxide films. It does not account, of course, for the nature of the emission or the mechanism by which the emitted particles acquire their kinetic energy. These questions will be addressed in Secs. IV B and IV C.

B. Possible mechanisms for the emission

Basically, two different mechanisms have been proposed to account for the energy required for tribo-stimulated emission of electrons from solid surfaces. Sujak and co-workers^{1,6} presented a model in which cracking of the oxide films during plastic deformation of the substrate is accompanied by charge separation across opposing crack surfaces, thus resulting in the creation of strong local fields within the fissures. These intense fields were assumed to give rise to field emission of electrons from the crack walls.

Thiessen *et al.*²⁴ proposed that the emission originates from a very-short-lived microplasma created during mechanical abrasion of dielectrics at the contact point between the abrading tool and the surface. Arnott and Ramsey³ suggested that the release of elastic strain energy at the tips of rapidly propagating cracks in the brittle oxide is responsible for the emission. Whether or not this release of strain energy leads to the formation of a microplasma of the kind proposed by Thiessen, or simply to thermionic emission of electrons and ions, was not discussed by these authors.

It is difficult to design an experiment which will make possible a clear distinction between these different mechanisms. However, the experimental results obtained in this work can be analyzed and compared with analytical predictions based on the electrified fissure model or the strain-energy-release model. This will be carried out in this section and in Sec. IV C.

The electrified fissure model has apparently received some independent support from Linke² who observed relatively strong tribostimulated electron emission from insulators such as Al_2O_3 and MgO . He failed to detect emission from semiconducting ZnO and concluded that due to the relatively high conductivity of this oxide the generation of high electric field in the fissure is impaired. However, he apparently was unaware that Gieroszynski and Sujak⁴ have detected relatively strong tribostimulated emission from NiO , generally a good semiconductor. In the present investigation, tribo-stimulated emission from nickel oxide, as well as from semiconducting titanium oxide, was detected. It is conceivable that Linke's failure to observe emission from oxide-covered Zn may simply have been due to the fact that his detection and recording apparatus lacked the required sensitivity.

One of the major results of the present investigation

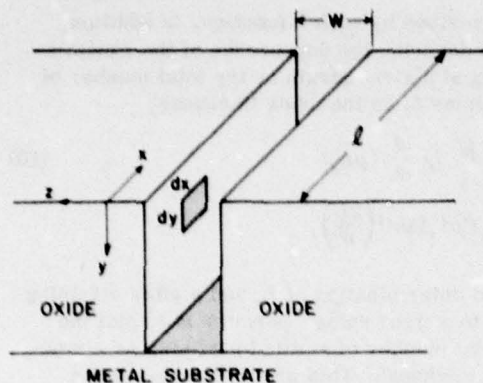


FIG. 13. Schematic representation of a crack in a thick layer of oxide on a metal substrate.

is the discovery that the emitted current consists of low-energy positive and negative ions and electrons as well as photons. All are emitted simultaneously when oxide-covered aluminum and nickel are deformed. Unfortunately, this observation does not provide sufficient evidence to discriminate between the electrified fissure model or the strain-energy-release model. Energy analysis of the negatively charged particles emitted from aluminum and nickel oxides revealed rather broad energy distributions, having low mean energies (a few eV), consistent with both models.

The strain energy per unit volume stored in an elastic medium subjected to tensile deformation is $\frac{1}{2}E\epsilon^2$,²⁵ where E is Young's modulus and ϵ is the strain. If at fracture all the strain energy could be converted into heat, the temperature of the specimen would be raised by

$$\Delta T = E\epsilon_f^2 / 2\rho^*c_p, \quad (4)$$

where ρ^* and c_p are the density and specific heat of the medium. In the case of anodically grown aluminum oxide deformed in tension in vacuum, $E \approx 2.1 \times 10^{12}$ dyn cm⁻², $\epsilon_f = 1.5 \times 10^{-3}$,¹⁶ $\rho^* = 3.3$ g cm⁻³,¹¹ and c_p (at 300 °K) = 19.9 cal mole⁻¹ °K⁻¹,²⁶ resulting in a temperature increase $\Delta T = 0.3$ °C. This is, of course, insufficient for thermionic emission. A temperature increase of this order of magnitude was actually observed by Beauchamp²⁷ for glasses with average elastic strain energy density of 5×10^6 kg cm⁻² which is comparable to that for alumina. The above calculations indicate that the emission cannot originate from the entire surface of the sample, but must be associated with the propagating cracks. A careful examination is therefore required regarding strain energy dissipation at the tip of a propagating crack where local stresses can be much higher than the average stresses in the strained oxide.

In an elastic medium, where the amount of plastic deformation prior to fracture is negligible, crack tips tend to be sharp, and the stress at the crack tip approaches infinity and decreases with distance r from the tip as $r^{-1/2}$.²⁸ For cracks with semicylindrical ends,²⁹ the maximum stress around a crack tip of radius R is

$$\sigma_c = 2\sigma(C/R)^{1/2}, \quad (5)$$

where C is half of the crack length and σ is the tensile stress normal to the tensile direction. For brittle solids, the crack-tip radius is on the order of one interatomic distance,³⁰ resulting in extremely high tensile stresses around the tip which will force the ions in the immediate vicinity of the crack tip to move far away from their equilibrium positions, thus raising their potential energy. When a crack is formed, the displaced atoms on either side of the crack will experience a restoring force which will allow them to return to their equilibrium positions, thus decreasing their potential energy.

According to Pugh,²⁸ atoms at the tip of a crack may acquire an excess energy of about $\frac{1}{2}$ eV per atom. If all that energy would be converted into heat, the local temperature at the crack tip would increase by about 3000 °K.

Since the FWHM of the energy distribution of the emitted negatively charged particles is considerably larger than the expected $\frac{1}{2}$ eV, the emission is apparently not purely thermionic and may possibly be influenced by electric fields within the crack. Such fields may not be intense enough to cause field emission, but may be sufficient to influence the kinetic energy of the emitted charged particles.

Additional information concerning the mechanism and origin of the emission from dense oxides on aluminum can be extracted from an analysis of the dependence of the emission intensity on oxide thickness. According to the electrified fissure model of Sujak and co-workers,^{1,4} the emission intensity at its peak is proportional to $D^{1/2}$ for $D \leq 2000$ Å, where D is the oxide thickness, and, furthermore, saturation occurs above $D > 2000$ Å. In contrast to this, Arnott and Ramsey³ noted that saturation occurs above an oxide thickness of about 1130 Å and concluded that the escape of electrons originating in the deeper fissures may be inhibited. These observations lead to a very important conclusion: Emission does not originate from the metal substrate because, otherwise, its intensity is expected to decrease with increasing oxide thickness, contrary to independent experimental observations. Thus, it is reasonable to assume that the emission originates from the walls of newly created cracks in the oxide. This knowledge then permits one to establish a simple phenomenological model to account for the dependence of tribostimulated emission intensity on oxide thickness.

A crack in a thick oxide film may be visualized as shown in Fig. 13. Tensile deformation occurs along the z axis. The emission per crack is

$$I_c = (1/2\pi)it_e \int_0^l \int_0^D P_n(x,y) dx dy, \quad (6)$$

where i is the intrinsic emission flux, in units of particles per cm² of wall area per sec, t_e is the time period during which emission from the newly created area $dx dy$ is actually taking place, D is the oxide thickness (crack depth), and l is the gauge width of the specimen. Only particles within a certain solid angle can escape from the crack, while the others will collide with the walls and either be neutralized or absorbed. A condi-

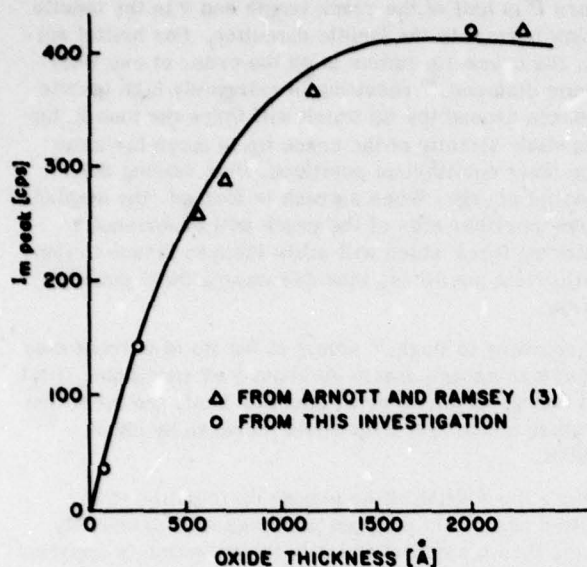


FIG. 14. Peak intensity of tribostimulated electron emission from dense Al_2O_3 films on aluminum versus oxide thickness. Deformation rate $\dot{\epsilon} = 2.2 \times 10^{-4} \text{ sec}^{-1}$. The solid line is calculated from Eq. (11) with $W = 1000 \text{ Å}$.

tion is, of course, that the mean free path of the particle must be larger than the crack dimensions, which will be discussed in more detail below. $P_0(x, y)$ is the probability that a particle will escape from the crack. In first approximation, P_0 may be taken as

$$P_0 = \frac{W(t)l(t)}{y^2 + W(t)^2}, \quad (7)$$

where $W(t)$ and $l(t)$ are the crack width and crack length, respectively. Thus, the exoemission intensity becomes

$$I = I_0 \frac{dN}{dt} = I_0 \dot{\epsilon} \frac{d}{d\epsilon} (\rho L_\epsilon). \quad (8)$$

In general, $\dot{\epsilon}$ will depend on time; however, the experiment may be carried out with a constant strain rate. The crack density ρ may be measured independently or derived from a model calculation. As an example, we discuss which form the emission intensity takes when Eq. (2) is valid. For simplicity, we assume $W(t)$ and $l(t)$ take their average values. $W(t) = \frac{1}{2} W$ and $l(t) = \frac{1}{2} l$. This permits us to determine the parameter ζ in Eq. (3):

$$\begin{aligned} I &= \frac{i t_0 W l^2}{4\pi} \left(\int_0^D \frac{1}{y^2 + W^2} dx \right) \dot{\epsilon} \\ &\times \frac{d}{d\epsilon} \left[\left(\rho_0 + \frac{1}{4KD^{1/2}} \ln \frac{\epsilon}{\epsilon_0} \right) L_\epsilon \right] \\ &= \frac{1}{2\pi} i t_0 l^2 L_\epsilon(0) \tan^{-1} \left(\frac{2D}{W} \right) \\ &\times \left[\rho_0 + \frac{1}{4KD^{1/2}} \left(1 + \epsilon^{-1} + \ln \frac{\epsilon}{\epsilon_0} \right) \right]. \end{aligned} \quad (9)$$

A comparison with Eq. (3) yields ζ .

As mentioned before, this function decreases with ϵ in the region $\epsilon > \epsilon_0$, and it is easy to show that the tail of a curve $I(\epsilon)$ measured for thick dense oxide on pure

Al can be described by such a function. In addition, Eqs. (6)–(9) describe the dependence of the exoemission intensity at a given strain or the total number of emitted particles I_T on the oxide thickness:

$$\begin{aligned} I_T &= I_0 N = \int_0^\infty I_0 \dot{\epsilon} \frac{d}{d\epsilon} (\rho L_\epsilon) \\ &= \frac{i}{2\pi} \dot{\epsilon} t_0 l^2 \rho L_\epsilon \tan^{-1} \left(\frac{2D}{W} \right). \end{aligned} \quad (10)$$

Experimental determination of L_ϵ and ρ after straining the samples to a fixed value ϵ permits us to plot the measured total number of emitted particles as a function of oxide thickness. This provides a test of the validity of crack model shown in Fig. 13. A similar test may be had by plotting $I(\epsilon)$ for samples of various oxide thickness at a given strain. For example, one might choose the peak of the $I(\epsilon)$ curve. Dense oxide of a thickness larger than 500 Å results in an $I(\epsilon)$ curve which peaks at about $\epsilon_{\text{peak}} = 0.04$ (see Fig. 12). Ramsey and Arnott have measured $\rho(\epsilon)$ and showed that at that point the crack density of all samples is virtually independent of oxide thickness.³

Thus, in the approximation of Eq. (9), which of course is not exactly applicable at the emission peak, we find with the additional assumption $\rho(\epsilon_{\text{peak}}) = \rho_0$

$$\begin{aligned} I(\epsilon_{\text{peak}}) &\propto \dot{\epsilon} \tan^{-1} \left(\frac{2D}{W} \right) \left[\rho_0 + \frac{1}{4KD^{1/2}} (1 + \epsilon_{\text{peak}}^{-1}) \right] \\ &\approx \dot{\epsilon} \tan^{-1} \left(\frac{2D}{W} \right) \left[\rho_0 + \frac{1}{4KD^{1/2}} \frac{1}{\epsilon_{\text{peak}}} \right]. \end{aligned} \quad (11a)$$

Since, according to Arnott and Ramsey, $\rho_0 = 7.5 \times 10^3 \text{ cm}^{-1}$ and with³³ $K = 0.13 \text{ cm}^{1/2}$, $\rho_0 \ll 1/4KD^{1/2}$ for $500 \leq D \leq 5000 \text{ Å}$, we have

$$I(\epsilon_{\text{peak}}) \propto \dot{\epsilon} D^{-1/2} \tan^{-1}(2D/W). \quad (11b)$$

Figure 14 shows a plot of measured peak emission intensities versus oxide thickness and, in comparison, a normalized plot of the thickness dependence as given by Eq. (11). The best fit was obtained by choosing $W = 1000 \text{ Å}$. The agreement is remarkable. The good fit in the region $D < 500 \text{ Å}$ must be considered fortuitous. Of interest is that the emission saturates above $D = 1000 \text{ Å}$, apparently the depth below which the escape of the charged particles is inhibited. Incidentally, Eq. (11) indicates a linear dependence of $I(\epsilon)$ on the strain rate $\dot{\epsilon}$ in agreement with experimental observations by Gieroszynski and Sujak.¹

It is instructive to discuss Eq. (9) in some further detail. The unknown parameters are W , t_0 , and i ; all others can be measured. Assuming the emission is thermionic in origin and results from local heating due to the release of elastic strain energy at the tip of rapidly propagating crack in brittle oxide, the time, t_0 , for an emission burst from local hot spots is estimated to be of the order of several times the reciprocal photon frequency, i.e., about 10^{-11} sec . This is the time interval during which the local temperature is expected to decay to a value below which thermionic emission is no longer significant. The total measured electron yield from a 2000-Å-thick dense aluminum oxide film

is $I_F = 1.7 \times 10^5$ (see Table II). The total number of cracks formed in the oxide film was calculated, with the aid of the measured average crack density, to be ≈ 4000 (on both sides of the sample). Inserting these figures into Eq. (10) gives with $W = 1000 \text{ \AA}$ and emission flux $i = 10^{12} - 10^{13} \text{ electrons cm}^{-2} \text{ sec}^{-1}$. It is easy to verify, with the aid of the Richardson equation, that $i = 10^{13} \text{ cm}^{-2} \text{ sec}^{-1}$ is consistent with values around 3000°K for the local surface temperature in the vicinity of a propagating crack as estimated by Pugh.²⁸

These calculations lend strong support to the idea that the emission is of thermionic origin. Thus, the release of strain energy in the vicinity of a propagating crack results in local heating to a temperature sufficient to cause thermionic emission from the walls. It is conceivable that some charging occurs at local hot spots, due to the emission of charged particles as suggested by Henry.³¹ This type of charging may be responsible for the generation of electric fields which may not necessarily be intense enough to cause field emission, but may participate in the emission process mainly by increasing the kinetic energy of charged particles and, thus, influence their escape from the cracks.

The phenomenological model presented above led to the derivation of expressions relating the measured emission yield to the intrinsic strain rate, the rate of crack formation, the duration of the emission burst, and the oxide thickness. An important parameter is the width of the crack, W , since this determines the probability of escape of triboemitted particles from the crack walls. If one assumes that stress relaxation in elastic solids occurs with about the same velocity as that of a propagating crack, especially at the unconstrained oxide-environment interface, then the crack opens to a width W during the emission time t_e , given by

$$W = V_p t_e, \quad (12)$$

where V_p is the rate of crack propagation. The velocity of brittle cracks was derived by Petch³² and found to be

$$V_{p_{\max}} = 0.6 C_2, \quad (13)$$

where C_2 is the shear wave velocity

$$C_2 = (G/\rho^*)^{1/2}, \quad (14)$$

where ρ^* is the density of the elastic medium and G is the shear wave modulus. Since

$$G = \frac{E}{2(1+\nu)} \quad (15)$$

(E is Young's modulus and ν Poisson's ratio), we obtain

$$W = 0.6 \left(\frac{E}{2(1+\nu)\rho^*} \right)^{1/2} t_e. \quad (16)$$

With the appropriate values for Al_2O_3 , namely, $E = 2.1 \times 10^{12} \text{ dyn cm}^{-2}$, $\rho^* = 3.3 \text{ g cm}^{-3}$,³² $\nu = 0.33$, and $t_e \approx 10^{-11} \text{ sec}$, one finds W to be in the order of several hundred \AA which is in reasonable agreement with the value of 1000 \AA required to fit Eq. (11) to the measured thickness dependence of the peak electron emission intensity.

The above discussion was exclusively concerned with electrons. It is conceivable that the observed ion emission may be of thermionic origin as well.

Many metals are known to emit positive ions at temperatures below their melting points. The emitted ions frequently stem from impurities which are not tightly bound to the lattice. Usually, a relatively much larger number of neutrals is emitted simultaneously. We expect a similar emission phenomenon to occur from the oxides investigated here. The "ionic" work function is unknown, but it certainly is appreciably higher than the electron work function. It therefore appears unlikely that at a local temperature in the vicinity of the crack tip of only about 3000°K there will be any measurable emission of oxygen or aluminum ions from Al_2O_3 . The observed ion emission is most likely the result of emission of impurity species; some of these are ionized, and in the case of anodically grown aluminum oxide films, the detected impurities are P, K, B, and Ca. Unfortunately, positive identification of the emitted ions with a mass spectrometer was not possible with the present experimental arrangement. This should be attempted in future work.

Photons are emitted from aluminum and nickel oxides simultaneously with ions and were absent, for example, from titanium oxide which does not emit ions as well. This, then, points to a mechanism of photon emission that is not exclusively blackbody radiation, but is also closely linked to the observed emission of ions. The most likely process appears to be that photons are emitted during relaxation of excited neutrals and ionized impurity species that evaporate from the freshly formed surfaces in the oxide created during crack propagation.

C. Tribostimulated emission from oxides of nickel and titanium

The discussion in Sec. IV B was based solely upon results obtained from dense-oxide films on aluminum. As will be discussed below, it is probable that tribo-stimulated emission from oxide-covered nickel and titanium is also basically of thermionic origin.

The mechanical behavior of NiO films on Ni substrates was not studied as systematically as that for Al_2O_3 on aluminum. The crack morphology and the characteristics of tribostimulated emission from thick ($\approx 2000 \text{ \AA}$) NiO films are very similar to those of Al_2O_3 , and, therefore, similar conclusions may be drawn concerning the mechanical behavior of NiO films on strained Ni substrates. In both cases, the cracks, after about 40% strain, are nearly equispaced and run normal to tensile direction. This observation suggests that both oxides fracture by the same mode, i.e., by cleavage. The higher crack density in NiO and the fact that the peak emission intensity occurs at lower strains in NiO than in Al_2O_3 is evidence that thermally grown NiO films on nickel when deformed in vacuum fracture at lower strains than do anodically grown Al_2O_3 films on aluminum. The rather low emission yield per crack from NiO (see Table II) may be a result of smaller crack openings or be due to intrinsically lower values of W , i , or t_e or a combination of the above.

Another parameter that influences the emission mechanism is Young's modulus of the oxide film. As pointed out by Pugh,²⁸ all ceramic materials fracture

in an essentially brittle manner with various degrees of plasticity. The maximum stress developed at the tip of a crack prior to crack propagation determines the strength of the material and the displacement of the atoms around the crack tip. These stresses are proportional to Young's modulus. The larger the atomic displacement, the higher is the potential energy of the atoms and the greater the amount of strain energy released, part of which may be converted into heat. Since Young's modulus of NiO (8×10^{11} dyn cm⁻²)³³ is of the same order of magnitude as that for alumina, it is conceivable that enough heat is locally generated at a tip of a crack to cause thermionic emission. The broad energy distribution of the negatively charged particles emitted from NiO [Fig. 7(b)] suggests that again some charging may occur on opposite crack walls.

Tribostimulated emission from titanium oxide can also be correlated with the crack morphology and with the mechanical behavior of the oxide on the strained metal substrate. The electron emission as a function of strain (refer to Fig. 10) shows the following:

(1) The electron emission is very weak compared to the emission from dense Al₂O₃ and NiO films of comparable thickness. The peak occurs at strains comparable to those for thick aluminum and nickel oxides.

(2) Emission is only observed in the strain interval from 0 to about 10%.

The above observations suggest that the fracture of relatively thick oxide films on titanium, aluminum, and nickel oxides on the respective substrates occurs by a common mode and that straining the titanium substrate beyond 10% produces very few additional cracks, if any.

Studies of the crack morphology and mechanical behavior of titanium oxide films on strained substrates confirm the above hypothesis. Figure (11) shows that extensive exfoliation of the TiO₂ film had taken place at 38% tensile deformation of the substrate. It is conceivable that exfoliation took place at about 10% strain as suggested by the termination of tribostimulated electron emission at that point.

We conclude that tribostimulated emission from titanium oxide and from oxides of aluminum and nickel occurs by the same mechanism, i.e., field-influenced thermionic emission, despite the fact that no ionic or photon emission was detected from TiO₂. It is quite possible that ions as well as photons were emitted

simultaneously with electrons, but that the emission current was below the sensitivity of the detectors.

- ¹A. Gieroszynski and B. Sujak, *Acta Phys. Pol.* **28**, 311 (1965).
- ²E. Linke, *Z. Angew. Phys.* **29**, 241 (1970).
- ³D. R. Arnott and J. A. Ramsey, *Surf. Sci.* **28**, 1 (1971).
- ⁴B. Sujak and A. Gieroszynski, *Acta Phys. Pol. A* **37**, 733 (1970).
- ⁵B. Rosenblum, Ph.D. thesis (Wayne State University, Detroit, 1976) (unpublished).
- ⁶B. Sujak, A. Gieroszynski, and E. Pega, *Acta Phys. Pol.* **28**, 61 (1965).
- ⁷W. J. Baxter, *Vacuum* **22**, 571 (1972); *Metall. Trans. A* **6**, 749 (1975).
- ⁸K. Becker, *Crit. Rev. Solid State Sci.* **3**, 39 (1972).
- ⁹T. F. Gesell, E. F. Arakawa, and T. A. Callcott, *Surf. Sci.* **20**, 174 (1970).
- ¹⁰B. Rosenblum, J. P. Carrico, P. Bräunlich, and L. Himmel, *J. Phys. E* (to be published).
- ¹¹S. Tajima, *Advances in Corrosion Science and Technology* (Plenum, New York, 1970), Vol. 1.
- ¹²M. J. Graham, G. I. Sproule, D. Caplan, and M. Cohen, *J. Electrochem. Soc.* **119**, 883 (1972).
- ¹³A. Aladjem, *J. Mater. Sci.* **8**, 688 (1973).
- ¹⁴G. J. Tibol, *J. Electrochem. Soc.* **111**, 1368 (1964).
- ¹⁵D. A. Vermilyea, *J. Electrochem. Soc.* **110**, 345 (1963).
- ¹⁶J. C. Grosskreutz, *Surf. Sci.* **8**, 173 (1967).
- ¹⁷A. J. Dekker, *Solid State Physics* (Prentice-Hall, Englewood Cliffs, 1957).
- ¹⁸V. S. Kortov, R. I. Mints, I. E. Myasnikov, and A. Y. Gaprindoshvili, *Phys. Status. Solidi. A* **3**, K13 (1970).
- ¹⁹Rockwell Int. Report No. SC 573.2 IR (unpublished).
- ²⁰D. C. Duglass, *Oxid. Met. Alloys* **1**, 137 (1971).
- ²¹C. Edeleanu and T. J. Law, *Philos. Mag.* **1**, 573 (1962); A. S. Durelli and S. Okubo, *Proc. Soc. Exp. Stress Anal.* **11**, 153 (1954).
- ²²S. C. Grosskreutz and M. B. McNeil, *J. Appl. Phys.* **40**, 355 (1969).
- ²³S. C. Grosskreutz, *J. Electrochem. Soc.* **116**, 1132 (1969).
- ²⁴P. A. Thiessen, E. Franke, and W. Stegling, *Monatsber. Dtsch. Akad. Wiss. Berlin* **1**, 365 (1965).
- ²⁵N. J. Petch, *Fracture* **1**, 351 (1968).
- ²⁶JANAF *Thermochemical Tables* 2nd ed. (National Bureau of Standards publication No. 37) (U.S. GPO, Washington, D.C., 1971).
- ²⁷E. K. Beauchamp, Sandia Lab Rep. SC-DR 720819, 1972 (unpublished).
- ²⁸S. F. Pugh, *Br. J. Appl. Phys.* **18**, 129 (1967).
- ²⁹C. E. Inglis, *Trans. Inst. Nav. Archit.* **55**, 219 (1931).
- ³⁰F. A. McClintock and A. S. Argon, *Mechanical Behavior of Materials* (Addison-Wesley, Reading, Mass., 1966), p. 489.
- ³¹P. S. H. Henry, *Br. J. Appl. Phys.* **2**, 31 (1953).
- ³²L. P. Smith, in *Handbook of Physics* 2nd ed., edited by E. W. Condon and Hugh Odishaw (McGraw-Hill, New York, 1967), p. 8-76.
- ³³P. V. DuPlessis, S. S. Fonder, and L. Alberts, *J. Phys. C* **4**, 1983 (1974).

ATTACHMENT C

CHARACTERIZATION OF ANODIC OXIDE COATINGS ON
ALUMINUM BY TRIBOSTIMULATED EXOEMISSION

by

D. L. Doering, T. Oda,* J. T. Dickinson, and P. Bräunlich
Department of Physics
Washington State University
Pullman, WA 99163

* Permanent Address: College of Education, Oita University,
Oita City, Japan 870-11

1. INTRODUCTION

Tribostimulated exoemission is a term which refers to the emission of electrons, ions, photons or neutral particles during the mechanical deformation of a material. This effect has been shown for oxide layers on metals such as Al, Ti, Mg and Ni ⁽¹⁻¹⁰⁾. Although the mechanism of exoemission is not clearly understood, it has been established that the emission is closely associated with the propagation of cracks in the oxide ⁽¹⁻¹⁰⁾. This implies that exoemission may be useful in discriminating between variations in the oxide, since crack propagation is strongly dependant on the oxide properties.

Recently, we have shown examples of characteristic exoemission during tensile deformation from anodic oxide coated aluminum alloys ⁽³⁾. The rate of negative charged particle emission vs. strain at a constant rate is defined as the characteristic exoemission curve or CEC. The CEC, as we shall see, is very sensitive to oxide thickness and structure. For a variety of examples of CECs, the reader is referred to references 1-3.

In this paper, we extend our investigation to a carefully controlled variation of parameters affecting oxide formation, studies of the effect of oxide age (time between anodization and testing), and the sealing of porous oxides in boiling water. A number of the anodization parameter variations were chosen to bracket values used in the preparation of aluminum surfaces for adhesive bonding. We suggest that exoemission could provide a means of detecting deviations from a desirable anodic oxide layer, perhaps due to improper pretreatment, anodization, or post anodization treatment. We, also, concentrate our attention on aluminum clad Al 2024 (T3 annealed) samples due to its wide range of commercial uses.

2. EXPERIMENTAL STUDIES

2.1 Apparatus

For the detection of exoemission, a high vacuum system equipped with a fully instrumented tensile straining device and a single event channeltron electron multiplier (CEM) for the detection of negatively charged particles was used. The CEM used was essentially noise free, exhibiting a background count rate of less than 2 counts per minute.

The use of high vacuum allowed a high rate of sample testing and the comparison of similar samples tested in both HV (1.4×10^{-4} Pa) and UHV (1.4×10^{-7} Pa) showed no significant difference in the CEC. To aid in the characterization of the oxides, an optical microscope and a high resolution scanning electron microscope (SEM) were used. To complete the facilities, an electrolytic cell was set up to anodically grow the oxide layers under well controlled conditions.

2.2 Data Acquisition and Treatment

Although the details of the acquisition and treatment of data that we use have already been reported ⁽³⁾, it would be worthwhile to highlight a few of the major items of interest here.

For each sample, the most important information obtained during elongation is the stress-strain curve, the characteristic exoemission curve (CEC) and the total emission. To generate the CEC, the pulses from the electron multiplier are amplified and then either integrated with a count rate meter or stored in a multichannel scaler which accumulates counts for 0.8 sec per channel. The rate meter output is recorded on a strip chart recorder to give the count rate vs. time. The multichannel scaler provides

a digital output which may later be treated by statistical methods.

The following parameters of the emission seem to be the most sensitive to variations in the oxide layer:

1. Total Emission. This indicates the total amount of negative charged particle emission observed from the beginning of strain until sample rupture.
2. Onset of Emission. After some particular minimum strain, the sample begins exoemission. The onset is given in percent strain.
3. Peak Height(s), Position(s) and Width(s). Many samples emit with more than one peak and all are considered potentially important. Most samples show a major peak following the onset (see ref. 3).

2.3 Samples and Sample Preparation

In order to produce a uniform stress distribution, the aluminum clad Al 2024 samples were machined into a traditional dogbone shape from 20 mil (0.013 cm) thick production stock. A slow milling process was used to avoid unnecessary stresses and temperature increases. Just prior to anodization, the samples were cleaned and then acid etched to provide a fresh aluminum surface for the oxide to grow evenly.

For anodization, the sample is placed in an electrolyting cell as the anode and voltage is applied to cause the conduction of oxygen ions toward it. Because aluminum oxide is an insulator, the process slows as the layer becomes thicker. If this were the only reaction occurring, the oxide would grow indefinitely with the square root of time. However, most electrolytes are acidic solutions which act to etch the oxide as it is forming. This slows the growth to a nearly linear relation with time initially. Later, it forces the oxide to come to an equilibrium thickness which is dependant on the voltage applied. This voltage can be continually increased up to

the breakdown voltage of the electrolyte.

For our studies, three electrolytes were used. The first solution was one of 0.05 M ammonium tartrate (later abbreviated AT). The solution is weakly acidic, thus, the resultant oxide is very dense (barrier type). In general, higher voltages are required to produce a given thickness of an oxide of this type. Second, solutions of phosphoric acid (H_3PO_4) were used. The rapid etching of the acid leaves a very porous (duplex) oxide. When viewed on edge with the SEM, one observes numerous vertical pores which traverse the majority of the thickness. In order to study the effect of sealing the oxide pores in boiling water, a third solution of sulphuric acid was chosen because the sealing of sulphuric acid prepared oxides has been studied in detail ⁽¹¹⁾ and provides us with a basis for comparison.

The oxides studied here were prepared with the conditions and variations given in Table I.

The most obvious changes due to variations of the anodization parameters were observed to be the thickness and the porosity. The latter being seen by changes in the pore diameter and profile. As seen with the SEM, changes in porosity are revealed by variation in surface texture and roughness of the crack wall (see Fig. 3). Optical microscopy also revealed changes in the crack patterns.

Following anodization, the samples were stored in a desiccator for at least a week (except sets g and h) to avoid the effects of aging, discussed in section 2.4.5. Also, we have found that samples rinsed in reagent grade acetone yielded more reproducible results as well as twice the exoemission when compared to unrinsed samples. This implies a dependence of the exoemission process on the surface condition, an effect we are further investigating. For the sake of consistency, the acetone rinse was used on all

samples before mounting in the vacuum system. The samples were tested at a pressure of 1 to 5×10^{-4} Pa (less than 15 minute pump-down time). The sample was pulled until rupture with a constant strain rate of $0.104 \text{ \% sec}^{-1}$.

2.4 Results

2.4.1 Effect of Oxide Thickness on Exoemission - Ammonium Tartrate Anodization

Samples were prepared with the standard ammonium tartrate solution to thicknesses ranging from 500 \AA to 4000 \AA . A graph of the total emission as a function of thickness (Fig. 1) reveals that the emission rises rapidly for lower thicknesses, levels off for intermediate values and then rises exponentially for larger thicknesses. Although the reason for this shape is not known, several models are being considered and further tests should distinguish between them. The onset of emission is also found to vary, decreasing monotonically with increasing thickness. It is interesting to correlate the onset with the total emission by plotting the two parameters together. Figure 2, curve a, shows the result which is interestingly a straight line. Discussion of this will be resumed later.

2.4.2 Effect of Oxide Thickness on Exoemission - H_3PO_4 Anodization

To vary the thickness for porous oxides, two methods were employed. The first takes advantage of the linear portion of the growth curve. Thickness can be varied by stopping the anodization at different times. Figure 3a shows an SEM photograph at $20,000 \times$ for such an oxide stopped at 600 sec, resulting in a 5500 \AA oxide layer. The second method allows the oxide enough time to come to equilibrium between the growth and the

etching. Thickness is, in this case, varied by changing the applied voltage. Such an oxide layer is shown in Fig. 3b for an anodization voltage of 15 volts, resulting in a 6400 Å film. The oxide formed by this second method has a more open pore structure which is best seen by examining the roughness of the crack wall.

When thickness is varied by the anodization time, the total counts vs. thickness curve (Fig. 4) reveals two distinct regions. For low thicknesses, the emission is very weak and almost linear with thickness. At approximately 2000 Å, a sudden change occurs. The emission is much stronger and the rise becomes exponential, similar to the dense oxide. Optical micrographs of these oxides show that the thin oxides have short closely spaced cracks that appear to be confined to grains in the substrate. Above 2000 Å, cracks become longer, more widely spaced and tend to be transverse to the direction of strain. It should also be noted that the onset of crack formation of the thin oxides is considerably later than for thick oxides. These features indicate different modes of crack propagation for the two regimes, substantially influencing exoemission.

For samples where the thickness was varied by changes in the anodization voltage, the total counts vs. thickness curve shows only the strong exponential dependence (see Fig. 5), similar to the thick anodization-time varied samples. This is because the minimum thickness obtained with this anodization method was greater than 2000 Å, so that the thinner oxide emission mode was not observed. It is interesting to note that for a given thickness, the emission for a voltage-varied sample is less than that of a time-varied one by a factor of approximately ten. Presumably, this can be explained by the fact that the pores are larger in the voltage varied samples. This would reduce the amount of oxide which is actually cracked and thus reduce emission.

In Figure 2, curves b and c, we have again correlated the onset of

emission with total emission. Similar to the dense oxide, we again see a linear relationship, except for the case of high emission where a minimum value of onset is reached. Differences in the slope and position of these curves reflect the differences in the porosity of the two sets of samples.

At this point, the value of the graph of onset of emission vs. total emission becomes apparent. Conceivably, a family of curves could be produced where each curve represents the dependence of onset and total emission on thickness for a given porosity. This would allow one to rapidly determine an approximate value for the thickness and the relative porosity of a sample from its CEC.

2.4.3 Effect of Electrolyte Concentration on Exoemission

By increasing the concentration of our H_3PO_4 solution, we expect a two fold effect. The conductivity of the electrolyte should increase, allowing us to grow a thicker oxide. However, the activity of the acid will increase and tend to etch more open pores. Comparing the SEM photos for an 8% (Fig. 3c) and a 12% (Fig. 3d) concentration samples, we can see both of these effects occurring. Figure 6 shows that for both sets of samples tested (the 30 V samples are roughly three times the thickness of in 10 V set) the emission is found to decrease with increases in concentration. This implies that for the range of concentration chosen the changes in porosity have the dominant effect. However, it should be noted that for some value of concentration lower than 8% the emission must achieve a maximum, since for zero concentration (pure H_2O), we obtain no emission.

To be consistent with our assumptions about the effects of porosity and thickness on a plot on onset vs. total counts, we would expect that such a plot for our concentration-varied samples would have a positive

slope with the highest value of concentration at the low emission end. Figure 2, curve d, gives an example of this for the 10 V set.

2.4.4 Effect of Electrolyte Temperature on Exoemission

As the temperature of an acid is increased, its activity is known to increase rapidly. In the case of our electrolyte, this will promote an increasing amount of oxide porosity. In addition, the number of oxygen ions and their mobility will also increase with higher temperature. Thus, we again have competing processes. With all other parameters held constant, we see in Figure 7 a plot of total counts vs. temperature. For low temperatures little emission occurs. SEM photos of these oxides show a very thin, nearly dense layer. The thickness is then seen to rise rapidly to a peak value which corresponds to the maximum in the total emission. Above this point, the porosity is seen to undergo the most dramatic changes and the thickness is reduced slightly. This can be seen in Figures 3e and 3f, which show oxides grown at 19.5 C and 29.5 C. The increases in porosity again are the dominating effect causing the reduction of total emission above 19 C.

2.4.5 Effect of Oxide Age on Exoemission

It is known that freshly formed anodic oxide coatings on aluminum and its alloys change their mechanical properties during a time lasting up to several days. The oxide is thought to change from a relatively soft to a stabilized brittle coating. Since the mechanical properties strongly affect the formation of cracks, we expect to observe changes in the CEC as a function of oxide age. To test this, two sets of samples were prepared. On the first set, a 2000 Å dense oxide was grown. The

second set was prepared in 10% H_3PO_4 at 30 V for 10 minutes (approx. a 6000 Å porous oxide). Both sets were known to emit well, so changes in the CEC would be easily noticed.

Figures 8a and 9 show that for both sets the emission rises rapidly with increasing age to a stable value. At the same time, the onset of emission decreases to a stable value with increasing age. Figure 8b shows this for the dense oxide. This is consistent with the idea that the oxide is becoming more brittle. We can also see from Figures 8 and 9 that the density of cracks does not significantly vary with age. Thus, the increase in emission cannot be explained by changes in the number of cracks. For both sets of samples the emission appears to level off after about 100 hours. However, this does not necessarily imply that this time is universal for all oxide layers.

By plotting the onset of emission vs. total counts (Fig. 2, curves g and h), we again find linear relationships for both sets. In fact, there is a high degree of correspondence between these curves and those of the sets of samples where the thickness was varied. This would tend to indicate that there is a layering effect in the oxide. A brittle layer, presumably at the surface, is most likely responsible for exoemission. A softer layer below it would still be able to affect the crack density but the energy released would not be sufficient for exoemission. The growth of this brittle layer with time would seem indicative of a dehydration taking place in the oxide. This type of exponentially decreasing growth rate is found to lead to the curves shown in Figures 8 and 9. This model would also indicate that the similarity in the age at which the emission levels off for the two sets is not universal but varies with thickness.

2.4.6 Effect of Sealing the Oxide Pores

Al_2O_3 is thermodynamically unstable at elevated temperatures in the presence of water. Thus immersion of porous oxides in boiling water produces profound changes in its structure and chemical composition (11). We have investigated the effects of this sealing procedure on the CEC of porous oxides anodized in a sulphuric acid solution.

For details of the reactions that occur during the sealing process, the reader is referred to reference 11. However, a brief description here would be enlightening as well.

Boiling water is found to readily dissolve Al_2O_3 to form aluminum hydroxide ($\text{Al}(\text{H}_2\text{O})_6^{3+}$). In this process, SO_4^- ions* become mobilized in the liquid/solid interface inside the pores. This facilitates the precipitation of a gel composed of aqua-hydroxo complexes ($\text{H}_2\text{OAl}(\text{OH})^{2+}$) as soon as the pH value has been lowered to a critical value. This quickly fills the pores and reduces the pore volume in the first two minutes of sealing. Afterwards, the reaction rate is controlled by H_2O diffusion into and SO_4^- diffusion out of the film. Gradual polymerization of the aqua-hydroxo gel also occurs to form pseudo-boehmite and boehmite. The reaction rates are reflected in a rapid weight gain in the first two minutes which slows by a factor of five in the next five to eight minutes. The lowest average value reached is about 1/40th of the initial rate after 10 minutes of sealing.

To study exoemission from these samples, they were all aged for one week. The precipitates in the pores are known to contain large amounts of water and sulfate radicals which are released during the aging process. The end products are aluminum trioxides which may be responsible for the change in the surface texture observed with the SEM.

*the sulphate concentration in these anodic oxide films reaches 14% (11)

In Figure 10, we see the total emission as a function of sealing time for three different anodizing times. Initially, a large drop is seen with increased sealing. In spite of the week of aging of the samples, the abundance of water in the oxide is still presumed to be quite high. Thus, the drop in emission may be directly related to the rapid weight gain that occurs for low sealing times. Once this reaction rate slows, the exoemission is seen to level off. With increased sealing times beyond 400 minutes, the emission is again seen to rise. This can be interpreted as resulting from the crystalization of the precipitates which were formed during the reaction. This would allow the oxide to become slightly more brittle and thus facilitate exoemission.

3. CONCLUSION

The results of this study indicate that exoemission is, as expected, strongly dependant on the preparation of the oxide. This may eventually lead to the use of this technique as a quantitative measure of the commercial quality of an oxide. This would be especially valuable in the case of adhesive bonding where the control of the oxidation process is critical to the strength of the bond. The data parameters that appear to be most useful for this purpose are the total emission and the onset of emission. In many cases, the thickness and relative porosity can be approximated from the CEC by the use of a graph such as is shown in Figure 2. However, for thick porous oxides, the ambiguity resulting from the minimum value of emission onset may require a more critical evaluation of the other data parameters revealed in the CEC.

It is clear from our results here and from earlier work that the propagation of cracks is necessary for emission. It seems reasonable that the breaking of molecular bonds at the crack tip is the source of the energy for particle emission. Thus, an increase in the total number of bonds

should cause an increase in emission. Since the crack density is seen to be constant with thickness for films greater than 2000 Å, we can say that the number of broken bonds is proportional to thickness. Observations of Figures 1, 4 and 5 show that the total emission is, indeed, rising with thickness. The fact that this dependence takes on an exponential form provides at least one important key toward the isolation of the mechanism for exoemission. We can say from this that the total amount of energy released is not the rate limiting factor for the emission. If it were, one would expect to see a linear relationship between emission and thickness. Our evidence here also does not behave as though the electrons are limited by a maximum escape depth which would limit the amount of detectable emission originating from deep within the crack.⁽²⁾ This would imply that either most of the negative charged particle emission originates at or near the surface or the mechanism is such that emission from deep within the crack is directed toward escape from the crack. However, it is obvious that further experimentation is needed in order to resolve the actual mechanism or mechanisms involved.

4. ACKNOWLEDGMENTS

We gratefully acknowledge support for this work from the Air Force Office of Scientific Research, Contract No. F49620-77-C-0042 and the Boeing Commercial Airplane Company. We thank the Bendix Corporation for transfer of equipment to Washington State University. The authors also wish to thank L. A. Larson, D. Snyder, and K. Voss for their assistance in the laboratory.

REFERENCES

1. B. Z. Rosenblum, J. P. Carrico, P. Bräunlich, and L. Himmel, J. Phys. E., Sci. Instrum. 10 (1977).
2. B. Z. Rosenblum, P. Bräunlich, and L. Himmel, J. Appl. Phys. 48, 5262 (1977).
3. J. T. Dickinson, P. F. Bräunlich, L. Larson, and A. Marceau, Appl. of Surf. Sci. 1 (1978).
4. D. R. Arnott and J. A. Ramsey, Surf. Sci. 28, 1 (1971)
5. E. Linke, Z. Angew. Physik 29, 241 (1970).
6. B. Sujak and A. Gieroszynski, Acta Phys. Pol. 28, 311 (1965)
7. B. Sujak, A. Gieroszynski, and E. Pega, Acta Phys. Pol., 28, 61 (1965).
8. W. J. Baxter, Vacuum 22, 571 (1972).
9. T. F. Gesell, E. F. Arakawa, and T. A. Callcott, Surf. Sci. 20, 174 (1970).
10. B. Sujak and A. Gieroszynski, Acta. Phys. Pol. A37, 733 (1970).
11. K. Wefers, Aluminum 49, 553 (1973).

FIGURE CAPTIONS

1. Total exoemission as a function of thickness for dense oxides.
2. Correlation of emission onset (in percent strain) and total emission for several sample sets. The letters correspond to the descriptions in Table I.
3. SEM photos of porous oxides with various preparations. Descriptions are given in the text.
4. Total Emission vs. Thickness for a time-varied porous oxide.
5. Total Emission vs. Thickness for a voltage-varied porous oxide.
6. Total Emission vs. Electrolyte Concentration for two porous oxides. The upper curve was grown at 30V, the lower curve at 10V. This results in a considerably thicker oxide for the 30V samples.
7. Total Emission vs. Temperature for a porous oxide.
8. a. Total Emission and Crack Density plotted vs. Oxide Age (time between anodization and measurement of exoemission) for a 2000 Å dense oxide.
b. Onset of Emission vs. Oxide Age for a dense oxide.
9. Total Emission and Crack Density vs. Oxide Age for a 6000 Å porous oxide.
10. Total Emission vs. Sealing Time (time in boiling water) for H_2SO_4 prepared porous oxides.

TABLE CAPTION

- I. Summary of sample preparations, parameters varied and changes in oxides observed.

TABLE I

Set	Electrolyte and Conditions	Parameter Varied	Major Change in Oxide	Comments
ANODIZATION				
a	Ammonium Tartrate, 0.05 M, at 21°C and 30 min. after anodization voltage is reduced	Anodization Voltage	Thickness	The thickness of the dense oxide was varied between 500 Å and 4000 Å.
b	H ₃ PO ₄ , 9.3%* at 30 V and 21°C	Anodization Time	Thickness	For times between 0 and 500 seconds, oxide thickness is proportional to time.
c	H ₃ PO ₄ , 10%* at 21°C for 20 minutes	Anodization Voltage	Thickness	20 minutes assures that equilibrium between growth and dissolution is reached. Thickness then increases with voltage.
d	H ₃ PO ₄ , 10 V, 21°C for 20 minutes	Electrolyte Concentration*, 8%, 9%, 10%, and 12%	Thickness, Pore Structure	Increasing concentration causes a slight increase in thickness and a more open pore structure.
e	H ₃ PO ₄ , 30 V, 21°C for 20 minutes	Electrolyte Concentration*, 8%, 9%, 10%, and 12%	Thickness, Pore Structure	Same as d, but oxide thickness is greater.
f	H ₃ PO ₄ , 10%*, 10 V for 20 minutes	Temperature 5°C, 10°C, 11.5°C, 19.5°C, 23°C, 25.5°C, and 29.5°C	Thickness and Pore Structure	As the temperature increases, the ion mobility increases while the acid activity increases. This produces variation in both the thickness and pore structure.

Table 1 (cont.)

POST-TREATMENT

		Time between anodization and testing (aging time), between 15 min. (pumpdown time) to 160 hours	Dehydration of the Oxide	The oxide appears to become more brittle with aging.
g	Ammonium Tartrate, 0.05 M, 21°C, 140 V, 30 min. after anodization voltage is reduced			
h	H ₂ PO ₄ , 10%*, 30 V, 10 min.	Aging time between 15 min. to 160 hours.	Dehydration of the Oxide	See g.
i	H ₂ SO ₄ , 20%*, 14 V, anodization times of 1.5, 3 and 5 min. (to vary thickness)	Sealing. Samples sealed in boiling water for times ranging from 0-800 min.	Pore Structure	Increase in oxide weight, pores fill with hydrated oxide, reducing surface area.

* by weight

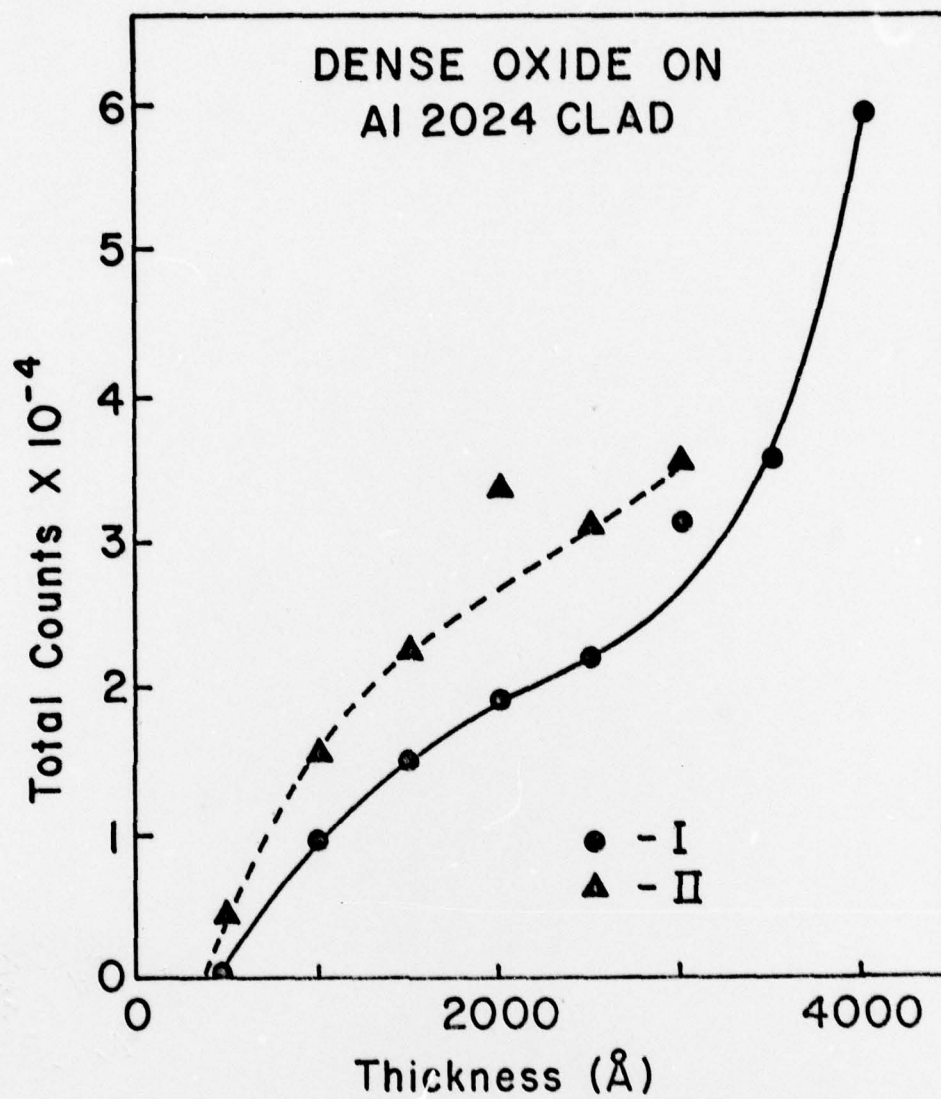


Fig. 1

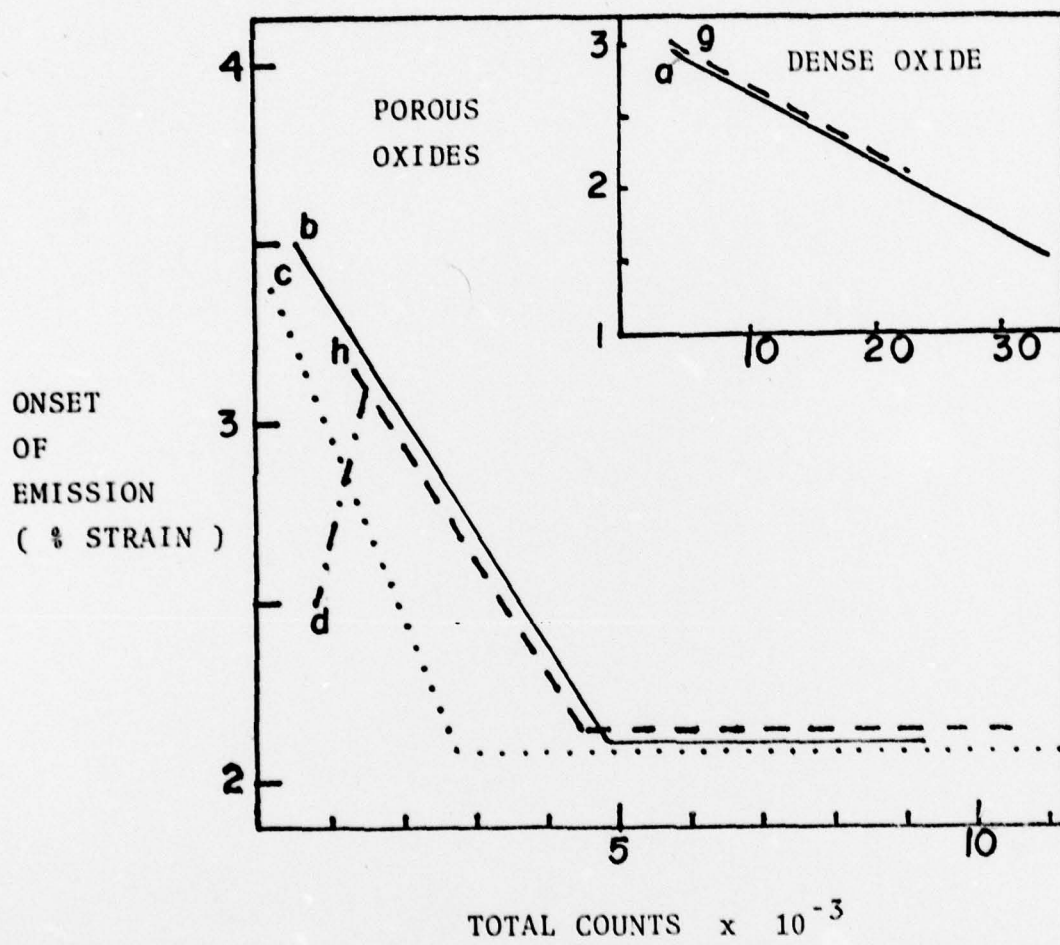


Figure 2

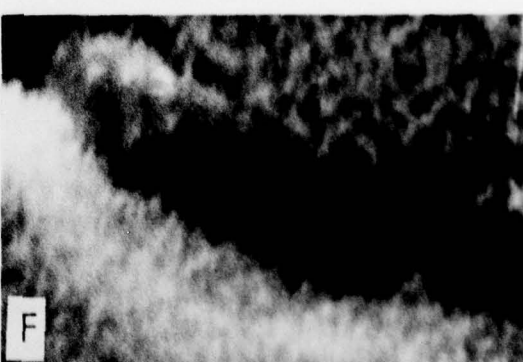
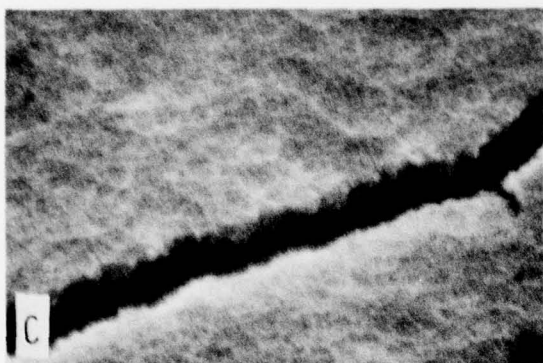
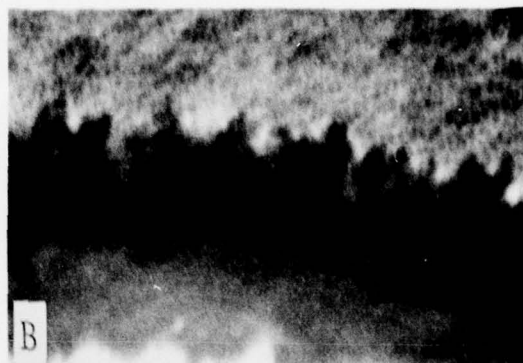
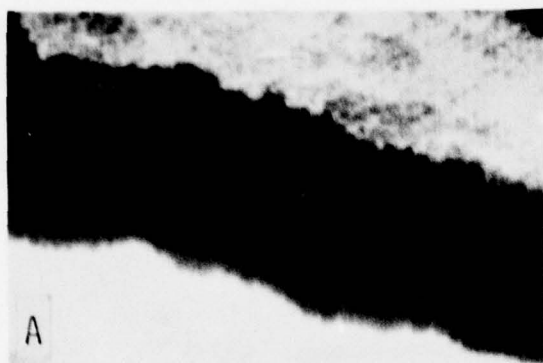


Fig. 3

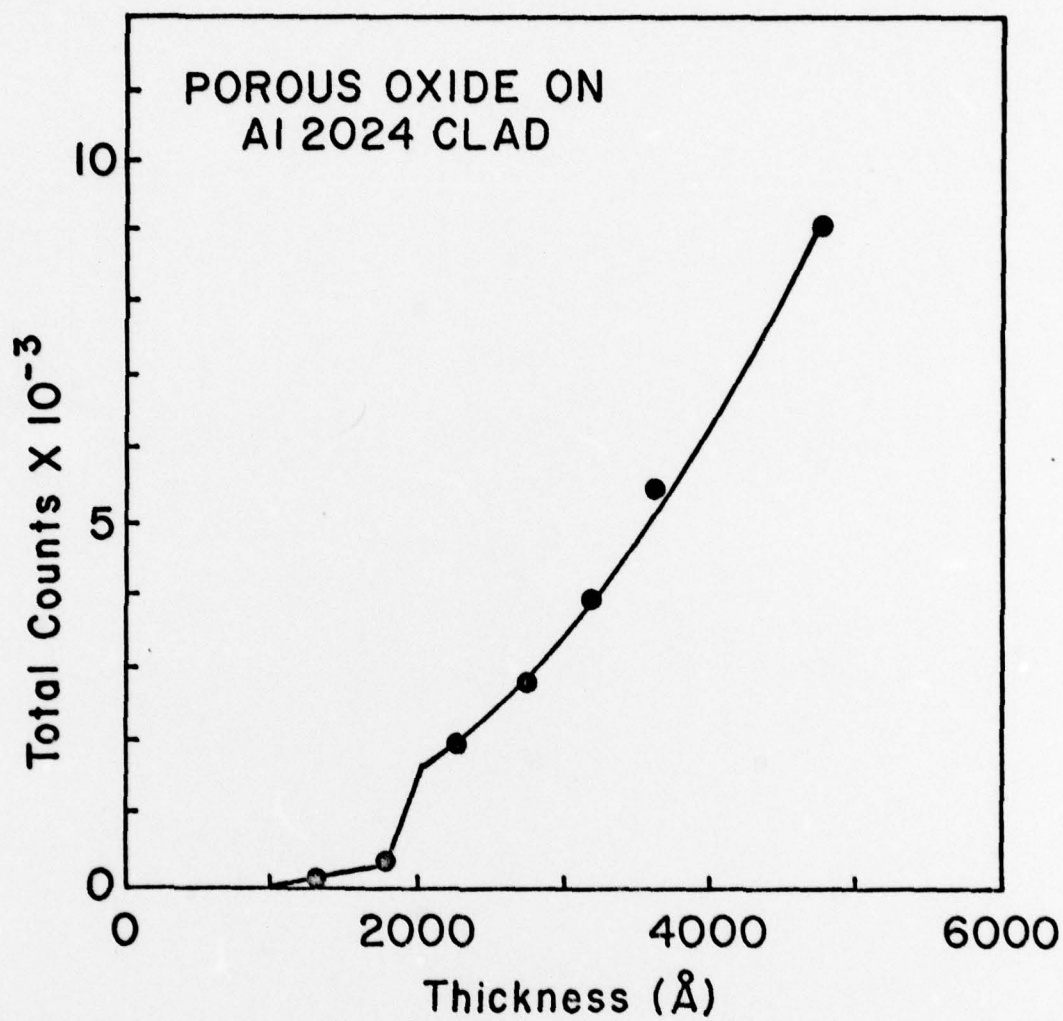


Fig. 4

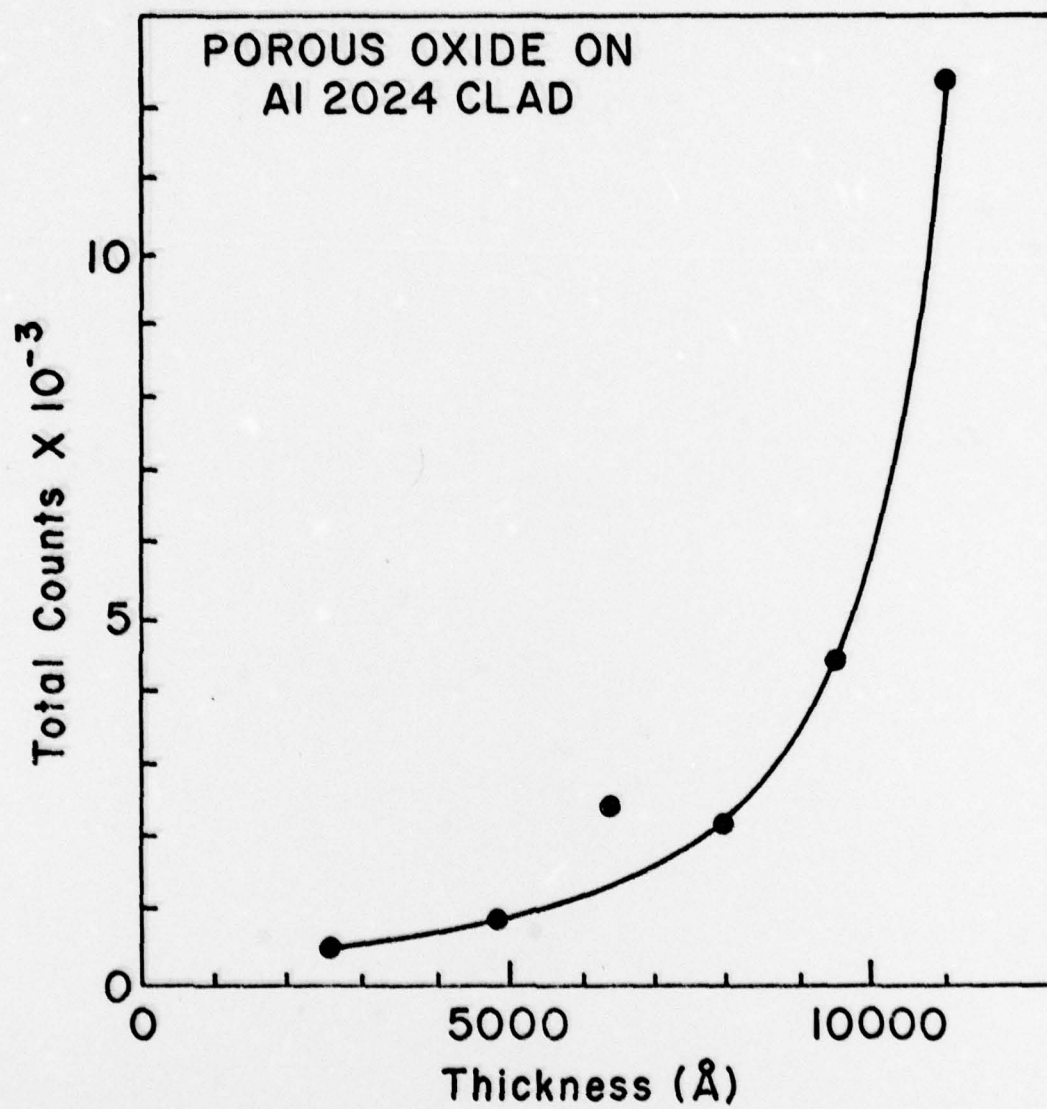


Fig. 5

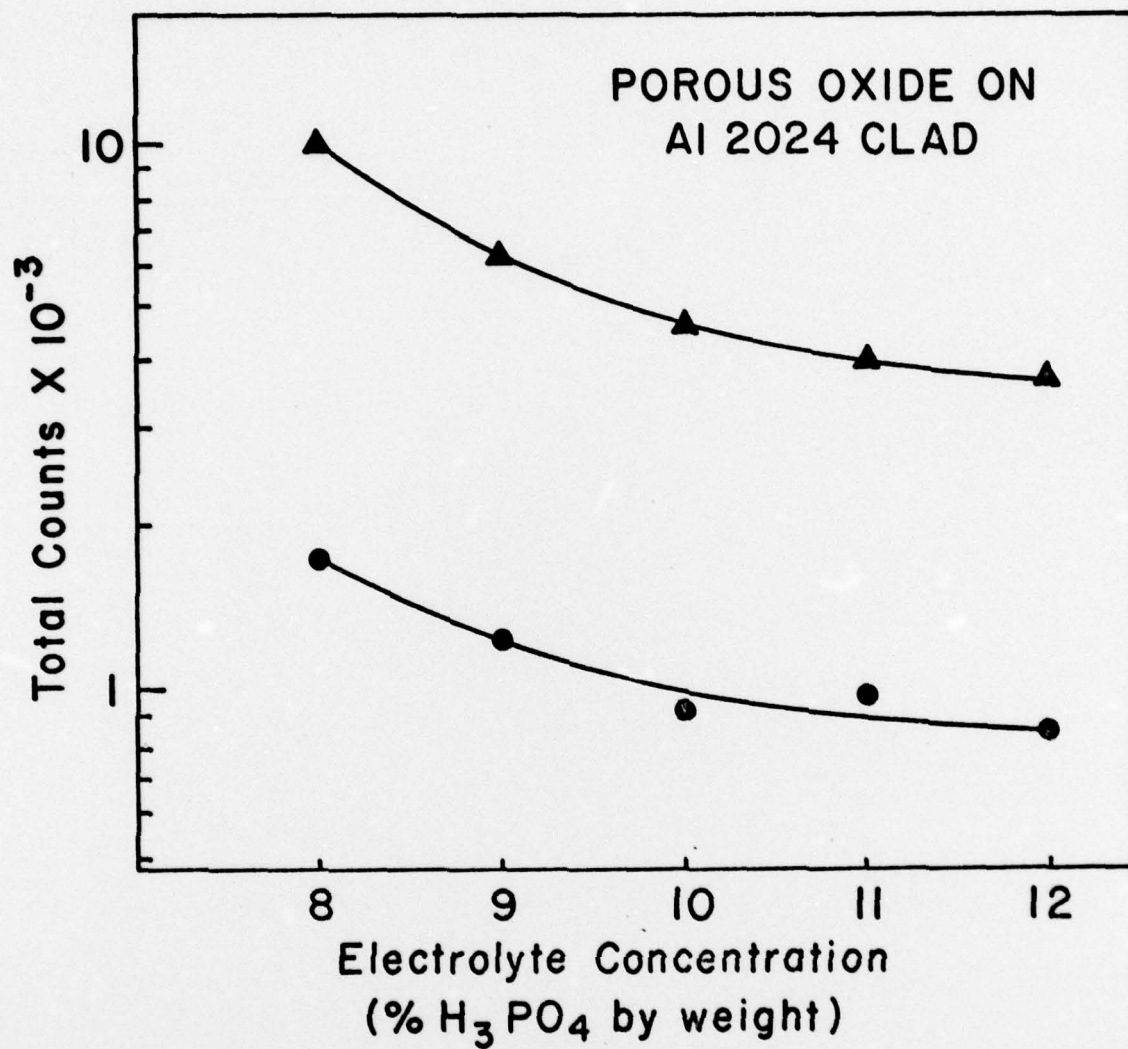


Fig. 6

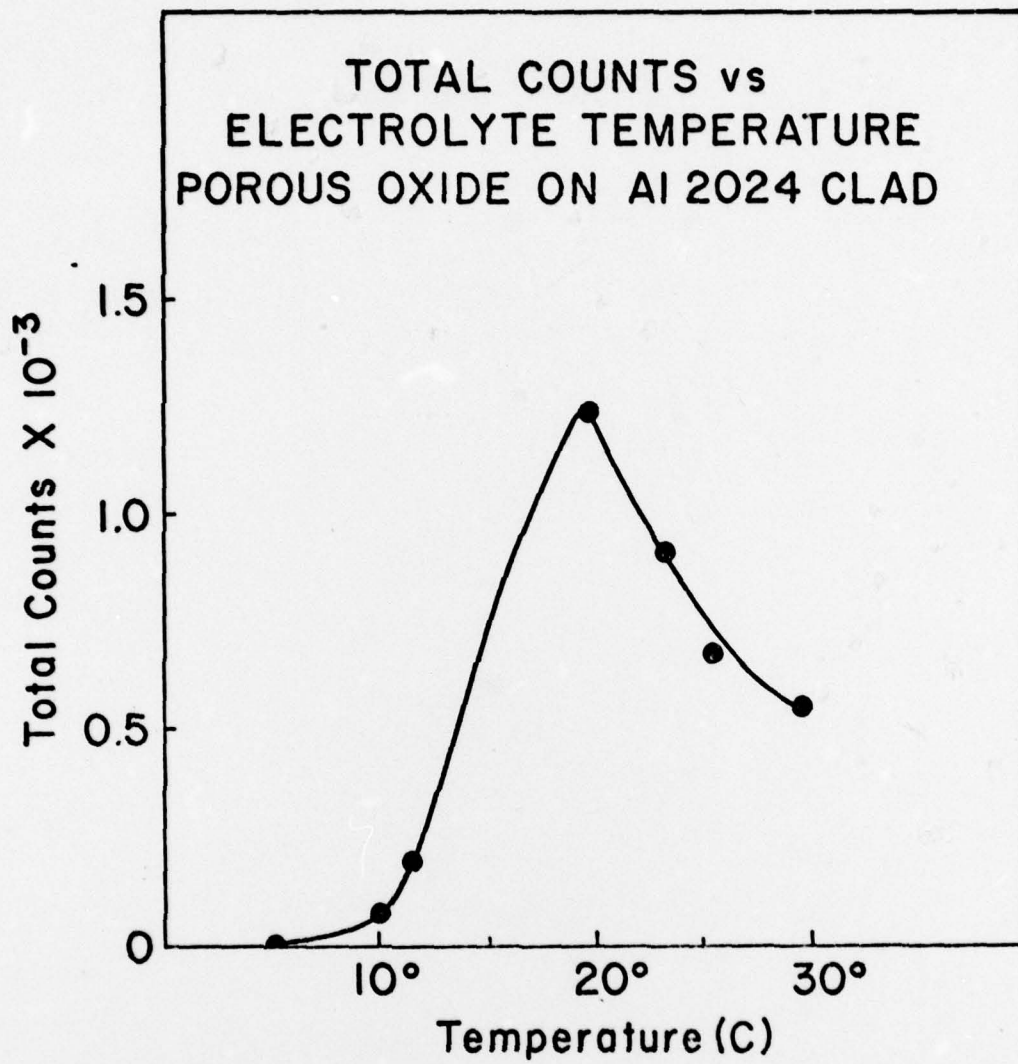


Fig. 7

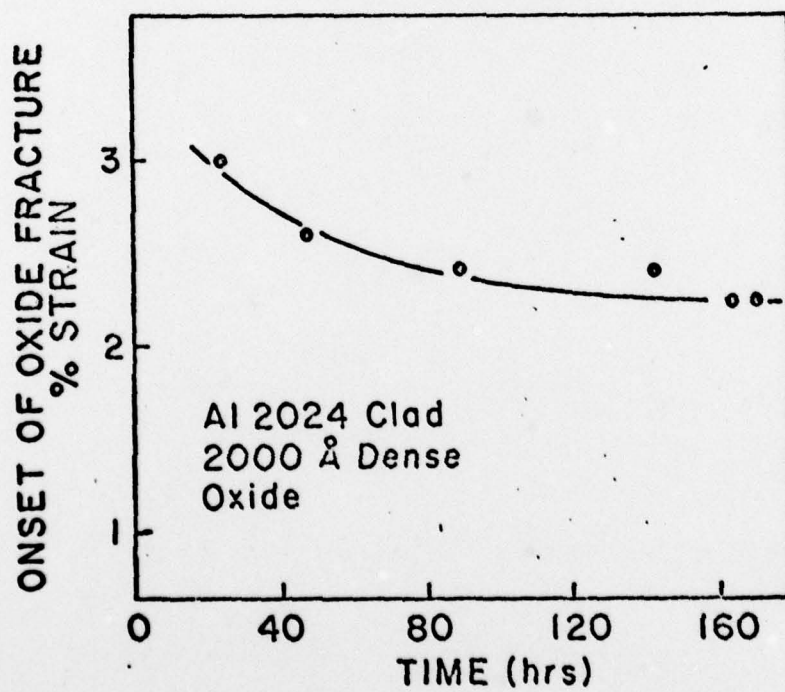
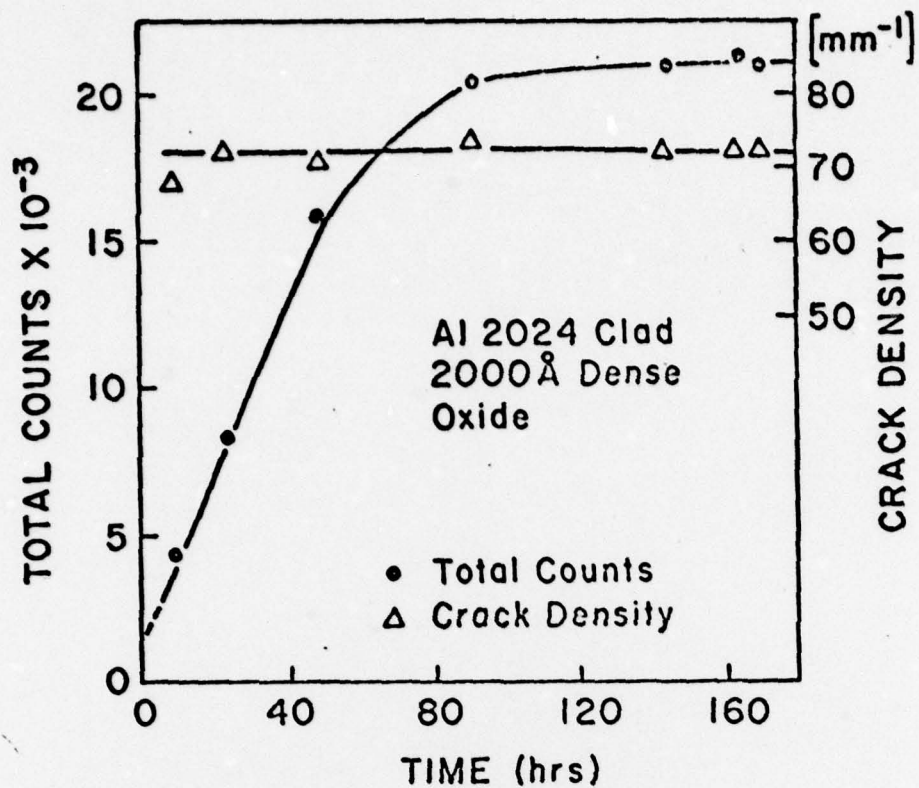


Fig. 8

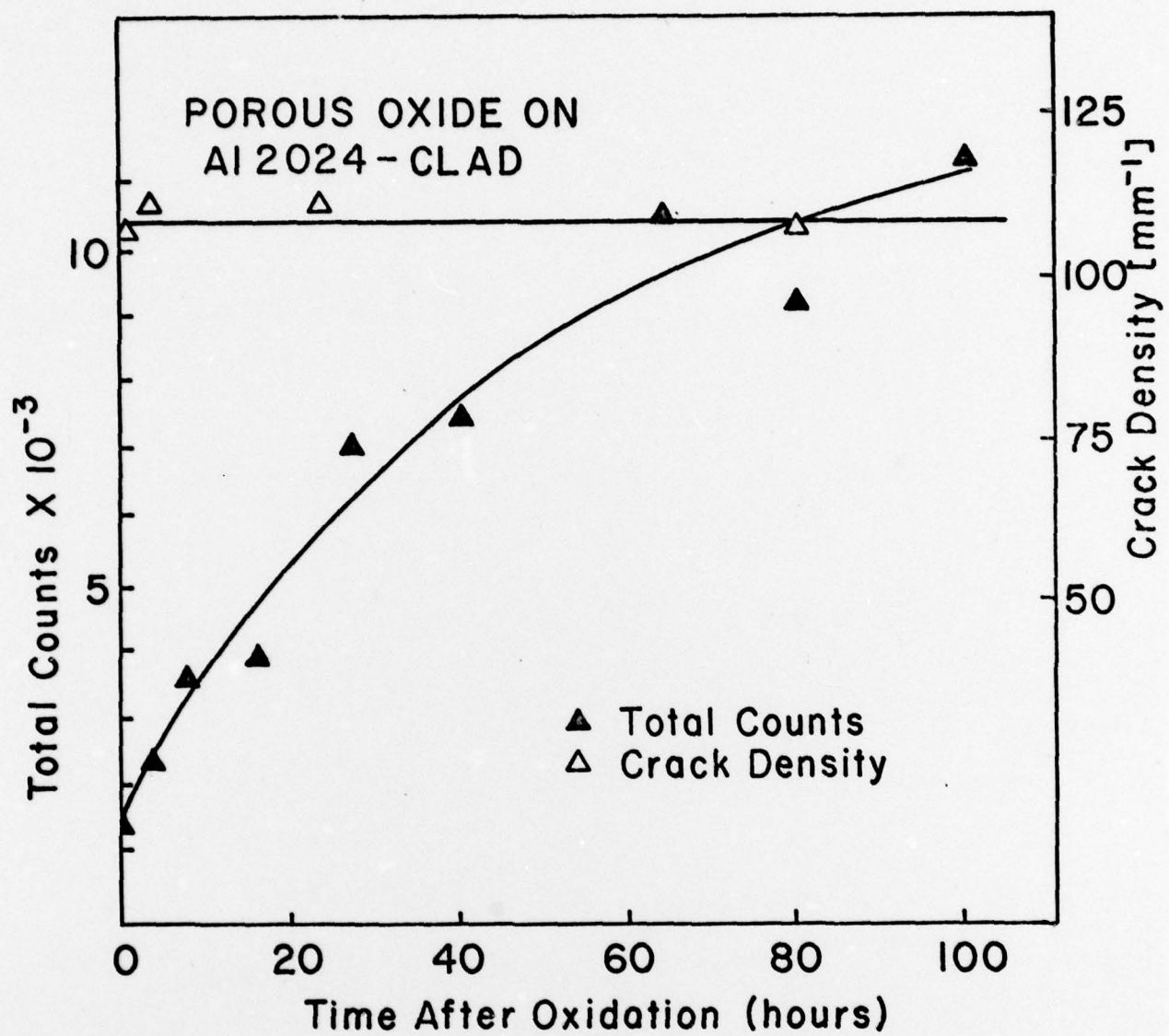


Fig. 9

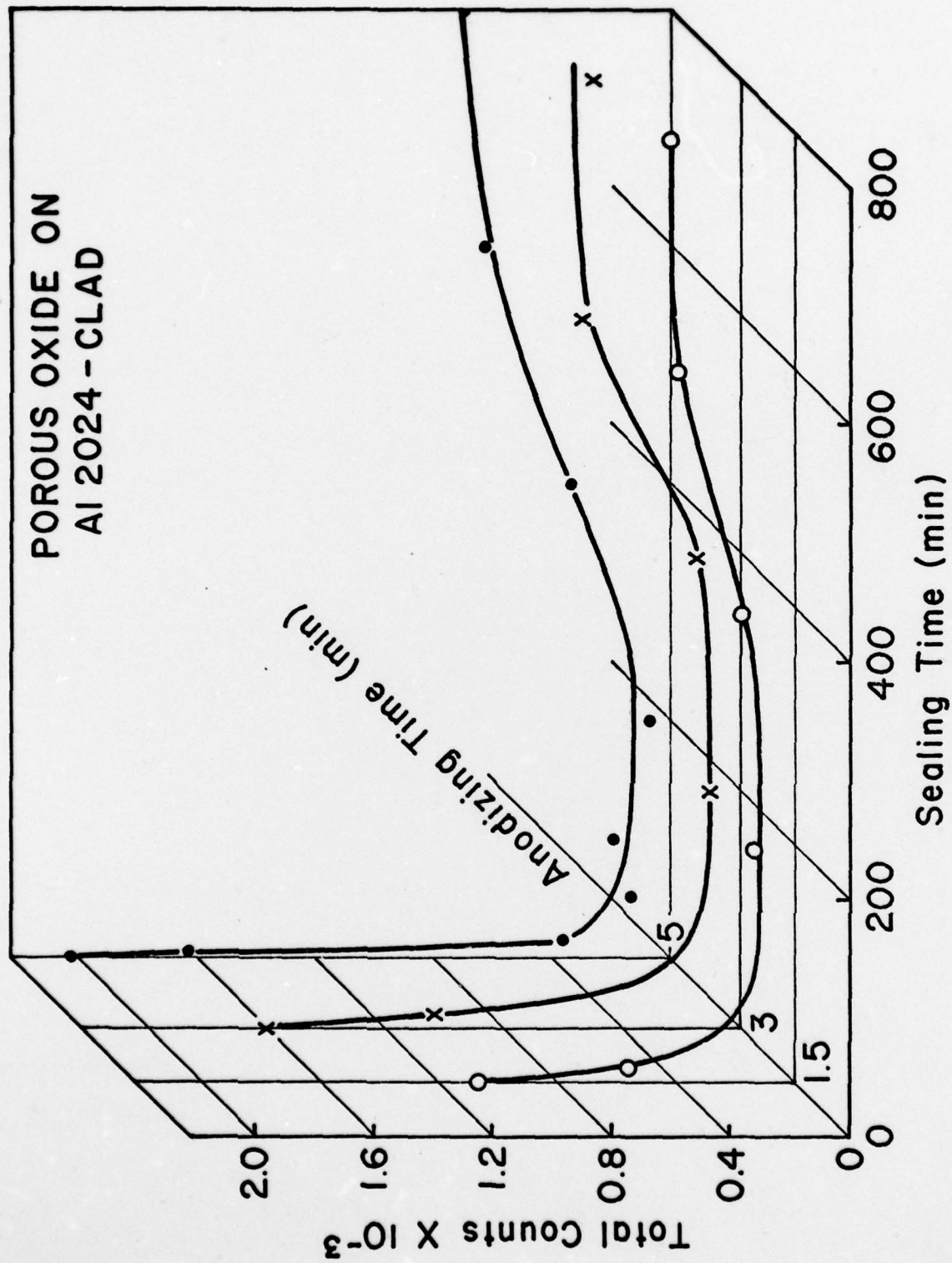


Fig. 10